Track Based Alignment for the Mu3e Pixel Detector

Dissertation
zur Erlangung des Grades
Doktor der Naturwissenschaften
am Fachbereich Physik, Mathematik und Informatik der
Johannes Gutenberg-Universität in Mainz

Ulrich Benedikt Hartenstein
geboren in Rastatt
Mainz, den 20.12.2018

Abstract

Ulrich Benedikt HARTENSTEIN

Track Based Alignment for the Mu3e Pixel Detector

In the hunt for new physics, the Mu3e experiment searches for the lepton flavour violating decay $\mu^+ \to e^+e^-e^+$ with a sensitivity goal of 1 in 10^{16} decays. In the Standard Model of particle physics, this process is heavily suppressed, making its observation a clear indicator of physics beyond the Standard Model. Up to 10^9 muons per second will be stopped in a target and decay at rest inside a magnetic spectrometer. To reconstruct the trajectories of the decay products, multiple concentric barrel shaped layers, consisting of about 3000 very thin (50 µm) high-voltage monolithic active pixel sensors, are used. With sensors that thin, the customary way of aligning a tracking detector - i.e. for position and orientation of detector parts only - is not sufficient. In addition, possible surface deformations will need to be taken into account.

Since the assembly tolerance for the pixel sensors is too large to ensure good tracking results, a track based alignment programme, utilising the General Broken Lines fit and the MILLEPEDE-II algorithm will be used to achieve this precision in the final detector. A reliable alignment programme is an essential prerequisite for the *Mu3e* experiment, since inaccurate knowledge about the detector geometry will foil all attempts at data analysis.

In this work, preparations for aligning the pixel detector using a detailed simulation and the track based alignment tool MU3EPIXAL - which was developed in the context of this work - will be presented. The effects of misalignment will be discussed and it will be demonstrated that MU3EPIXAL is capable of determining corrections to misplacements of pixel sensors well enough to reach tracking performances agreeing almost perfectly with the results for the nominal detector.

Zusammenfassung

Ulrich Benedikt HARTENSTEIN

Track Based Alignment for the Mu3e Pixel Detector

Auf der Suche nach neuer Physik untersucht das Mu3e-Experiment den Lepton-Flavour verletzenden Zerfall $\mu^+ \to e^+e^-e^+$ mit einer Sensitivität von einem in 10^{16} Zerfällen. Laut dem Standardmodell der Teilchenphysik ist dieser Prozess stark unterdrückt, was eine Beobachtung dessen zu einem klaren Hinweis auf Physik jenseits des Standardmodells macht. In einem magnetischen Spektrometer werden bis zu 10^9 Myonen pro Sekunde von einem Target gestoppt, woraufhin sie in Ruhe zerfallen. Zylindrische Lagen, bestehend aus ca. 3000 sehr dünnen (50 µm) mit Hochspannung betriebenen monolithischen Pixelsensoren werden genutzt, um die Spuren der Zerfallsprodukte zu rekonstruieren. Die Nutzung solch dünner Sensoren führt dazu, dass die übliche Art des Alignments - allein nach Position und Orientierung der Detektorteile - nicht ausreicht. Zusätzlich müssen mögliche Verformungen der Oberflächen berücksichtigt werden.

Da die Toleranz beim Bau des Pixeldetektors zu groß ist, um noch eine gute Spurrekonstruktion garantieren zu können, wird ein auf Spuren basiertes Alignment-Programm, welches auf dem General Broken Lines fit und dem MILLEPEDE-II Algorithmus basiert, benutzt, um eine ausreichende Präzision im finalen Dektor zu erhalten. Ein zuverlässiges Alignment-Programm ist zwingend erforderlich, da ungenaues Wissen über die Detektorgeometrie jegliche Analyse vereiteln würde.

Mithilfe einer detaillierten Simulation und MU3EPIXAL, dem im Zusammenhang mit dieser Arbeit entwickelten Tool zum spurbasierten Alignment, wurden Vorbereitungen für das Alignment des Pixeldetektors getroffen, die in dieser Arbeit vorgestellt werden sollen. Effekte, welche durch ein falsches Alignment hervorgerufen werden, werden diskutiert und es wird demonstriert, dass MU3EPIXAL die Lage der Pixelsensoren mit einer Genauigkeit bestimmen kann, welche die Leistungsfähigkeit der Spurrekonstruktion so stark verbessert, dass sie fast exakt mit der des nominellen Detektors übereinstimmt.

Contents

Dedicated to my wife Anna.

Chapter 1

Introduction

> The important thing is not to stop questioning; curiosity has its own reason for existing.
>
> (Albert Einstein, [1])

The curiosity, Einstein encourages here, led to an understanding of the laws of nature at the heart of which we can find particle physics, a scientific field concerned with the fundamental constituents of our universe: *elementary particles*. In the 20th century, the combined works of many scientists around the world led to a description of all elementary particles and their interactions. Today this is known as the Standard Model of particle physics.

1.1 The Standard Model of Particle Physics

The Standard Model of particle physics (SM) provides a unified picture of our current understanding of physics in form of a Quantum Field Theory. In it, forces - i.e. interactions - between elementary particles are described as particles themselves - so called *bosons*[1].

The pinnacle of the model's success story was the discovery of the Higgs boson at the Large Hadron Collider (LHC) at CERN in 2012 [2]. As a consequence, all SM particles have been discovered experimentally; but the story does not end here. Although the SM describes many experimental observations with great success, there are still exceptions. For example: While it includes the description of three of the fundamental interactions (or forces) - namely the electromagnetic, the weak and the strong interactions -, it does not describe gravitational interactions. Hence the SM cannot yet be a *theory of everything* which should explain all of the above and with that all the fundamental forces we currently know about. In the following, a brief overview over the inner workings of the SM will be given.

Figure 1.1 shows a partitioning of the particles in the SM into different types. There are essentially two categories of particles: fermions and bosons.

Bosons Bosons represent interactions by carrying discrete amounts of energy and momentum between elementary particles.

[1] The Higgs boson being the exception here - it is not a force carrier.

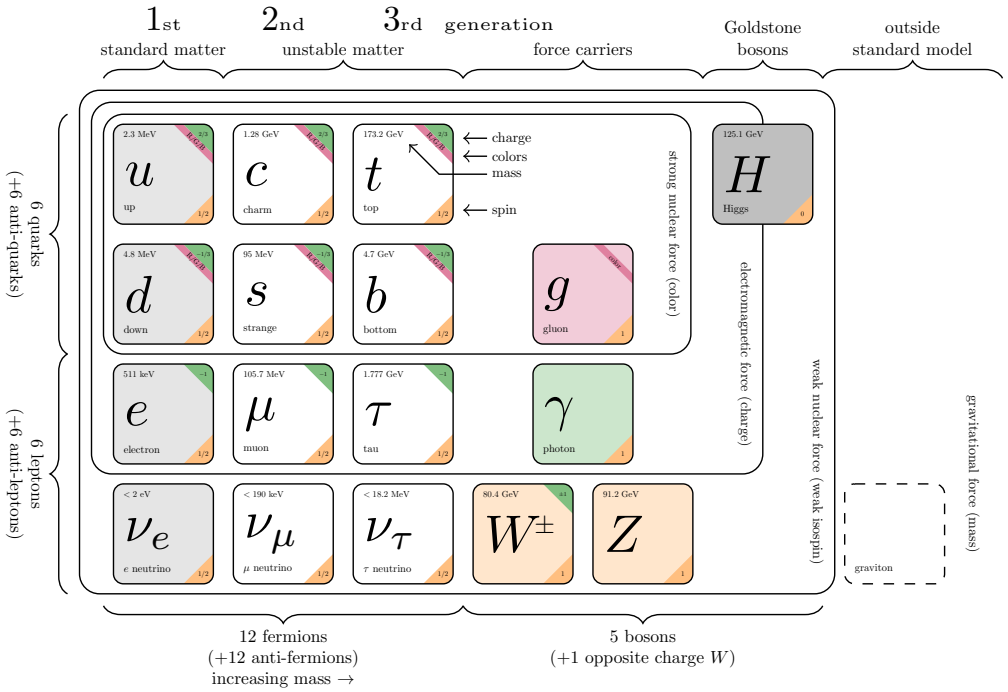

FIGURE 1.1: Elementary particles and force carriers according to the Standard Model of particle physics. Picture taken from [3].

The strong interaction is described by the theory of quantum chromodynamics (QCD) and defines interactions between quarks and gluons. It acts on the colour charge, is mediated by eight different gluons and binds quarks together to hadrons to make up the everyday matter (i.e. protons and neutrons). Since gluons themselves carry a colour charge, they can also interact with each other.

Quantum electrodynamics (QED) is the theory that describes the electromagnetic interactions via (virtual) photons between electrically charged particles.

The theory describing the weak force is occasionally referred to as quantum flavour dynamics (QFD). It is mediated by the W- and Z-bosons and couples to the weak isospin, a quantum number all left-handed fermions and right-handed antifermions[2] posses. Therefore, all fermions are affected by the weak force, making it the only possible interaction the SM allows for neutrinos. Above the energy scale of about 246 GeV [4], the electromagnetic and the weak interaction are combined in the electroweak unification.

The Higgs boson provides the mechanism by which the other elementary particles acquire their masses.

[2]Right-handed fermions and left-handed antifermions have a weak isospin of 0.

	e^-/ν_{e^-}	e^+/ν_{e^+}	μ^-/ν_{μ^-}	μ^+/ν_{μ^+}	τ^-/ν_{τ^-}	τ^+/ν_{τ^+}
L_e	$+1$	-1	0	0	0	0
L_μ	0	0	$+1$	-1	0	0
L_τ	0	0	0	0	$+1$	-1

TABLE 1.1: Leptons and their respective flavour numbers.

Fermions The matter one comes in contact with on a daily basis is made up of quarks and leptons; hence their alternative name: "matter particles". Quarks, interacting with all bosons, succumb to all the forces we currently know about. Leptons, however, do not interact with gluons (since they don't carry a colour charge). Fermions can be categorised in three generations or families, where lower generation relates to lower mass[3]. Therefore, generation I particles do not decay. Another classification can be constructed for the leptons: They can be divided into (electrically) charged (i.e. electron, muon and tau) and uncharged leptons (i.e. neutrinos). Hence, neutrinos, as opposed to charged leptons, only carry a weak charge and therefore only couple to Z- and W-bosons. In addition to the particles mentioned in Figure 1.1, every fermion has a specific *antiparticle* which possesses the opposite quantum numbers. In each generation, a flavour number (L_e, L_μ or L_τ) equal to -1 or 1 is assigned to each lepton and its antiparticle respectively. Table 1.1 shows an overview of the leptons and their flavour numbers.

In the following, the names of particles and their corresponding antiparticles will be used interchangeably; hence for example electron also stands for the positron.

Muon Decay in the Standard Model The fermion of the second generation is the muon. It has a mass of about 105.7 MeV and a lifetime of about 2.2 µs. Its main decay channel - with a branching fraction of almost 100 % - is the so called "Michel decay": $\mu^+ \to e^+ \overline{\nu}_e + \nu_e$. With a branching fraction of 1.4 % an additional photon is radiated and with a branching fraction of 3.4×10^{-5} this photon converts to an e^+e^--pair [5]. The Feynman graphs of these three decays are displayed in Figure 1.2.

In the hunt for a new model that describes all the physics we currently know about, a good starting point is to test the limits of the SM. There are essentially two ways to go about that. One way is direct searches as performed at the LHC, where the idea is to find new particles and processes by going to previously unreached energy levels. Indirect measurements on the other hand probe for new physics by performing precision or high intensity measurements.

[3]Strictly speaking, this can not be said with certainty for neutrinos, since their absolute masses have not been measured yet.

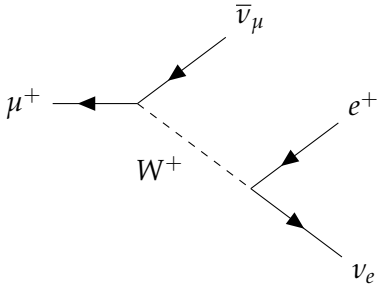

(A) Michel decay.

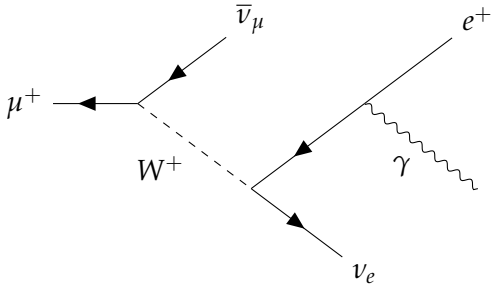

(B) Michel decay with an additional photon.

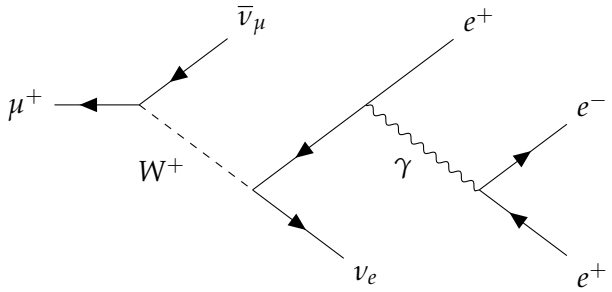

(C) Michel decay with a photon performing internal conversion to an e^+e^--pair.

FIGURE 1.2: Michel decays and subsequent additional decays.

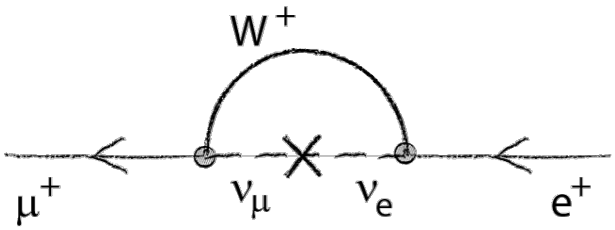

(A) Decay of a muon to an electron via neutrino oscillation.

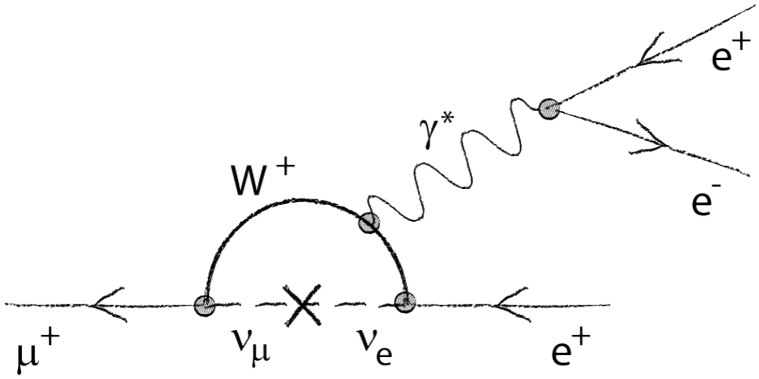

(B) Decay of a muon to three electrons via neutrino oscillation.

FIGURE 1.3: Feynman diagrams for decays via neutrino oscillation.

The *Mu3e*-Experiment falls under the latter category; its intention is to search for new physics by investigating the sector of lepton flavour violation (LFV).

1.2 Lepton Flavour Violation

There are several laws of conservation in particle interactions; and they are firmly linked to "symmetries". The term symmetry refers to an invariance of the equations that describe a physical system, i.e. an invariance in the *Lagrangian* function. The conservation of energy for example requires that the *Lagrangian* does not explicitly depend on time. One can distinguish between "continuous" and "discrete" symmetries. According to *Noether's theorem*, the former category always implicates a conserved quantity: e.g. time symmetry implicates energy conservation. However, discrete symmetries are accidental and occur only because of very specific circumstances. An example for a conservation law resulting from such an accidental symmetry is the conservation of lepton flavour in the SM. To first order, lepton flavour is conserved, preventing the decay of one lepton to another, where they have different flavour numbers. But there are exceptions which, in this case, lead to the violation of lepton flavour conservation.

1.2.1 In the Standard Model

According to the SM, lepton flavour must be conserved at tree-level[4], prohibiting processes like e.g. $\mu^+ \rightarrow e^+e^-e^+$. For neutrinos, this conservation is already obsolete, since its violation has been observed by various experiments [6–8]. Massive neutrinos allow a process called neutrino oscillation or mixing, where a neutrino can change its lepton flavour, breaking the symmetry which implicates lepton flavour conservation, allowing for processes like the one mentioned above. A possible lepton flavour violating decay of a muon is depicted in Figure 1.3: The charge of the antimuon is carried away by a W^+-boson, leaving a muon-neutrino, which in turn changes flavour to become an electron neutrino. The W^+-boson can afterwards combine with the electron-neutrino to form a positron. Additionally, a radiated gamma particle can decay into an electron-positron pair, forming the final state of two positrons and one electron. Decays like this, however, are heavily suppressed and occur only with a branching ratio (BR) of [9][5]:

$$BR(\mu^+ \rightarrow e^+e^-e^+) \approx 5.2 \cdot 10^{-55} \tag{1.1}$$

This branching ratio is too small[6] to be observable in any experiment, making a measurement of such a decay a clear indicator of physics beyond the SM.

[4]Tree-level means, the corresponding Feynman graph does not contain loops of particles, hence only leading order calculations are taken into account.

[5]The cited calculation includes not only neutrino oscillation, but also other higher level effects and external massive particles.

[6]This is due to the tiny ratio of the difference of the neutrino mass squares ($\mathcal{O}(10^{-3}\,\mathrm{eV}^2)$) and the squared mass of the W-boson ($m_W = 80.4\,\mathrm{GeV}$) entering at the second power.

1.2.2 Beyond the Standard Model

There are many theories going beyond the SM that predict the branching ratio in Equation 1.1 to be much larger and even detectable. Some of them shall be briefly introduced here.

Supersymmetric Theories In supersymmetric models, for each particle contained in the SM, a so called "superpartner" which differs by half a unit of spin, is added. The superpartners of leptons are therefore bosons and are called "sleptons". In some SUSY models, the mass matrix of these sleptons has off-diagonal elements, allowing for LFV via mixing of sleptons (cf. Figure 1.4c).

Triplet Higgs Model By introducing a Higgs triplet, consisting of a neutral, a singly and a doubly charged scalar, neutrino Majorana masses can be generated. Such a theory allows for lepton flavour violation at tree level, since the Higgs field carries lepton number -2 [10] (see Figure 1.4a).

Extended Gauge Sector These models give rise to new heavy bosons, such as the Z' [11] which can mediate $\mu \to eee$ decays. This is shown in the Feynman graph in Figure 1.4b.

The above mentioned models (among others) suggest the BR of a lepton flavour violating decay of a muon to be on the experimentally accessible level. This prompts the search for new physics in that area. Figure 1.5 shows an overview of current, past and future experiments, investigating muon decays, where at least one of the resulting particles is an electron. There are experiments searching in the channels $\mu \to e\gamma$, $\mu \to 3e$ and $\mu N \to eN$. For each of the $\mu \to e + X$ decays mentioned in Figure 1.5, at least one new experiment or an upgrade to an already existing one is being built. This shows the prominence of these lepton flavour violating decays.

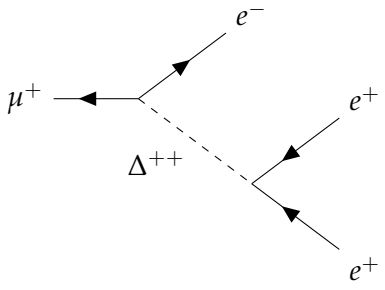

(A) Double charged scalar from Higgs triplet.

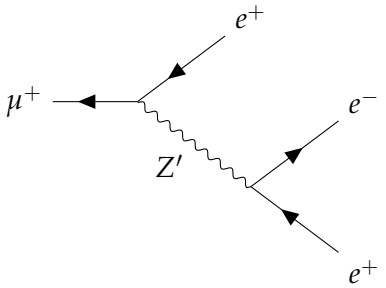

(B) Additional gauge boson (Z').

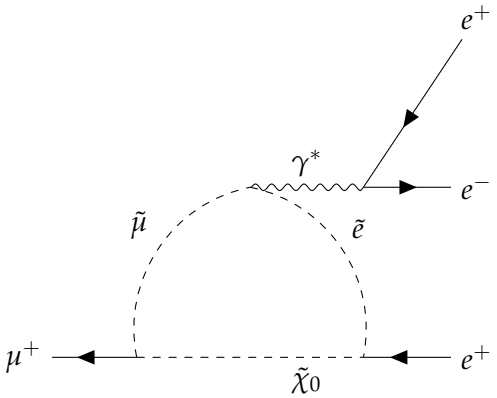

(C) SUSY loop diagram with *neutralinos* and *sleptons*

FIGURE 1.4: $\mu^+ \to e^+e^-e^+$ signal decay as described in various models beyond the SM.

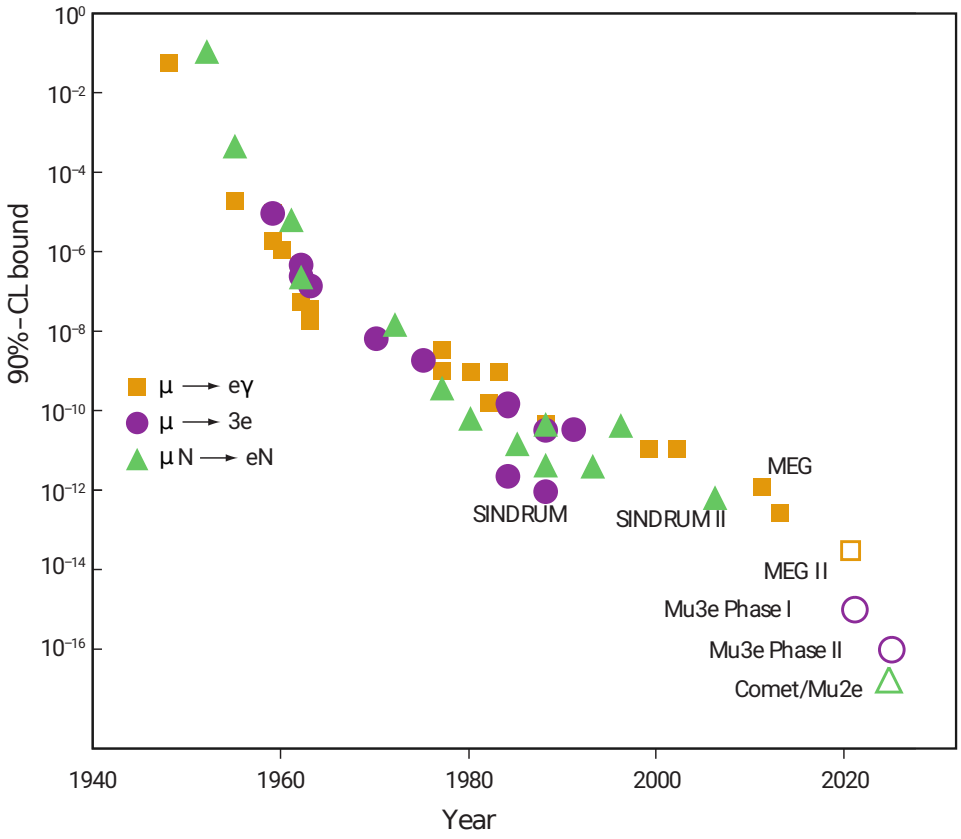

FIGURE 1.5: Past and future experiments searching for lepton flavour violation for muons decaying to electrons. Hollow markers represent future experiments that are under development, solid markers represent currently running or already concluded experiments. Adapted from [12] and updated with recent experiments.

Chapter 2

The Mu3e Experiment

As the name suggests, the main purpose of the *Mu3e* experiment is to search for the lepton flavour violating process of a Muon decaying to three electrons. The exact decay to be studied is $\mu^+ \to e^+e^-e^+$, which - in the Standard Model - is forbidden. If one includes the possibility of neutrino mixing it becomes an allowed process, is however heavily suppressed by a factor of approximately 10^{-54} [9].

During the first of the two planned phases of *Mu3e*, the goal is to reach a single event sensitivity of $2 \cdot 10^{-15}$. To be able to achieve this goal, an intensity of 10^8 muons per second in a continuous beam are required, making the πE5 beam line at the Paul Scherrer Institute (PSI) in Switzerland the perfect choice to build the experiment.[1] In a second phase, the sensitivity of *Mu3e* is planned to be improved by a factor of 20, making it $1 \cdot 10^{-16}$, which would improve the current limit - set in 1988 by SINDRUM- by four orders of magnitude [13]. This could be made possible by the construction of the *high intensity muon beam* (HiMB) that is currently under study at PSI.

In the end, the physics results can only be as good as the detector allows them to be. This includes detector calibration and - particularly - the detector alignment. The following chapter will focus on the experimental challenges followed by the detector design. With this knowledge at hand, one can then investigate the demands on the tracker alignment. Since the commissioning of *Mu3e* is set to be in 2020, the alignment software was developed with the help of a detailed detector simulation which is part of the *Mu3e* software package that will be briefly introduced in the concluding part of this chapter.

2.1 Signal and Background

The signal decay $\mu^+ \to e^+e^-e^+$ is identified by two positrons and one electron originating from the same vertex at the same time. This means the following two conditions apply:[2]

[1] See subsection 2.2.6 for more information on the beam line.
[2] In natural units: $c = \hbar = 1$

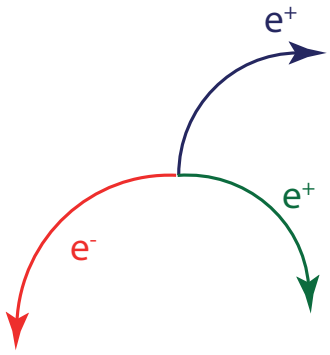

FIGURE 2.1: Event topology of the signal decay $\mu^+ \to e^+e^-e^+$.

1. The sum of four-momenta of the electrons is equal to the muon mass:

$$\left(\sum_{i=1}^{3} P_{e,i}\right)^2 = m_\mu^2. \tag{2.1}$$

2. In the rest frame of the muon, the three-momenta of the electrons add up to zero:

$$\sum_{i=1}^{3} \mathbf{p}_i = 0. \tag{2.2}$$

The incoming muons are stopped in a target and decay at rest. Therefore the latter equation also holds in the lab frame. An example event topology that fulfills the mentioned requirements is depicted in Figure 2.1. However not only the signal can lead to a topology that can be identified as the wanted process. There are several other processes that can occur, mimicking the signal topology up to small deviations, which makes vertex, momentum and timing resolution crucial parts of *Mu3e*. In the following, the main sources for background are discussed.

2.1.1 Internal Conversion

One of the possible background processes is the radiative muon decay with internal conversion $\mu^+ \to e^+e^-e^+\nu\bar{\nu}$ which is similar to the signal but conserves lepton flavour because of the additional neutrinos. This has been briefly discussed in section 1.1 and a Feynman graph is displayed in Figure 1.2c. Additionally, a schematic depiction is shown in Figure 2.2a. With a branching fraction of $3.4 \cdot 10^{-5}$ [14] it is expected to be the main background but can be distinguished from the signal by making use of energy and momentum conservation. Since the neutrinos carry away energy and momentum, equations (2.1) and (2.2) do not hold at the same time for this process but would only deviate by very little. Therefore, a very good momentum resolution is necessary to be able to distinguish this background from the signal. Figure 2.3 shows the branching fraction of internal conversion contamination in the signal region as a function of the mass resolution. From there one can deduce that in

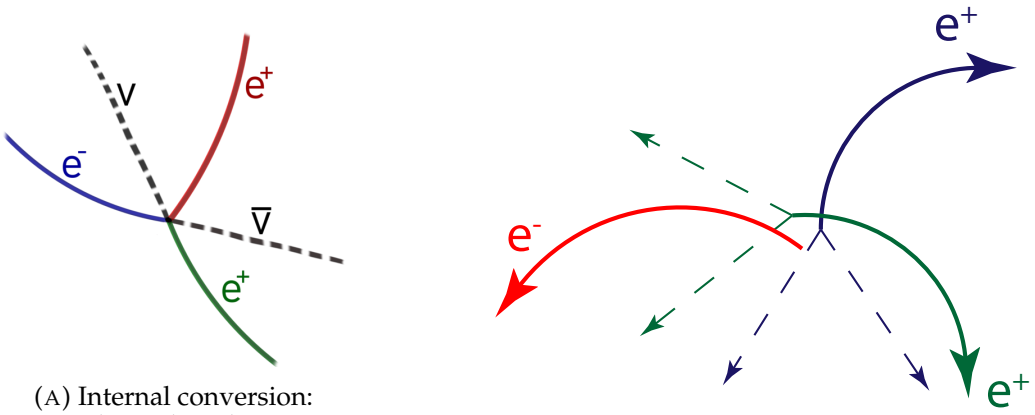

(A) Internal conversion: $\mu^+ \to e^+e^-e^+\nu\bar{\nu}$

(B) Accidental background originating from two Michel decays and an additional electron.

FIGURE 2.2: The two main sources for background events that are expected for the *Mu3e* experiment.

order to reach the goal of a sensitivity of $2 \cdot 10^{-15}$ with a 2σ cut on the reconstructed muon mass, the average mass resolution has to be better than $1.0\,\mathrm{MeV}/c^2$.

Since the mass resolution is directly related to the momentum resolution[3], this goal can not be achieved without an excellent tracker alignment. In chapter 4, the effects, misalignment has on the momentum resolution of the tracking detector, will be demonstrated. This will motivate the need for a track based alignment as will be presented in chapter 5.

2.1.2 Accidental Background

The main process contributing to accidental background is the primary decay channel of a positively charged muon: the Michel decay $\mu^+ \to e^+\nu\bar{\nu}$. In contrast to the signal, there is no negatively charged particle in the Michel decay. Hence, it can only contribute to the background in combination with other processes that provide negatively charged particles, like Bhabha scattering, photon conversion or Compton scattering. If a positron from Michel decay and an electron and a positron from other sources are falsely combined, an event topology similar to the signal topology can appear (see Figure 2.2b). If both the electron and the positron from Bhabha scattering are observed, the accidental coincidence is even enhanced, since two of the three particles already have the same vertex and just one more positron is needed to mimic the signal. All of these background processes have one thing in common: There is no common vertex for the three particles in question.

Hence, with an excellent vertex and time resolution, it is possible to suppress accidental background sufficiently. Especially for the vertex resolution, a good tracker alignment is crucial.

[3]The mass of the muon can be reconstructed via the momenta of its decay particles.

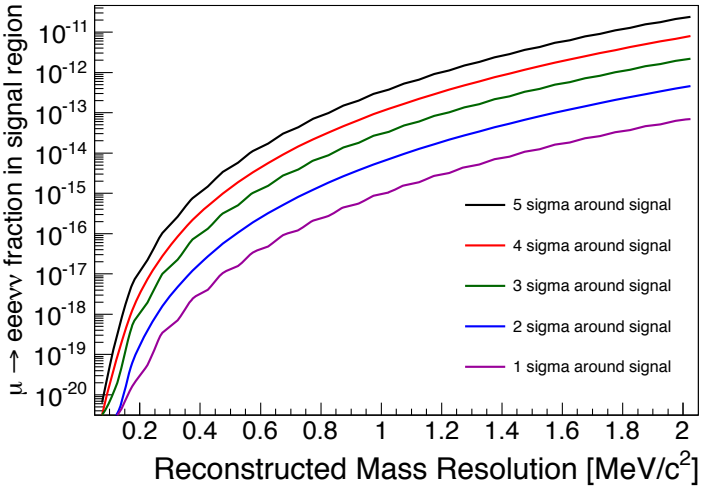

FIGURE 2.3: Contamination of the signal region with internal conversion events as a function of energy resolution. Figure taken from [15].

2.2 Detector Concept

When a detector concept is developed, it is essential to think about the limiting factors for its physics performance. There are mainly two limiting aspects concerning momentum and vertex resolution: the positional resolution of the sensor used for detecting passing particles and multiple Coulomb scattering in detector material. By using gaseous detectors, such as time projection chambers or wire chambers, the material budget would be very low, reducing the multiple Coulomb scattering. However, it would not be possible to handle the high rates needed to reach the sensitivity goal or the precision needed for effectively reducing background processes. Despite of the higher material budget, this leaves using silicon pixel sensors for particle tracking to be the only sensible option for *Mu3e*.

The resolution of a pixel sensor (with digital readout) σ_x is derived from the variance of a uniform distribution over the pixel:

$$\sigma_x^2 = \int_{-a/2}^{a/2} x^2 f(x) dx \tag{2.3}$$

$$= \frac{a^2}{12} \tag{2.4}$$

$$\Rightarrow \sigma_x = \frac{a}{\sqrt{12}}, \tag{2.5}$$

with the uniform distribution function $f(x) = 1/a$ (for $0 \leq x \leq a$) and the pixel pitch a. Therefore, the resolution is directly correlated to the pixel size.

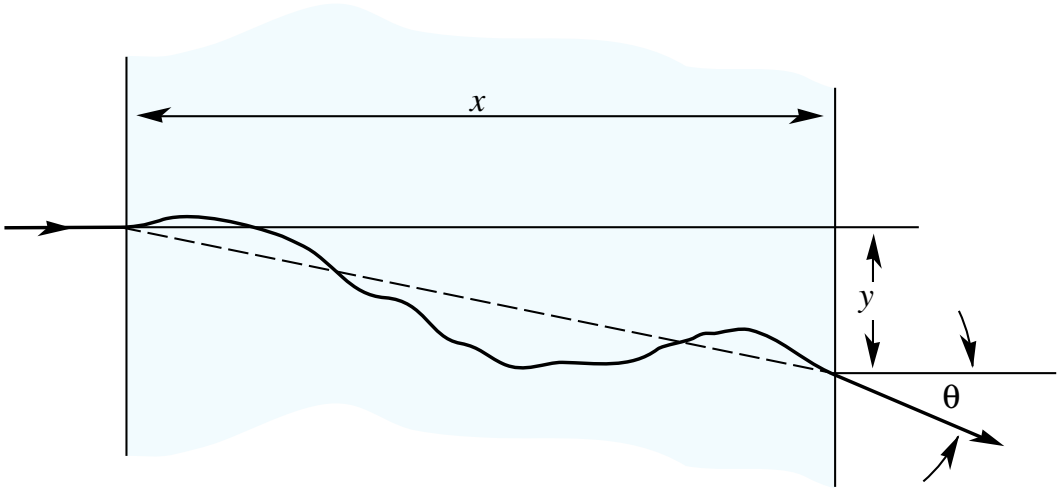

FIGURE 2.4: Multiple scattering of a particle traversing material. The particle is deflected multiple times inside the material which leads to an offset y and a scattering angle θ with respect to its incoming trajectory. Figure based on [5].

Multiple Coulomb scattering, as depicted in Figure 2.4, can be approximated by a Gaussian function with a distribution width for the scattering angle of

$$\theta_0 = \frac{13.6\,\mathrm{MeV}}{\beta c p} z \sqrt{x/X_0}\,(1 + 0.038\,\ln(x/X_0))\,, \tag{2.6}$$

where x/X_0 is the thickness of the traversed material in units of radiation length, p, βc and z are the momentum, velocity and charge number of the incident particle respectively [5, 16]. To reduce multiple scattering, it is therefore crucial to hold the material budget to a minimum by making the sensors as thin as possible. Additionally, this has the effect that offsets (labelled y in Figure 2.4) become negligibly small and multiple Coulomb scattering can be simply parametrised by θ_0.

In the *Mu3e* experiment, muons are stopped and will decay at rest; hence, their decay products cannot exceed an energy that corresponds to half the muon mass, i.e. approximately 53 MeV. The pixel sensors used for tracking will have a pixel size of 80 µm (see chapter 3) making multiple Coulomb scattering the dominating factor concerning momentum and vertex resolution.

To be able to measure the momentum of a particle in the first place, a magnetic field is needed. In a magnetic field the Lorentz force[4] bends the trajectories of charged particles such that they describe a helical motion[5]. If one can figure out the radius of this helix, one can calculate the momentum of the corresponding particle via

$$p_T \approx 0.3 B \rho. \tag{2.7}$$

[4]Disregarding electric fields, the Lorentz force is calculated via $\mathbf{F_L} = q\mathbf{v} \times \mathbf{B}$, with the particle's electrical charge q, its velocity $\mathbf{v}$ and the magnetic flux density (a.k.a. magnetic field strength) $\mathbf{B}$. Thus, the Lorentz force acting on a charged particle is always perpendicular to the particle's velocity and the field strength.

[5]Provided their velocity has a component perpendicular and a component parallel to the magnetic flux density.

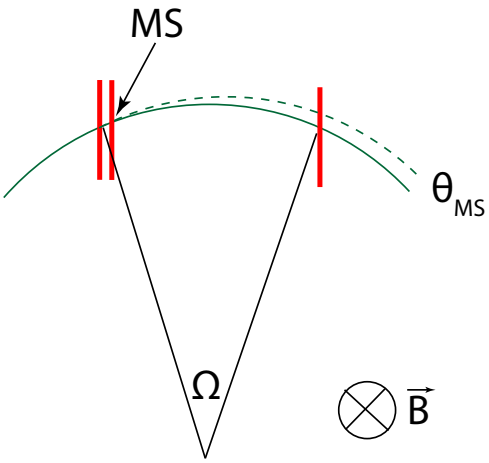

(A) Multiple scattering for measurement planes with a distance $\ll \pi$.

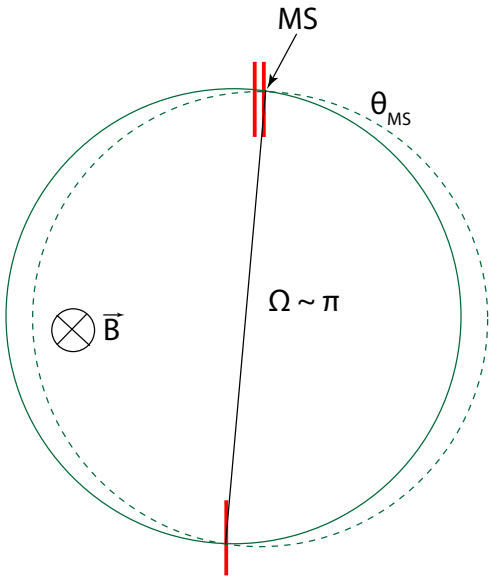

(B) Multiple scattering for measurement planes with a distance of π.

FIGURE 2.5: Effect of multiple scattering on trajectory offsets after different path lengths. For path lengths close to (multiples of) π, the offset due to multiple Coulomb scattering is minimised.

With p_T being the transverse momentum of the particle in units of GeV c^{-1}, B being the magnetic flux density in T and ρ being the radius of the helix - projected onto a surface perpendicular to the magnetic field - in m. So the task is to reconstruct helical tracks, calculate their radius and from there derive the particle momentum.

In Figure 2.5 it can be seen that the effect multiple scattering has on momentum resolution cancels to first order if a particle is measured again after one or more half turns. Since this is very much desirable, the geometry of the *Mu3e* tracking detector is chosen such that particles that re-enter the tracking detector due to the magnetic field, predominantly do so when their bending angle is a multiple of π.

A schematic cut view of the detector concept fulfilling the above requirements is displayed in Figure 2.6 and a CAD model can be found in Figure 2.7. The tracking detector consists of layers arranged as barrels around the target and is composed of monolithic silicon pixel sensors (see chapter 3 for more details).

However, pixel sensors alone won't be enough to meet the requirements. The time resolution of the used sensors was measured to be as low as 6.5 ns [17], which is excellent for monolithic pixel sensors but not quite good enough for a sufficient background suppression. Therefore, additional timing detectors (cf. subsection 2.2.3) that will improve the overall time resolution to better than 100 ps are implemented just inside of the outer pixel layers.

2.2.1 Stopping Target

The target has to walk the thin line between having enough material to stop as many muons as possible but at the same time not having too much material in a sense

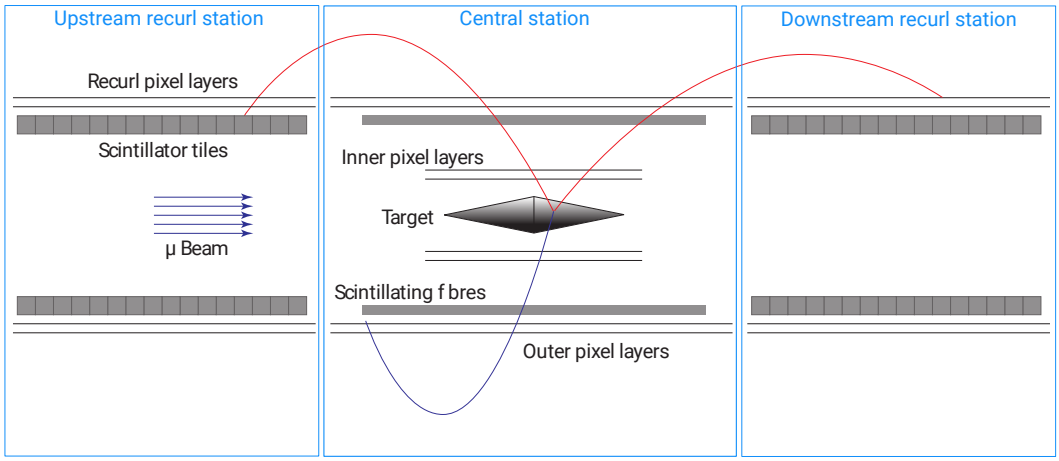

FIGURE 2.6: Schematic cut (along the beam direction) of the *Mu3e* detector for the first phase. (not to scale)

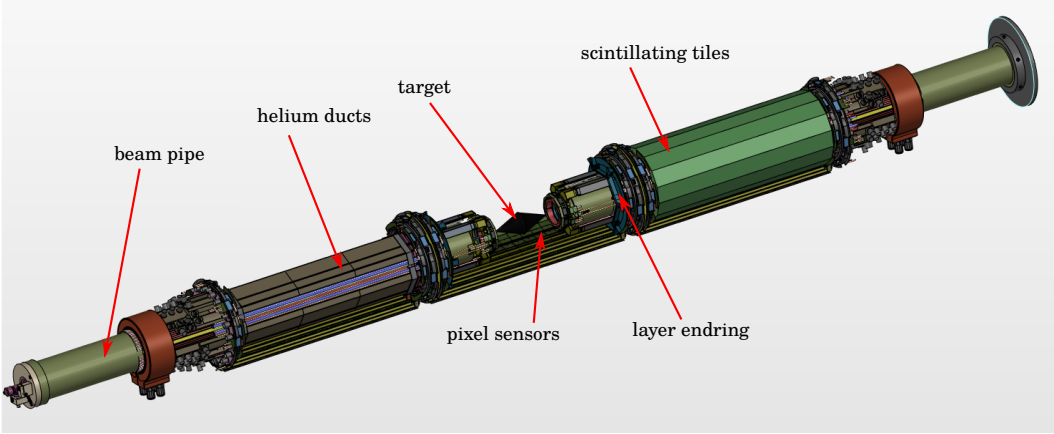

FIGURE 2.7: Partial CAD model of the *Mu3e* detector. To make all the relevant parts visible, not the whole detector is displayed here.

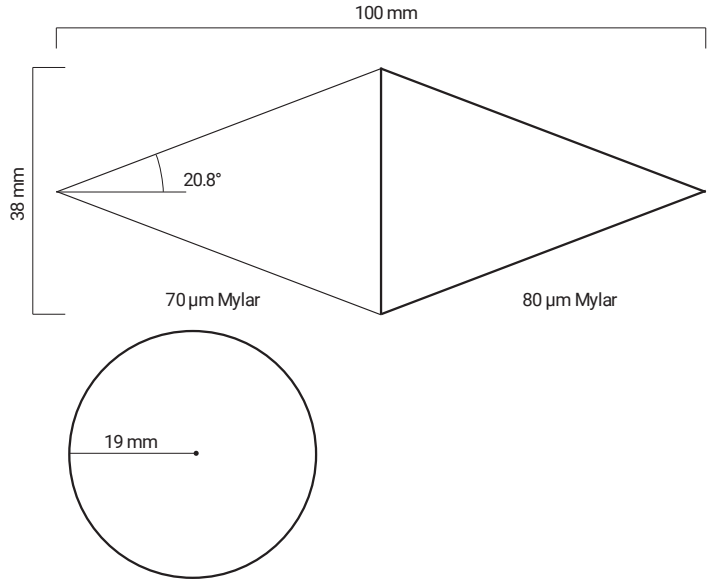

FIGURE 2.8: Baseline design for the *Mu3e* target (material thickness is not to scale).

that more material means more background processes and more challenging track reconstruction. By using a material with low atomic number Z, photon conversion and large angle Coulomb scattering are suppressed and spreading out the target widely helps to reduce accidental coincidences of track vertices.

A hollow double cone target à la SINDRUM [13] as depicted in Figure 2.8 satisfies these demands. The design consists of 70 µm and 80 µm thick Mylar in the upstream and downstream half respectively. This results in a total of 0.16% of a radiation length for passing muons. Using a hollow target instead of a solid one does not only reduce the material budget but also assists the vertex reconstruction. The decay vertex position can be restricted to just the surface of the double-cone, whereas for a solid target the vertex could be situated anywhere in the complete volume. Carbon fibre pipes are used to hold the target in place which allows for easy removal and exchange if desired. Simulations and studies with various shapes and materials lead to the described baseline design and have shown that it in fact fulfills the requirements mentioned previously [15].

2.2.2 Tracking Detectors

For tracking particle flight paths, two cylindrical double layers of silicon pixel sensors supported by a polyimide framework are used. Since charged particles travelling through a magnetic field describe a helical trajectory[6], at least three measurement points are needed to determine said trajectory. Hence, a particle traversing two double layers of sensors will provide an additional redundancy of measurements in form of a fourth measurement point. This allows the definition of a χ^2 value for each fitted track and opens up the possibility of a track selection by χ^2.

The geometry of the tracker layers determines the acceptance and momentum resolution for outgoing tracks. One set of double layers is located as close as possible to the target, while not interfering directly with the beam but providing the highest possible vertex resolution. The second set of layers with larger radii is implemented to offer a basis for a reliable track reconstruction. Having a large lever arm means an improved measurement of the bending radius of a particle which, in turn, directly leads to a better momentum resolution (see Equation 2.7). However, the outer layer radii can not be chosen to be arbitrarily large, since - aside from the spacial restrictions - too large radii prevent a proper reconstruction of strongly curved tracks. Because of the low momentum of the particles and their multiple scattering dominated trajectories, the arrangement of layers in pairs with only small gaps in between is favoured. The information from such a layer pair allows for the reconstruction of a basic "track stub" which limits the combinatorial burden on track finding. By implementing so called "recurl stations" (cf. Figure 2.6), it is possible to get another set of measurements for particles that curl back further away (upstream or downstream) from the target.

[6] Of course this is only true if the particle is not disturbed by material on its path.

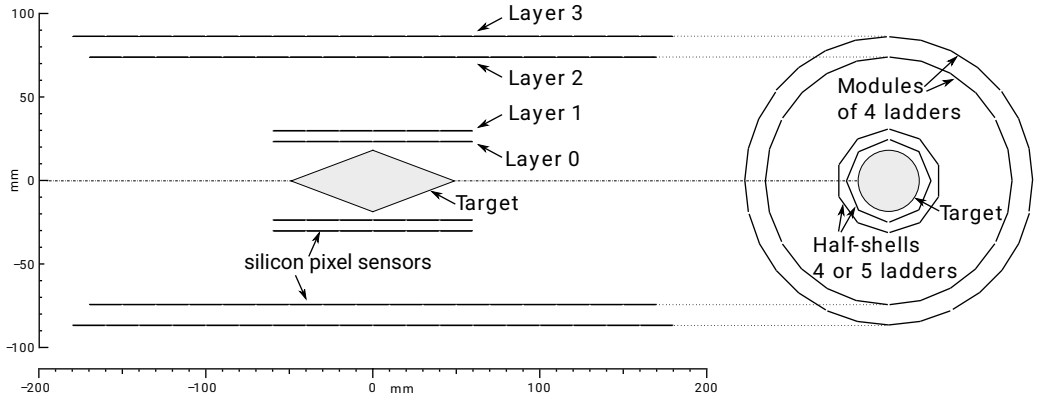

FIGURE 2.9: Schematic view of the central detector layout including scale.

For the *Mu3e* experiment to succeed, a very low material budget but also a very precise position measurement are required. Put this together with the demands on the fast digital readout because of the high rates, the only sensible solution for *Mu3e* was the development of a new High Voltage Monolithic Active Pixel Sensor (HV-MAPS): the MUPIX [18]. It can be thinned down to 50 µm, has a pixel pitch of 80 µm and a time resolution of the order of a few ns. A more detailed description of this technology can be found in chapter 3.

Figure 2.9 shows the central tracker parts and its measures and Figure 2.10 shows the hierarchical structure of the *Mu3e* tracking detector (which will play a large role in later chapters). All MUPIX sensors used for the tracking detector have an active area of $20 \times 20\,\mathrm{mm}^2$ and are supported by thin polyimide substrates. On these so called "High Density Interconnects" (HDI), signal and power lines are implemented as thin aluminium traces. Multiple MUPIX chips can be glued on an HDI to form a thin support structure and make up *ladders* that represent the smallest mechanical unit. The ladders of the inner layers (also referred to as the vertex layers) carry six sensors each, the outer layers carry 17 or 18 sensors each. The ladders have an overlap of 0.5 mm which does not only improve the acceptance but is also beneficial for the alignment, since particles traversing the overlapping regions connect detector parts that are usually not connected by a particle trajectory. Additionally, hits in the overlapping regions provide measurements with a high precision because of their close proximity. The pixel modules consist of several ladders held by an "endpiece". Multiple modules are mounted with their endpieces onto an "endring" (cf. Figure 2.11) to build up cylindrical detector layers. To improve stability, the longer ladders in the outer tracker layers will receive v-shaped polyimide folds[7] as schematically depicted in Figure 2.12. The active parts of the detector as well as the target will be supported by the beam pipes. The beam pipes on the other hand are supported by a detector cage on a rail system which allows for easy maintenance access.

[7] As will be seen in subsection 2.2.5, these folds are used for cooling purposes as well.

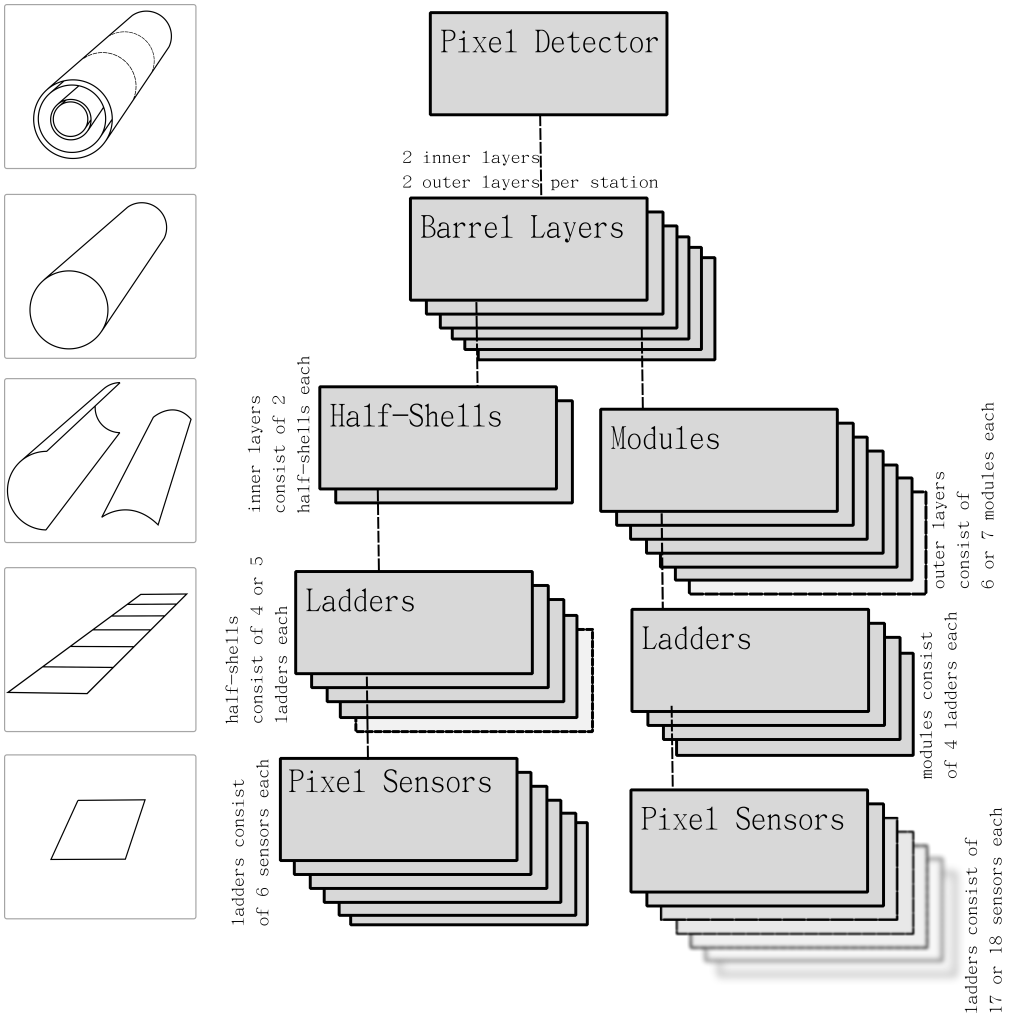

FIGURE 2.10: Schematic depiction of the hierarchical structure of the *Mu3e* tracking detector.

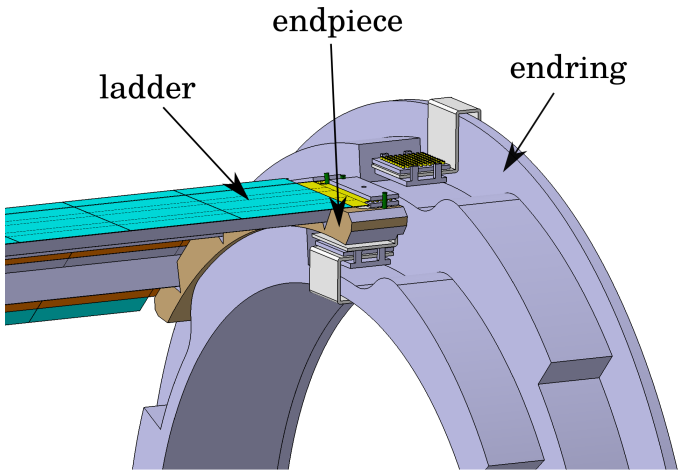

FIGURE 2.11: CAD model of a pixel module mounted with an endpiece onto an endring. Figure based on [15].

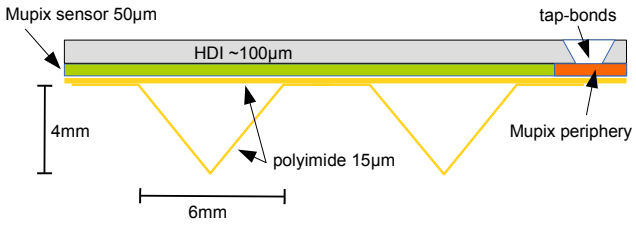

FIGURE 2.12: Cross section of an outer layer ladder with v-folds. Figure based on [15].

2.2.3 Timing Detectors

To guarantee sufficient combinatorial background suppression and high rate capabilities at the same time, two different types of timing detectors are used.

After a particle has passed the recurl stations, there is no need for detection anymore. Hence, it is possible to use a detector with a large material budget which results in a large energy deposit for passing particles. This means a high light yield and, in turn, a precise time information. Therefore, a detector made of scintillating tiles with an outer radius of about 6.3 cm will be implemented just inside of the recurl stations. It will be composed of individual tiles with a size of $6.5 \times 6.5 \times 5\,\mathrm{mm}^3$ each, which will be read out individually by silicon photomultipliers (SiPMs). Based on recent prototype tests, resolutions of better than 50 ps and detection efficiencies of close to 100% are expected for the tile detector in question [19]. Accidental background can therefore be sufficiently suppressed.

For the central detector region however, a tile detector is out of the question, because a low material budget is crucial here. Still, a detection efficiency of close to 100% and a timing resolution of better than 500 ps are required. With this at hand, even in topologies where one track does not reach the tile detector, accidental background can still be suppressed. In addition, by having another set of timing measurements, a reliable charge identification of a particle is made possible by utilising the time of flight between the outgoing and recurling part of particle trajectories[8]. Therefore, it is planned to build a timing detector with a radius of about 6 cm and a sensitive length of roughly 29 cm, consisting of 250 µm thin scintillating fibres just inside of the third pixel layer in the central detector region. In the current design, three or four layers of scintillating fibres with round cross sections - arranged in ribbons - are foreseen to be used. At each end, SiPMs will be placed for photon detection. This will allow for a timing resolution of the fibre detector of better than 400 ps [20].

[8] Of course, this only makes sense if the particle actually recurls into the detector.

2.2.4 Magnet

For a precise momentum determination with the *Mu3e* detector, a homogeneous solenoidal magnetic field is fundamental. The magnetic field strength of 1 T is chosen (in combination with the selected pixel layer radii) to minimise multiple scattering for the majority of the decay electrons with a momentum of $\sim 30\,\mathrm{MeV}\,c^{-1}$. Although, to allow for future modifications, it is foreseen to have a variable field strength that ranges up to 2.6 T. The solenoid is planned to be approximately 2.5 m long and have a radius of about 55 cm. Within the solenoid, a field stability of $\leq 10^{-4}$ is required. The same is true for the stability within 100 days of running. As can be seen in Figure 2.13c, the magnetic field can be considered as constant in the central detector part in longitudinal direction. Perpendicular to the beam (as can be seen in Figures 2.13a and 2.13b) the magnetic field is negligibly small.

2.2.5 Cooling

Most of the active hardware components produce significant amounts of heat. A cooling system is therefore an essential part of the *Mu3e* detector. A global gaseous helium flow through the whole magnet bore will provide a basis for cooling. The elements inside the active detector volume will be cooled by gaseous helium flows in the volumes in between the pixel layers and the fibre detector. In addition, the v-folds in the polyimide support structure for the outer layers will serve as high flux helium cooling channels. Elements located outside the active volume, such as the readout electronics and the SiPMs, are cooled by water.

Although a heat dissipation of only $300\,\mathrm{mW\,cm^{-2}}$ is expected for the MuPix sensors, the cooling strategy is planned such that it can reduce the occurring temperature gradient to a reasonable level for heat dissipations of up to $400\,\mathrm{mW\,cm^{-2}}$. However, a temperature gradient in the detector can not be prevented completely. Lab studies and simulations have shown, that - in agreement with the accepted power consumption - the planned cooling system is able to restrict the temperature gradient over the inner and outer pixel layers to less than 70 K and 40 K respectively [22]. However, these temperature alterations evoke detector parts to expand and contract which affects the detector alignment; even on single sensor level, these effects will take place. The alignment algorithm will have to make sure these changes in geometry are accounted for.

2.2.6 Muon Beam Line

Mu3e - being a coincidence experiment - not only requires to run at extremely high intensities but also benefits from a continuous muon beam, since this provides a lower instantaneous muon rate and therefore helps to reduce accidental background. This makes PSI the right place to be for *Mu3e*.

It hosts a proton accelerator with 1.3 MW average beam power [23]. Via interaction with a production target, pions are produced which then mainly decay to muons

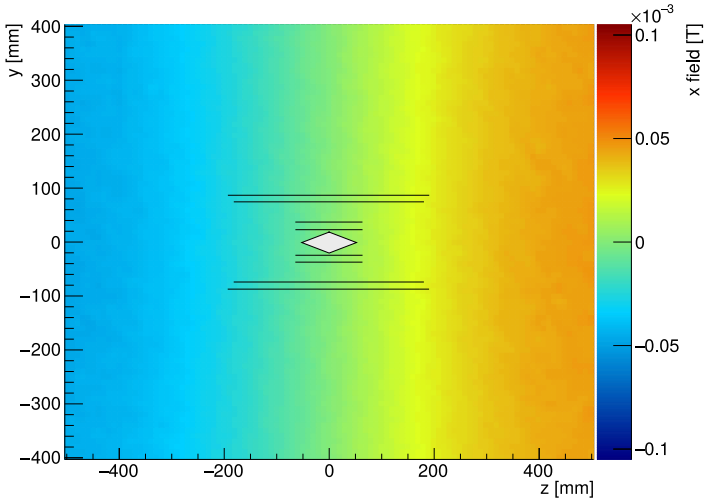

(A) Along global x-direction (perpendicular to the beam axis).

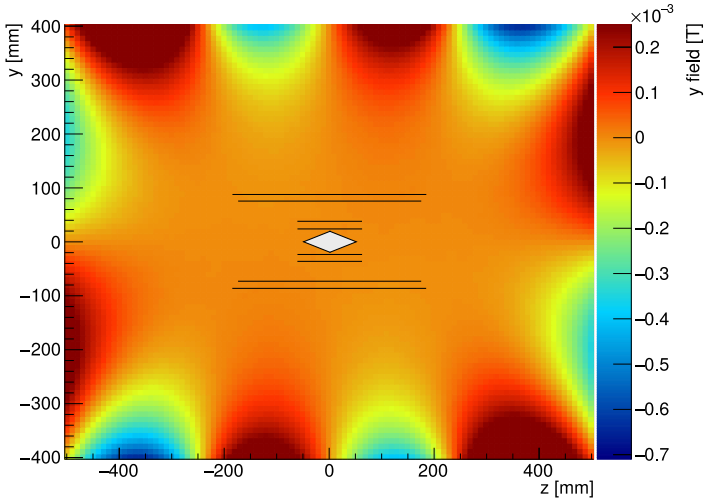

(B) Along global y-direction (perpendicular to the beam axis).

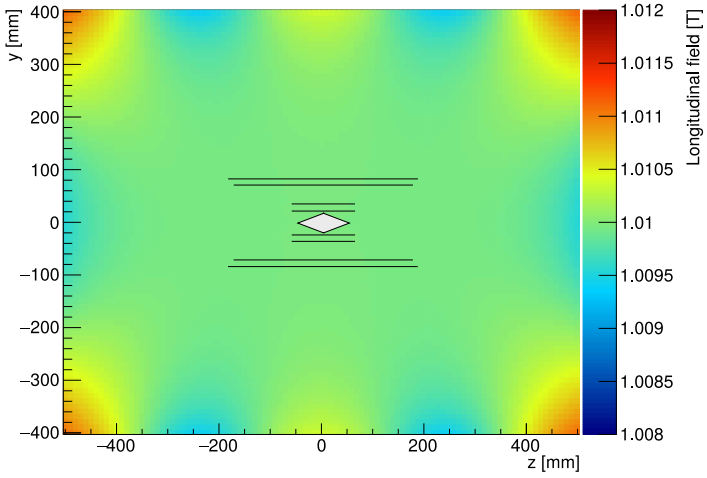

(C) Along the beam axis.

FIGURE 2.13: Expected magnetic field maps displayed as cuts in the global yz-plane inside the *Mu3e* solenoid as used in the simulation. The central detector part is shown for size comparison. Figures taken from [21].

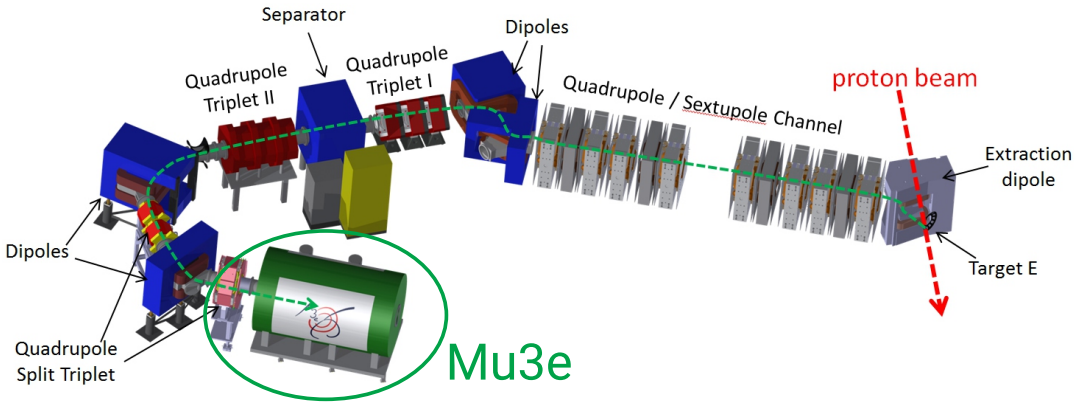

FIGURE 2.14: CAD model of the πE5 channel and compact muon beam line.

[5] which, in turn, are extracted into a separate muon beam line and transported to the experiment. In Figure 2.14 a CAD model of the πE5 beam line, the *Mu3e* detector will make use of, is displayed. To suppress positrons that are produced by π^0 decays in the target or muon decays in flight or at rest, a Wien filter (labelled with "Separator" in Figure 2.14) is placed in the beam line. It separates the positrons from the muons such that an almost pure muon beam can be obtained for *Mu3e*. The in this way provided world's most intense continuous muon beam line is expected to offers - after the planned HiMB upgrade - rates of about $10^{10}\mu/s$ [24]. To reach the ultimate sensitivity goal of *Mu3e* of $1 \cdot 10^{-16}$ in a reasonable time frame, an upgrade like this is crucial. Measuring at least 10^{16} muons at the already available πE5 beam line at PSI with 10^8 μ/s would mean a net data taking time of more than three years. With an estimated duty cycle of 50% and an overall efficiency of about 20% this would add up to about 30 years of data taking which is of course not feasible.

.

2.3 Data Acquisition and Online Reconstruction

The requirement of strong constraints on the signal vertex, timing and the particle trajectories pose a challenge on the trigger and readout system. Each readout frame needs to be fully reconstructed to inspect multiple electron/positron-combinations and checked for possible signal decays. At a muon stopping rate of 10^8 μ/s, more than 80 Gbit s^{-1} of data will be produced [21]. To be able to handle such high data rates, an online reconstruction is implemented to reduce the data rate by selecting signal candidate events.

The continuous data stream is read out by front-end FPGAs. Afterwards the data will be transferred to a data acquisition (DAQ) computer farm consisting of 12 PCs with an FPGA and a GPU each. A DAQ computer's FPGA does a first hit selection and transfers the necessary data to the PC's main memory while continuing to buffer incoming data into the FPGA board. Selected data is transferred to the GPU, where a track and vertex reconstruction will select possible signal candidate events; the rest

is discarded. The complete data of these events is then copied from the FPGA board to the DAQ computer. As a consequence, the data produced can be reduced to below 100 Mbit s^{-1} [21] and can therefore be written to disk for later offline analysis.

For the online selection process to work properly, a precise knowledge about the detector geometry is crucial. Misalignment[9] effects on the selection efficiency have been studied and are presented in [21]. After examining various modes of random misalignments of individual pixel sensors, the dominating modes were found to be rotations around the axes perpendicular to the sensor surfaces and shifts along the beam axis. For average rotation angles of 0.05° (corresponding to a tilt of less than 20 µm), a slight decrease of efficiency of 0.1 % was measured. Average shifts of up to 50 µm on the other hand, did not result in a drop in signal efficiency. However, as will be presented later, the expected sensor misplacement after detector assembly is expected to be much larger than the ones mentioned above. This means that the online reconstruction will probably not work well enough without some sort of alignment algorithm applied beforehand. Since the alignment programme for *Mu3e* is expected to result in a more precise knowledge about sensor positions and orientations (see chapter 5), sensor misalignment does not pose a thread to the online selection efficiency.

2.4 The Mu3e Software Package

In this section, the main components of the *Mu3e* software package will be introduced.

2.4.1 Detector Simulation

The *Mu3e* software package includes a detailed GEANT4 [25, 26] simulation of the detector, the occurring particles, their decay products and their interactions with matter. It is used to study and optimise the detector design, develop track reconstruction and alignment code and to estimate signal efficiency and background rates.

The simulation follows the planned detector geometry outlined in section 2.2. Several decay modes are implemented; the most important ones being Michel decay, radiative decay (with and without internal conversion) and, of course, the signal decay. In addition, a cosmic muon generator based on the spectrum and angle parametrisation of Biallass and Hebekker [27] was implemented. Because of the high energy and unique topology of cosmic muons, their trajectories connect detector parts that are usually not connected by other occurring particles. They assist in counteracting weak modes (section 5.8) in the detector geometry when used in the track based alignment algorithm. Another set of special trajectories comes from Mott scattering electrons and positrons. Compared to the other possible decay particles

[9] More on the programme that produced the misalignment can be found in chapter 4.

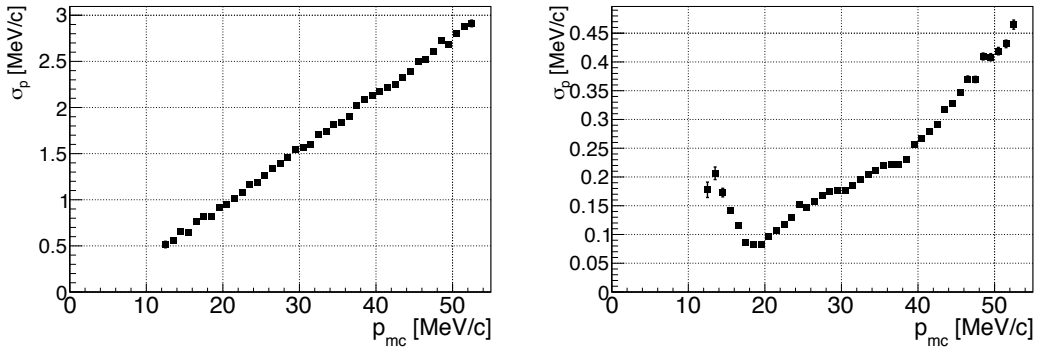

(A) Short tracks, consisting of 4 hits. (B) Long tracks, consisting of 6 or 8 hits.

FIGURE 2.15: Momentum resolution σ_p as a function of true momentum p_{mc}.

they have a high forward momentum, which makes them also valuable for track based alignment.

2.4.2 Track Finding and Fitting

As mentioned before, multiple Coulomb scattering (MS) in detector material is the dominating uncertainty for tracking in *Mu3e*. A fast three-dimensional MS fit [28] is used for tracking. This fit ignores the uncertainties originating from the hit positions, which - as discussed in section 2.2 - is a very good approximation and fits the MS angle at the middle hit of each hit triplet combination.

Track finding is done by inspecting hits in the first three detector layers. Triplets of hits are identified and fit with the fast MS fit if they are consistent with a track originating from the target. If a triplet passes an imposed χ^2-selection, it is extrapolated to the fourth layer, where the presence of an additional hit compatible with the triplet is required. Another fast MS fit is performed followed by another χ^2 cut. The resulting short tracks are used for the online reconstruction and the vertex fit. For the full offline reconstruction, also recurling tracks are used to extend the short track to longer tracks comprised of even more hits each. Figure 2.15 shows the improvement in momentum resolution by utilising recurling long tracks compared to short tracks.

2.4.3 Vertex Fit

The signal consists of three tracks with a common point on the surface of the target. Of these three, one must correspond to a negatively charged particle and the other two to a positively charged particle. Hence, to find a possible signal decay vertex, all combinations of such three tracks must be considered, while making sure not to combine recurling tracks with themselves.

The vertex fit is performed by forcing three tracks to intersect in a common point in space, taking MS only in the first detector layer as the only degree of freedom.

Accidental background can then be suppressed by applying cuts on the χ^2 of the fit and the distance of the vertex to the target surface [29].

2.4.4 Alignment Software

A working alignment software is essential for every experiment, since physics results can only be as good as the alignment allows them to be. Therefore, its development phase has to start early on by utilising the detector simulation. This has the additional advantage of providing the opportunity for identifying possible weak modes (cf. section 5.8) for the alignment early on, which allows for the possibility to counteract them by e.g. finding appropriate alignment strategies or the implementation of external measurement systems.

The backbone of *Mu3e*'s alignment software, MU3EPIXAL, is the track fitting library WATSON [30]. It incorporates a *General Broken Lines* (GBL) track fitter (see section 5.1) optimised for thin sensors like the MUPIX and provides a very useful interface to PEDE (see section 5.3) which in the end performs the calculations needed for gaining alignment corrections. More on this procedure will be presented in chapter 5. The great advantage of using WATSON is its generic nature. It is not only used for the *Mu3e* track fitting and alignment but is also for the *P2* experiment [31] and the alignment of beam telescopes (see section 6.1). In principle, it can be plugged into any application that fits particle trajectories through pixel sensors and is in need of an alignment algorithm. To study misalignment effects and justify the need of an alignment algorithm, the misalignment tool MU3EMISAL has been created. It features various misalignment modes for the pixel detectors as well as the fibre detectors and will be introduced in chapter 4.

Although this thesis only covers the alignment of the pixel detector, work on an alignment of the timing detectors is in progress.

Chapter 3

The Mu3e Silicon Pixel Sensors

The high demands of the *Mu3e* experiment on single hit resolution, digital readout speed and material budget require the use of a novel type of pixel sensors: High Voltage Monolithic Active Pixel Sensors (HV-MAPS). In this chapter, the working principle of semiconductor pixel sensors in general as well as HV-MAPS in particular will be introduced. Subsequently, the MuPix chip, developed especially for the *Mu3e* experiment and its performance, will be discussed.

3.1 Semiconductor Sensors

Every material has a specific conductivity, which is defined by the energy difference between the electrons in the valence band and the ones in the conduction band: the so called *band gap*. A large band gap prevents electrons from travelling from the valence to the conduction band, making the material an insulator. Without a band gap, electrons can travel freely between the two bands, making the material a conductor. The third option is a semiconductor which usually has a band gap of the order of 1 eV; silicon, being the most widely used semiconducting material, has a band gap of ~ 1.1 eV. For band gaps that small, external electric fields or thermal excitation can lead to an electron from the valence band traversing through the band gap into the conduction band. As a result, the valence band has one electron less and the conduction band has one electron more than in their neutral state - an electron-hole pair came into existence. It can move almost freely through the material and therefore act as a charge carrier.

By adding foreign atoms to the semiconductor, additional electrons or holes can be introduced, leading to the semiconductor being of *n-type* or *p-type* respectively, depending on the added atoms. This process is called *doping*. Foreign atoms with one more valence electron than the semiconductor are called *donors* and atoms with one less are called *acceptors*.

Semiconductor sensors exploit the properties of so called *pn-junctions*, i.e. boundaries between differently doped regions in a semiconductor. At this boundary, charge carriers diffuse into the opposite region, recombining with their counterparts and

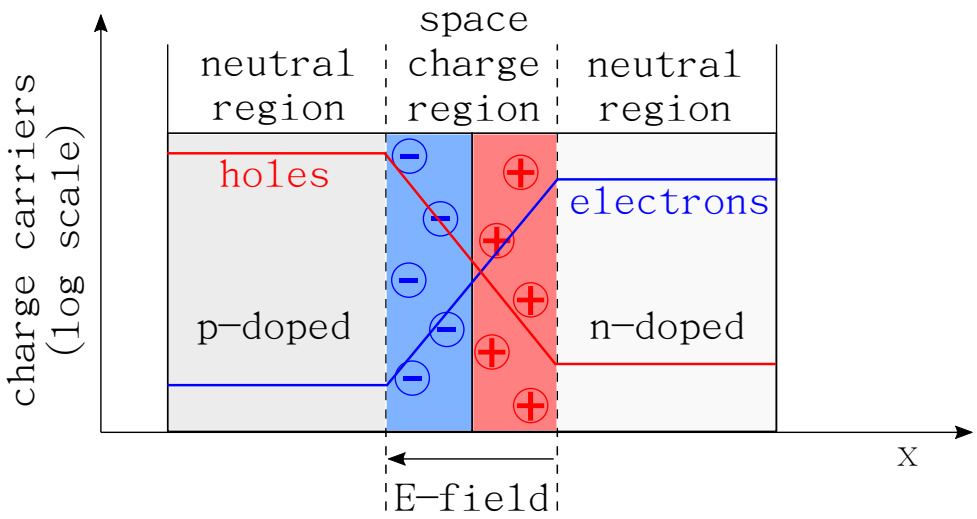

FIGURE 3.1: Schematic of a pn-junction after diffusion of charge carriers. Picture based on [33]

creating a region without free charge carriers: the *depletion zone*. Because of the departure of electrons from the n-doped side, positive donor ions are left behind. Likewise do the holes leave a negative acceptor ion in the p-doped side behind, creating an electric field in the region between the n-doped and p-doped regions - the *space charge region*. Figure 3.1 shows an illustration of a pn-junction after the diffusion.

Charged particles passing through matter deposit energy - mostly through ionisation - creating electron-hole pairs. If such a particle passes through the space charge region of a pn-junction, the electric field forces the ionisation charges to drift to either side of the junction, where they can be detected by localised electrodes. Hence, a very basic sensor for particle detection was created. However, for a sensor like this to be viable for today's particle detectors, a few things have to be modified.

The width of the depletion zone of a semiconductor sensor can be found e.g. in [32] and is given by

$$x = \sqrt{\frac{2\epsilon}{e}\frac{N_A + N_D}{N_A N_D}(U_0 + U_{\mathrm{ext}})}, \tag{3.1}$$

with ϵ being the permittivity, N_A and N_D being the acceptor and donor concentration respectively and e being the electron charge. U_0 denotes the voltage between p- and n-doped region due to the diffusion and U_{ext} denotes an optional externally applied voltage. Hence, the depletion zone width depends on the applied voltage and the dopant concentrations (and implicitly on the substrate resistivity). By applying a large enough external voltage, the whole sensor can be depleted, making the full volume active. Additionally, a large voltage means faster charge collection via drift which, in turn, means faster readout - an effect very much desired for *Mu3e*. An illustration of the working principle of a semiconductor sensor is displayed schematically in Figure 3.2.

For a full sensor configuration, usually a separate chip is needed to process the signals produced by the sensor. These types of sensors are called hybrid (pixel)

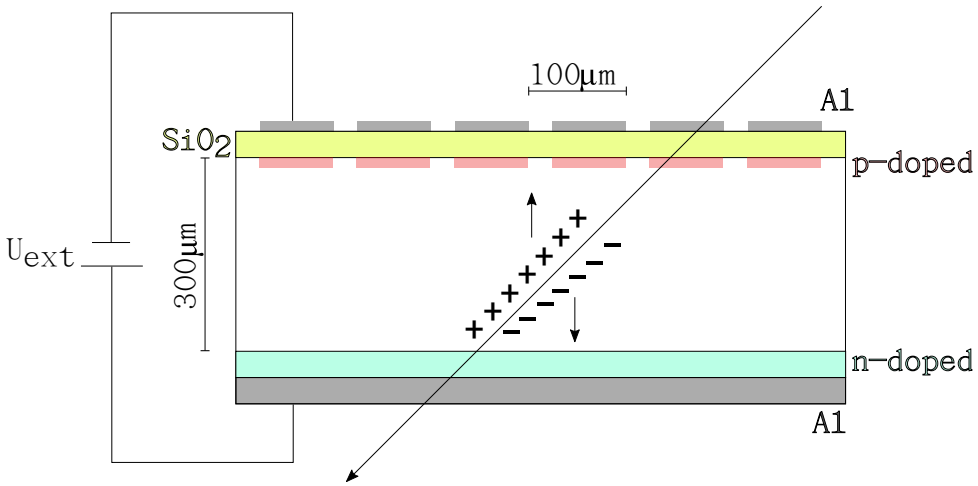

FIGURE 3.2: The working principle of a semiconductor sensor with typical scales and materials. The aluminium electrodes are divided into rectangles with a width of 100 µm (i.e. the pixels) and the depletion zone extends over the full distance between p- and n-doped regions.

sensors. They are widely used in major experiments like CMS and ATLAS at the Large Hadron Collider (LHC). However, with usual total thicknesses of approximately 600 µm and the added high Z material used for bonding the processing logics part with the active part, they are not suitable for the *Mu3e* experiment[1].

3.2 High Voltage Monolithic Active Pixel Sensors

To avoid the high amount of material needed for hybrid sensors, so called *monolithic* sensors, which integrate the active sensor area into the readout chip, were developed. They can be produced in commercial Complementary Metal-Oxide-Semiconductor (CMOS) processes which makes them relatively cheap and accessible. These processes are qualified for "high" voltages of up to 120 V, making a fast charge collection via drift possible. Figure 3.3 illustrates the layout of an HV-MAPS, where a deep n-doped well is sitting in a p-doped substrate. By applying a bias voltage between the substrate and the wells, a depletion zone is created around the n-wells, defining the sensitive volume of the sensor. Thanks to the possibility of applying high voltages, depletion zones of $10 - 20$ µm thickness are possible (for silicon based chips with an appropriate resistivity). Since the p-substrate is not depleted, the sensor can be thinned down from the back, allowing for total thicknesses of down to 50 µm which corresponds to 0.05 % of the radiation length. The HV-MAPS technology was developed by Ivan Perić [34]; they will not only be used by *Mu3e*, but might also be used in various other future upgrades or experiments (e.g. ATLAS, *P2* [31], Compton polarimetry at JLAB and the Panda Luminosity Detector [35]).

[1] As mentioned before, a very low material budget is a key ingredient for the *Mu3e* experiment to succeed.

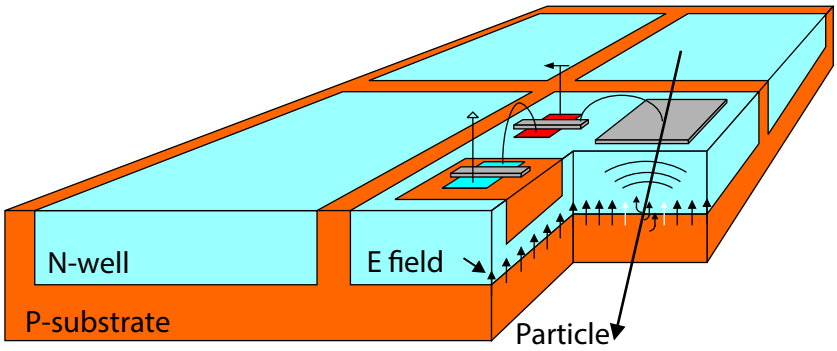

FIGURE 3.3: Four pixel cells of an HV-MAPS where one exemplarily hosts additional circuits. Figure taken from [18].

3.3 The MuPix Chip

The MUPIX prototypes are implementations of the HV-MAPS technology specifically designed in the context of the *Mu3e* experiment. After submitting the first proof-of-principle demonstrator in 2010, different prototypes with different pixel sizes, overall dimensions and functionality have been developed over the years, arriving at the most recent one: the MUPIX8. It is manufactured by Austria Mikro Systeme (AMS) in an HV-CMOS 180 nm process and first prototypes are being evaluated since fall 2017.

The MUPIX8 is about $1 \times 2\,\mathrm{cm}^2$ in size and consists of 128×200 pixels with a pitch of $81 \times 80\,\mu\mathrm{m}^2$. This makes up a $16 \times 10\,\mathrm{mm}^2$ active area (covering over 75 % of the total sensor surface) which is divided into three submatrices with a dedicated data output each. Exact measurements can be found in the layout depicted in Figure 3.4 and the pixel electronics and readout state machine for each pixel and submatrix respectively can be seen in Figure 3.5.

Each pixel contains a sensor diode which generates a voltage pulse to be afterwards amplified by a charge sensitive amplifier. The amplified signal is then driven to the digital periphery located at the bottom of the chip (cf. Figure 3.4), where a digital readout cell is implemented for each pixel. It is comprised of two comparators[2] with adjustable thresholds that allow not only the setting of a global threshold, but also a fine adjustments for individual pixels. The digitised signal is then fed into the state machine which exists once for each chip submatrix. It sends out the 8b/10b encoded [36] serialised zero-suppressed signal via a *low-voltage differential signal* (LVDS) link.

[2] A second comparator adds additional possibilities for time walk correction.

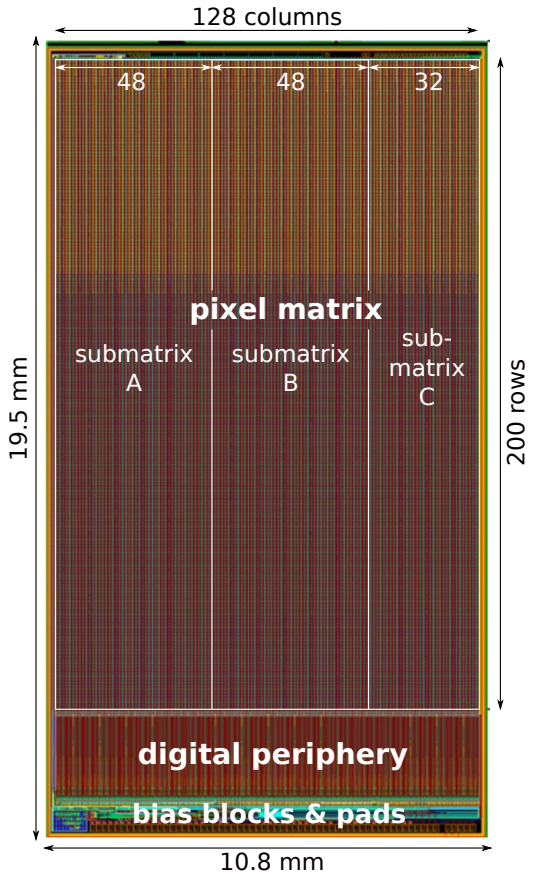

FIGURE 3.4: Layout of the MUPIX8 prototype.

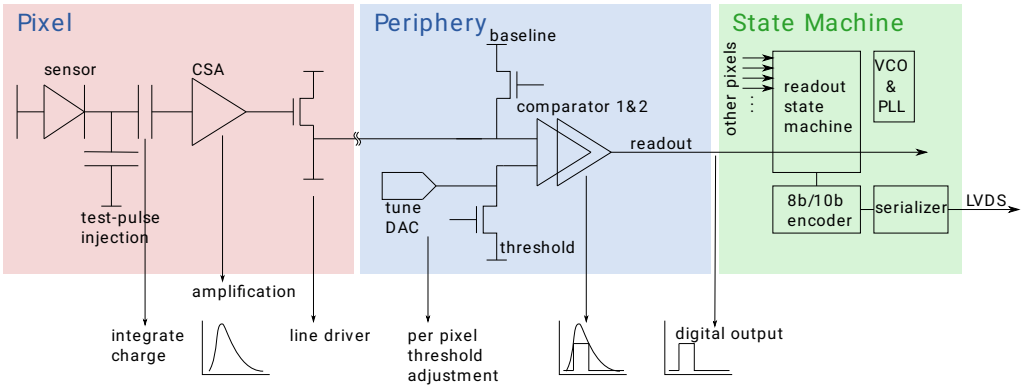

FIGURE 3.5: Schematic depiction of the pixel electronics and readout state machine of the MUPIX8. The "Periphery" parts are included once for every individual pixel, whereas the state machine exists once per submatrix.

3.3.1 Prototype Studies

The characteristics and performances of sensor prototypes have to be studied in various regards before producing chips in large quantities for the pixel tracker. Extensive measurements have been carried out at different testbeam facilities[3] to study the properties of each MUPIX prototype. In the following, some of the latest results of these studies for the MUPIX8 will be presented, the data for which was gathered at the DESY testbeam facility with an $\sim 4\,\text{GeV}$ electron beam.

Figure 3.6a shows an efficiency map of the MUPIX8, i.e. a measurement of the detection efficiency of individual pixels in each column and row of the sensor. It shows that the sensor efficiency is evenly distributed over the sensitive surface and above 90 % in every single pixel. The overall detection efficiency can be found in Figure 3.6b, where the efficiency and the noise as a function of applied threshold is displayed. Efficiencies of over 99.5 % at noise rates of less than 0.3 Hz per pixel are possible. Individual pixels with extraordinarily high noise affect the efficiency at lower thresholds. Masking these pixels means lowering the noise rate by sacrificing a bit of efficiency at the same time. However, Figure 3.6c shows, the decline is negligible in comparison to the improvement gained in overall noise rate.

Due to charge sharing between neighbouring cells, a single particle can prompt multiple pixels to send a signal. These clusters of hits can complicate the alignment procedure. A similar problem arises from crosstalk, the phenomenon of one electronics circuit interfering with another. In a pixel sensor, this can lead to pixels firing without actually detecting a particle passing through them, simply because of cross talk. Figure 3.7a shows that lower threshold leads to higher crosstalk probability.

However, in terms of alignment, crosstalk and clustering are not expected to be a concern. To the contrary, clusters that emerged due to charge sharing, have an even improved hit resolution since the position of the particle that created the signal, is better localised. The strong suppression of clustering in the MUPIX8 chip displayed in Figure 3.7b is due to the thin active material compared to the pixel size and the fast charge collection, allowing charge sharing between neighbouring pixels essentially only at the very edge of each cell. Crosstalk on the other hand can in general pose a minor problem for alignment, since it introduces a track reconstruction ambiguity. However, this can be identified and corrected for in analysis which makes its effects negligible.

The power consumption of individual sensors plays an important role with regards to the cooling of the whole detector. Studies have shown that the MUPIX8 can be operated efficiently with a power consumption of $\sim 210\,\text{mW}\,\text{cm}^{-2}$ which lies well within the cooling capabilities of the final detector design specified to up to $400\,\text{mW}\,\text{cm}^{-2}$ [37].

These results - together with the single-hit-resolution of $\sim$ 23.2 µm - constitute an excellent basis for the *Mu3e* experiment and its alignment algorithm.

[3] Among them are MAMI in Mainz, DESY in Hamburg and PSI in Villigen, Switzerland

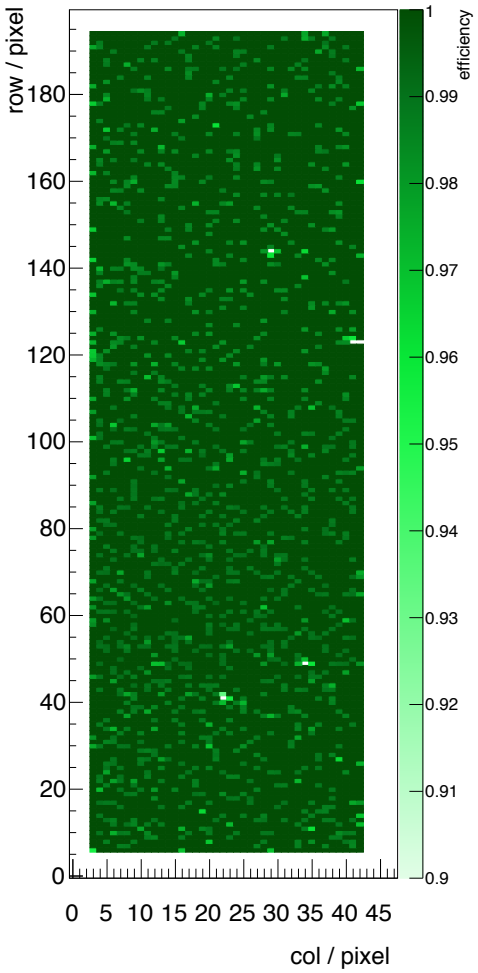

(A) Efficiency map of the whole sensor

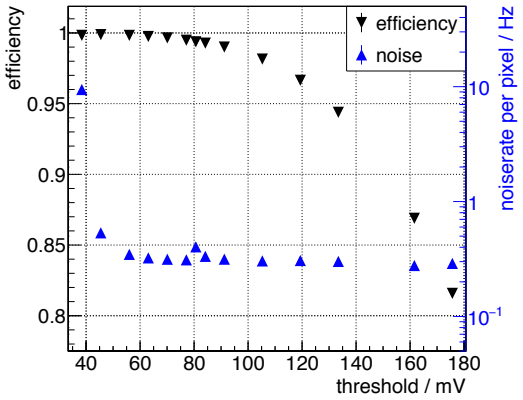

(B) Efficiency and noise rate as a function of threshold

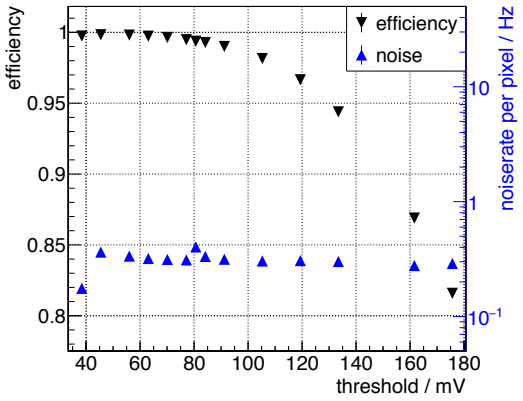

(C) Corrected (by masking noisy pixels) efficiency and noise rate as a function of threshold

FIGURE 3.6: Exemplary efficiency measurement results for the MUPIX8 prototype. Figures taken from [17].

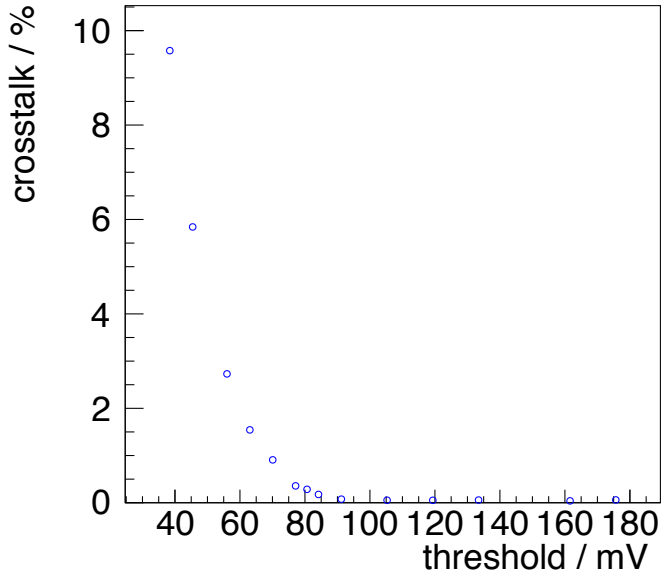

(A) Fraction of pixels firing due to cross talk

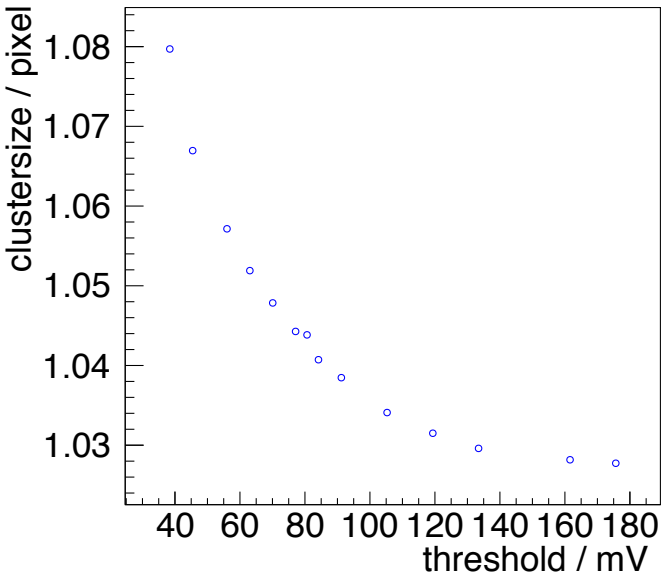

(B) Cluster size, corrected for cross talk

FIGURE 3.7: Exemplary measurement results for the MUPIX8 prototype. Figures taken from [17].

Chapter 4

Misalignment

The construction of a particle detector is an extremely demanding task. It requires working on a very high level of precision during detector assembly. For the tracking detector, almost 3000 MuPix chips have to be glued on *High Density Interconnects* (HDIs). Multiple sensors will be glued on the same support structure to build up so called *ladders*. Four or five (depending on which barrel layer they belong to) of them will be assembled to modules or half-shells. These modules and half shells make up the final detector layers. As mentioned before, the *Mu3e* detector is (in its first phase) divided into three stations. The central detector station, consisting of two (small) inner and two (large) outer layers is situated around the target. Up- and downstream of the central station, two recurl stations, each consisting of two large layers, are located. A schematic view of the hierarchical structure of the *Mu3e* tracking detector is depicted in Figure 2.10. In a perfect world, every single detector part would end up exactly where it was supposed to. But in the real world, there is only a limited mechanical assembly precision. Additionally, there are environmental factors which influence the detector geometry (over time), like thermal expansion or gravitational effects. All of this means that detector parts will - in general - not end up at their nominal positions. These misplacements are summarised by the term *misalignment*.

In this chapter, various misalignment modes and their implementation into the *Mu3e* software framework will be discussed and their effects on the performance of the track reconstruction will be investigated.

4.1 Misalignment Modes

When preparing the alignment algorithm, one has to think about the magnitude of the misalignment and its effect on the detector performance that has to be faced. Estimating a realistic misalignment for a complex structure such as the *Mu3e* detector is a challenging task. Starting from the lowest hierarchy possible, which is the individual sensor, going up to complete detector movements or deformations, thousands of different combinations of misalignment modes are possible. Since individual detector entities, such as sensors, ladders, modules, and layers are expected to experience only small offsets with respect to the larger entities they are part of, the hierarchical

Relative misalignment	$\sigma_{\texttt{off,x,y}}$ in µm	$\sigma_{\texttt{rot,x,y}}$ in mrad	$\sigma_{\texttt{off,z}}$ in µm	$\sigma_{\texttt{rot,z}}$ in mrad
sensors vs. ladders	50(100)	5(10)	5(100)	5(10)
ladders vs. modules	150(300)	1(2)	150(300)	1(2)
modules vs. layers	150(300)	1(2)	150(300)	1(2)
layers vs. layer pairs	25(50)	0.2(0.2)	50(50)	0.2(0.2)
layer pairs globally	150(300)	1(2)	250(300)	1(2)

TABLE 4.1: Expected misalignment scenario after detector construction. The depicted values represent realistic estimates for the standard deviation of the Gaussian distribution used for misalignment. In parentheses, the expected worst case is given. It is used to truncate the Gaussian. Additionally, sensors are expected to have surface deformations which translate to roughly 50 µm average deviations from a flat sensor. For individual sensors, local coordinate systems are defined, for composite parts, the global coordinate system is used.

structure displayed in Figure 2.10 will be reflected in a realistic misalignment scenario. Such a scenario is obtained by estimating the expected error on each entity and modifying the nominal (simulated) geometry by random Gaussian distributed values which reflect these error estimates. However, these random misplacement of a detector component can lead to outliers not expected for the real-life detector. There is a lower limit for the mounting precision of components. Therefore, the Gaussian distributions used for misalignment have to be truncated. Table 4.1 displays the error estimates and the values at which they are truncated that will be used in the following[1].

It is crucial to study the effects such a scenario will have on the detector performance. Therefore it has been implemented into the *Mu3e* software framework as follows.

4.1.1 Misalignment in Software

Rather than to apply the misplacements at the simulation level, it has been decided to carry them out at the reconstruction level to save computing time[2]. Thus, a geometrical movement of detector parts will only move hits but can not remove hits that should not have been detected in the first place because of misalignments. However, such drastic results are expected to be negligible, since it is not expected that displacements can, for instance, lead to a loss of sensor overlap. The application of misalignment after simulation has the additional advantage of preventing volume overlap in GEANT4.

[1]The position uncertainty of the pixels inside the sensors are ignored here, since it is much better than the minimal feature size of 180 nm

[2]Starting at the simulation level would take about a factor of 12 longer to process than starting at the reconstruction level.

Detector Entity	Misalignment Modes
barrel layers	shifts, rotations, torsion, radial scaling
central inner layers	shifts, rotations, torsion, radial scaling
central outer layers	shifts, rotations, torsion, radial scaling
recurl stations	shifts, rotations, torsion, radial scaling
half shells	shifts, rotations, torsion, radial scaling
modules	shifts, rotations
ladders	shifts, rotations
individual sensors	shifts, rotations, torsion, surface deformations, temperature scaling

TABLE 4.2: Pixel detector parts and their corresponding misalignment modes.

In the context of this thesis, *Mu3e*'s very own misalignment tool MU3EMISAL was developed. Table 4.2 displays the misalignment modes which are currently possible via this tool. They are applied by modifying the nominal positions and orientations by Gaussian distributed random[3] values with the given standard deviations. As discussed before, a simple Gaussian distribution will in general not reflect a real-life scenario. Therefore the Gaussians are truncated by setting an upper bound for the random number generator. For composite detector parts (i.e. any entity mentioned in Table 4.2 larger than a single sensor), the global coordinate system $(\hat{\mathbf{x}}, \hat{\mathbf{y}}, \hat{\mathbf{z}})$, where $\hat{\mathbf{z}}$ is parallel and $\hat{\mathbf{x}}$ (horizontal) and $\hat{\mathbf{y}}$ (vertical) are perpendicular to the beam axis, building a right-handed coordinate system, is used to apply misalignments. At the sensor level, a local coordinate system is defined by the unit vectors $\hat{\mathbf{u}}$, $\hat{\mathbf{v}}$ and $\hat{\mathbf{w}}$, where $\hat{\mathbf{u}}$ and $\hat{\mathbf{v}}$ are defined along two adjacent edges of the sensor and $\hat{\mathbf{w}}$ perpendicular to it. Shifts and rotations are then defined along and around the coordinate axes respectively where the entity's centre of mass is used as the rotational centre. Sensor surface deformations are produced with the help of Legendre polynomials parameterised by seven numbers (see subsection 5.5.2). Temperature scaling of individual sensors is done by adding two numbers that stretch or contract the sensor in $\hat{\mathbf{u}}$- and $\hat{\mathbf{v}}$-direction. The "torsion mode" corresponds to a rotation around the z-axis proportional to the distance to the centre of mass of the corresponding entity and "radial scaling" describes the change of layer radii.

[3]The (pseudo) random numbers are produced by utilising ROOT's TRandom3 class [38].

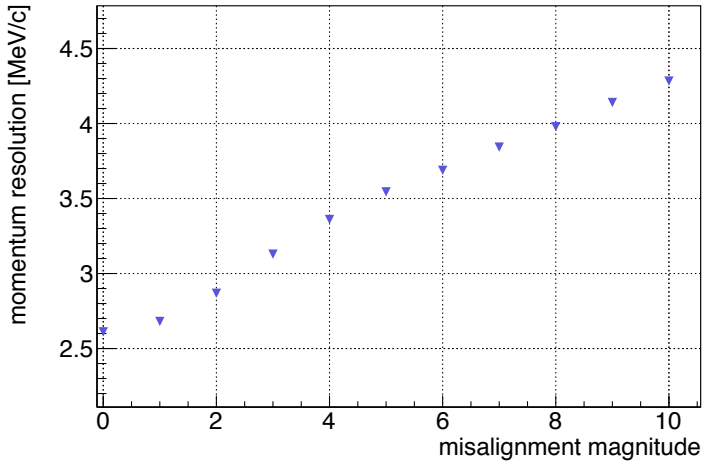

(A) Momentum resolution from RMS of the difference between reconstructed and true momentum.

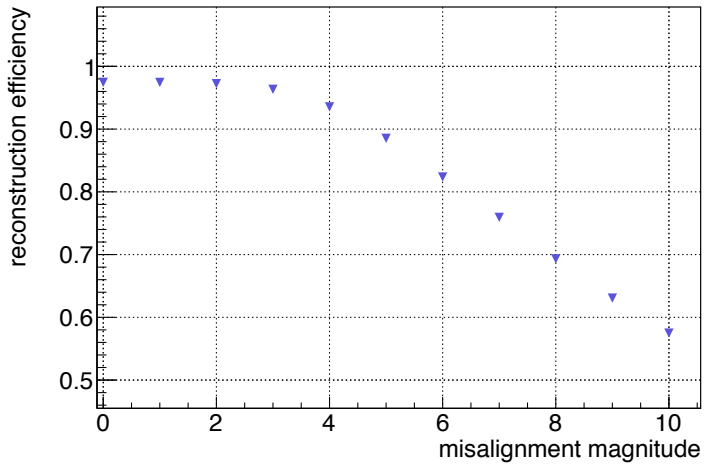

(B) Momentum reconstruction efficiency.

FIGURE 4.1: Momentum resolution and reconstruction efficiency for short tracks (consisting of 4 hits) as a function of various misalignment magnitudes.

4.2 Effects on the Tracking Performance

To utilise a track based alignment algorithm, reconstructed tracks are essential. The larger the number of available tracks, the smaller the statistical error on the alignment corrections will be. Furthermore, it is vital for these tracks to be reconstructed with a good precision to prevent too many alignment iterations (and therefore save time).

4.2.1 Effects for Realistic Misalignment Estimates

The effects of various misalignment scenarios, derived from the realistic estimate in Table 4.1, on tracking efficiency and momentum resolution have been studied and

an excerpt of the results is shown in Figure 4.1. As a measure of misalignment, a *misalignment magnitude* is defined. A magnitude of 0 corresponds to the nominal detector geometry and all misplacements are being increased in consistent steps to reach the full realistic estimate introduced in Table 4.1 at magnitude 10.

For the realistic scenario, about 40 % of overall efficiency is lost, whereas the momentum resolution is degraded by almost a factor of two. These results are useful in various respects:

Show the importance of an alignment algorithm: One can derive that some sort of alignment algorithm is necessary to achieve sufficient momentum resolution and reconstruction efficiency. As mentioned in chapter 2, an excellent momentum and mass resolution is vital for background suppression and according to Figure 4.1a, misalignment has severe repercussions on these parameters. *Mu3e*, being a high precision experiment, relies on large statistics, which of course, would be diminished by a lower reconstruction efficiency. Since the signal corresponds to three electrons being detected, the reconstruction efficiency enters at third power for signal events. Although, in reality, one would open up the cuts applied into track reconstruction to achieve higher efficiencies, this has not been done for the depicted results, to have a clear indicator of how important a correct alignment actually is for track reconstruction.

Derive a demand on the alignment algorithm: Figure 4.1 also shows that the alignment algorithm needs to be able to work under the depicted suboptimal conditions and improve from there. Despite of the fact that, for the realistic scenario, efficiency is down to $\sim 58\,\%$, there are still reconstructable tracks available to utilise in a track based alignment. The worsening in reconstruction resolution, however, means that an iterative approach is necessary to gain more tracks with better resolution in each alignment step. In chapter 5 it will be shown that this, indeed, leads to a satisfying result.

Aside from the effects on the momentum resolution and reconstruction efficiency, there is the obvious hit position misplacement. In Figure 4.2 the average absolute three dimensional offset of one corner of a sensor is depicted as a function of the misalignment magnitude used in Figure 4.1. Deviations of more than 400 µm - corresponding to five times the pixel size - are expected, which would be a problem for a decent track and vertex reconstruction and background suppression.

The effects, these misalignment scenarios have on the signal reconstruction can be seen in Figure 4.3. For misplacements smaller than a misalignment magnitude of 1, the deterioration in vertex resolution, mass resolution and signal efficiency are marginal. This sets a goal for the alignment algorithm: reaching a level of misplacements corresponding to a misalignment magnitude of smaller than 1, i.e. absolute offsets of smaller than 50 µm. Although it is not expected that the misplacements left after alignment are evenly distributed to resemble a misalignment magnitude, this is a - rough but - reasonable milestone to set.

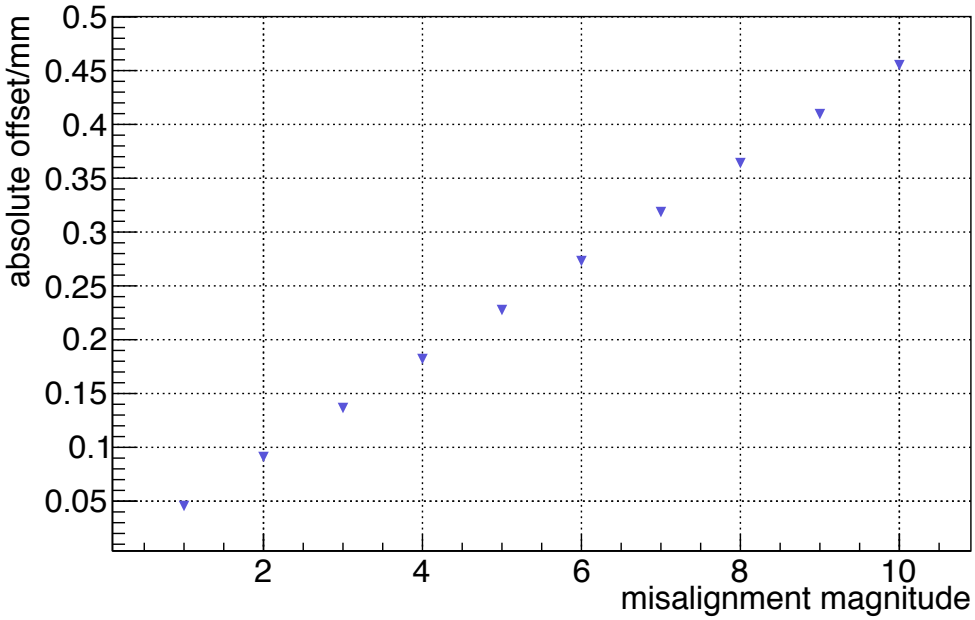

FIGURE 4.2: Average absolute offset at a sensor corner for each misalignment magnitude. The values were obtained by calculating the absolute three-dimensional deviation at the corner of a sensor (depicted here is one of the four corners, the others are very similar and can be found in Figure A.3) from their nominal positions.

4.2.2 Effects for Misalignments of Composite Detector

According to "Murphy's Law" anything that can go wrong will go wrong. That means that aside from the estimated misalignment scenarios, during construction, hall access, magnet ramping etc. it might happen that individual detector parts get misplaced as a whole. Although, it is not feasible to think up and analyse all possible misplacements in this scope, a few possibly interesting modes have been studied. Among them are the effects of misplacements of the recurl stations and the vertex layers on signal reconstruction; plots of the corresponding results can be found in Appendix A, particularly in Figures A.5 to A.8.

For "reasonable" misplacements of the recurl stations, no significant effects on signal reconstruction efficiency, vertex resolution and mass resolution were found. However, movements of the recurl stations in the order of hundreds of micrometres along the beam direction deteriorate the reconstructed muon mass by up to $0.1\,\mathrm{MeV}/c^2$ (see Figure 4.4). A stretching of the detector will lead to an enlargement of the reconstructed mass, whereas a squeezing generates a reconstructed mass that is too small. This is expected, since a higher muon mass would lead to more energy for the decay particles which, in turn, leads to recurl hits further away from the decay vertex. Misplacements of the vertex layers perpendicular to the beam direction don't have a large effect on signal reconstruction (see Figure A.8). However, movements along the beam direction affect the signal significantly (see Figures 4.5

and A.7). More results of the carried out misalignment studies can be found in Appendix A.

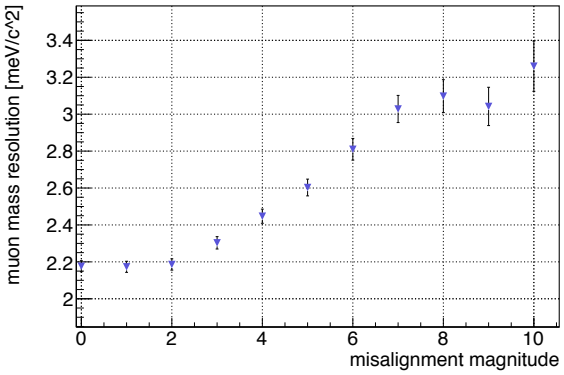

(A) Reconstructed muon mass resolution from RMS of mass recounstruction.

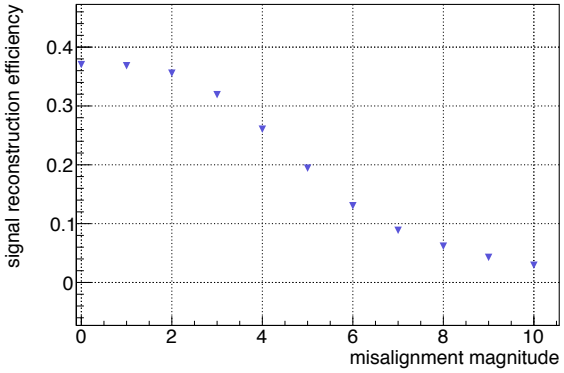

(B) Signal reconstruction efficiency.

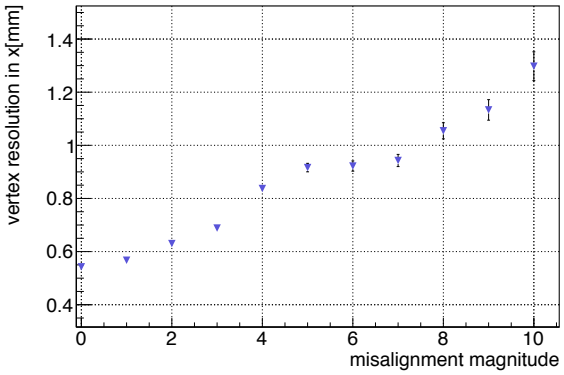

(C) Vertex reconstruction resolution in x from RMS of reconstructed vertex position.

FIGURE 4.3: Misalignment effects on signal reconstruction. The drops occurring in the resolution plots starting from misalignment magnitude 6 are due to selection effects caused by the very low efficiency (Figure 4.3b). For reasons of clarity and comprehensibility, only the vertex resolution in x is given here. The other dimensions of the vertex resolution can be found in Figure A.4. The data given here was obtained by using short tracks for the efficiency calculation and not requiring recurlers for the resolutions.

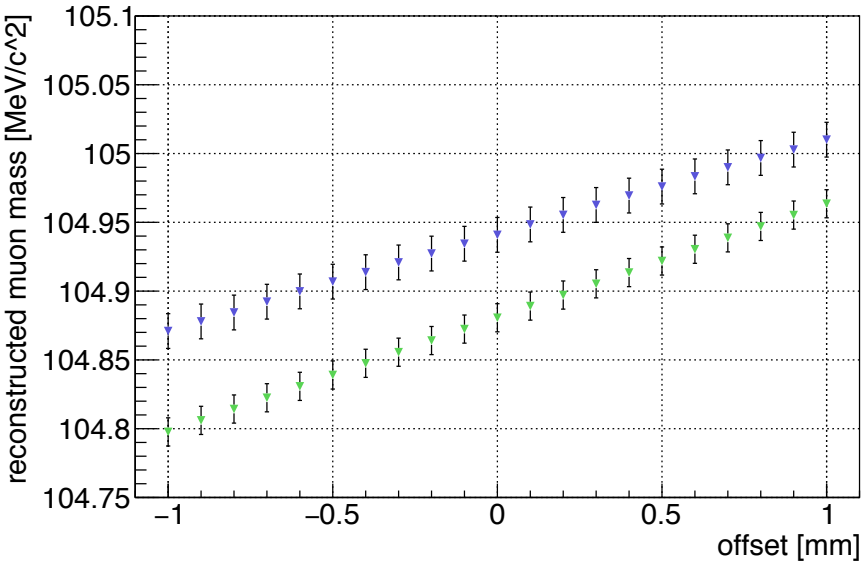

FIGURE 4.4: Reconstructed muon mass as a function of systematic misplacements of the recurl stations for utilising only long tracks (green) and for all possible tracks (blue) for reconstruction. The stated offsets correspond to the systematic misplacement of both recurl stations simultaneously towards each other (along beam direction). Hence, a negative offset corresponds to a "stretching" and a positive offset to a "squeezing" of the detector.

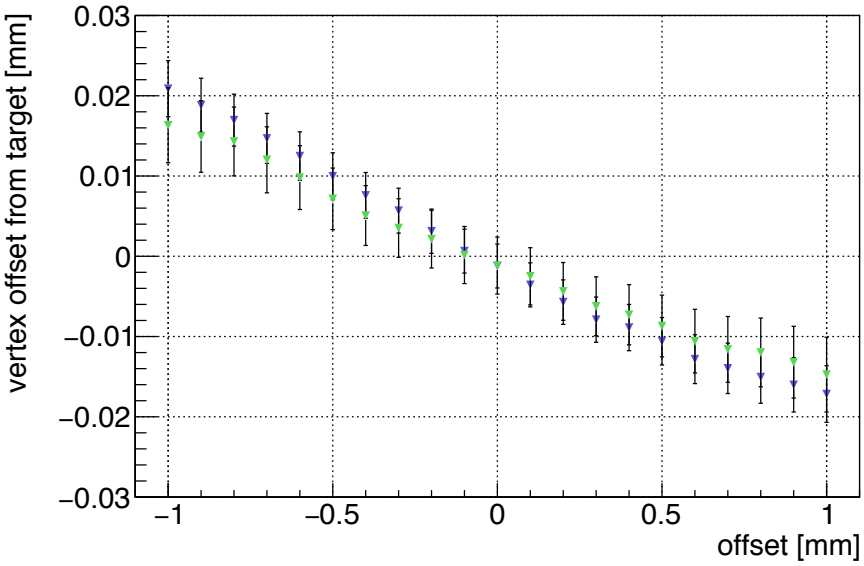

FIGURE 4.5: Three dimensional distance between reconstructed vertex position and target surface for using only long tracks for reconstruction (green) and for all possible tracks (blue). The stated offsets correspond to the systematic misplacement of vertex layer along beam direction.

Chapter 5

Alignment

In order for the track reconstruction to work properly, the positions, orientations and surface structures of all detector parts must be known to great precision. The error on the pixel positions inside a sensor is given by the tolerance of the manufacturing process and is estimated to be better than 180 nm. Compared to other sources of misalignment this is completely negligible.

The careful assembly of the modules and layers with precision tools is of course the first step towards reaching an adequate alignment. Even in the best case scenario, the single sensor alignment after detector construction cannot be expected to be better than several tens of micrometres. Hence, more involved alignment strategies will have to be applied. In this chapter, the alignment procedure that is planned to be used in the *Mu3e* experiment and the included tools will be introduced. Although this work will focus solely on the alignment of the tracking detector consisting of silicon pixel sensors, some of the presented techniques will be applied to other detector parts like the timing detector[1].

5.1 The General Broken Lines Fit

For tracking and track finding, *Mu3e* will use a three-dimensional MS fit (see subsection 2.4.2). However, for alignment purposes, the General Broken Lines Fit (GBL) [40, 41] was implemented.

Multiple Coulomb scattering (as discussed in section 2.2) causes particles passing through matter to change their direction. This means that their trajectories through detector material in a magnetic field cannot be described by a simple helix and a more involved track model is needed. One of these models is the GBL. It is a track refit that adds the effects of multiple scattering to a seed track and provides the complete covariance matrix of all track parameters. Since this is a requirement for performing a track based alignment with MILLEPEDE-II (see section 5.3), GBL is the programme of choice for the track based alignment for *Mu3e*.

The general description of the GBL is schematically depicted in Figure 5.1. The seeding track parameters at some reference point (the first measured point on the

[1] However, these procedures will not be covered in this thesis as they are still in development as part of a different thesis [39].

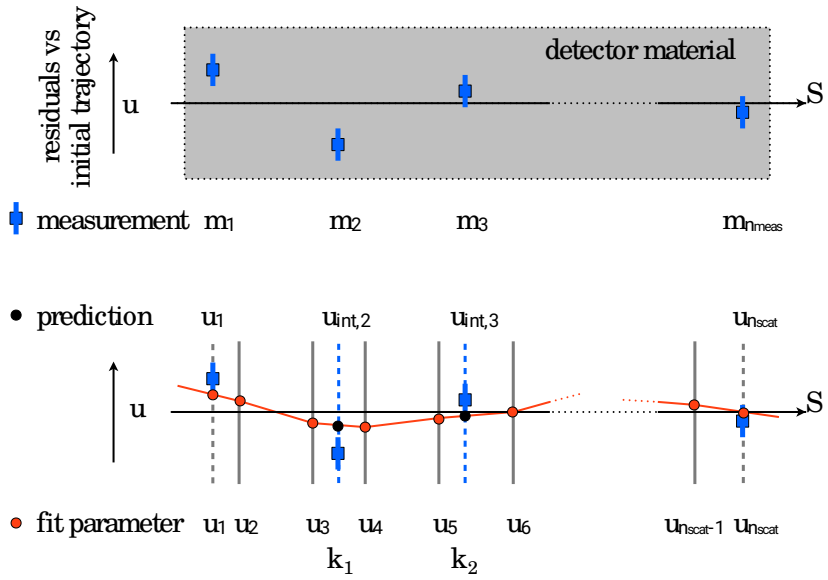

FIGURE 5.1: Simple example for the GBL trajectory, based on [40]. Top: The residual, i.e. the difference between measurement (blue) and initial trajectory, versus the trajectory is depicted. Bottom: Between all measurements, two thin scatterers are added, implying two offsets (red). These offsets are used as fit parameters to interpolate a hit prediction at each measurement plane. The first and last hit define additional offsets to define a start and an end of the trajectory.

trajectory is an obvious choice) are used to calculate an (undisturbed) helix trajectory (called S in Figure 5.1) through the magnetic field. At each measurement plane, i.e. pixel sensor, a two-dimensional residual $\boldsymbol{r}$ can be defined as the difference between the local coordinates of the trajectory at the plane and the measured hit. By adding a thick scatterer - consisting of up to two thin scatterers[2] - per plane, two-dimensional offsets u_i can be defined in the curvilinear system[3]. These offsets, together with a correction on the inverse momentum $\Delta q/p$, are used as fit parameters $\boldsymbol{x} = (\Delta q/p, \boldsymbol{u}_1, \boldsymbol{u}_2, ..., \boldsymbol{u}_{n_{\mathtt{scat}}})$ and allow the interpolation of predictions on the j'th measurement plane $\boldsymbol{u}_{\mathtt{int},j}$. New residuals can now be defined as

$$\boldsymbol{r}'_i = \boldsymbol{r}_i - \boldsymbol{P}_i \, \boldsymbol{u}_{\mathtt{int},i} \tag{5.1}$$

with the projection

$$\boldsymbol{P}_i = \frac{\partial \boldsymbol{r}_i}{\partial \boldsymbol{u}_i} \tag{5.2}$$

from the curvilinear system at i to the corresponding measurement plane.

Furthermore, for $n_{\mathtt{scat}}$ thick scatterers, $n_{\mathtt{scat}} - 2$ two-dimensional kinks $\boldsymbol{k}$ can be defined, describing the changes of the trajectory slope at each "inner" scatterer (cf. Figure 5.1). A χ^2-function to be minimised can be defined as a combination of a

[2]For the thin MUPIX chips, one thin scatterer per sensor suffices.

[3]The curvilinear system [42] is a local coordinate system, travelling with a particle along its trajectory. Offsets in the curvilinear system are defined with respect to the particle position and perpendicular to its current direction.

χ^2_m from the measurements, i.e. residuals, and a χ^2_k from the kinks:

$$\chi^2(\boldsymbol{x}) = \chi^2_m + \chi^2_k \tag{5.3}$$

$$= \sum_{i=1}^{n_{\mathtt{meas}}} \boldsymbol{r}_i'^T \, \boldsymbol{V}_{m,i}^{-1} \, \boldsymbol{r}_i' + \sum_{i=2}^{n_{\mathtt{scat}}-1} \boldsymbol{k}_i^T \, \boldsymbol{V}_{k,i}^{-1} \, \boldsymbol{k}_i, \tag{5.4}$$

with the covariance matrices $\boldsymbol{V}_{k,i}$ and $\boldsymbol{V}_{m,i}$ and $\boldsymbol{x} = (\Delta q/p, \boldsymbol{u}_1, \boldsymbol{u}_2, ..., \boldsymbol{u}_{n_{\mathtt{scat}}})$.

Following the derivation in Appendix B, this χ^2-function can be transformed into a matrix equation. To build the matrix in question, the derivatives of all residuals $\boldsymbol{r}_i'$ and all kinks $\boldsymbol{k}_i$ with respect to the associated track parameters are needed. But since the residual of trajectory point i only depends on the parameters $\boldsymbol{u}_{i-1}$, $\boldsymbol{u}_i$, $\boldsymbol{u}_{i+1}$ and $\Delta q/p$, the resulting matrix will be a bordered band matrix of size $n_{\mathtt{scat}}$ with a band width of $b \leq 5$ and a border width of 1. By using root free Cholesky decomposition [43], the matrix equation can be solved in a computing time proportional to $n_{\mathtt{scat}} b^2$ [44].

A more detailed description of the mathematics behind the GBL can be found in e.g. [40].

5.2 Track Based Alignment

When aligning a detector, a common procedure is to look at individual particle tracks. After fitting them with an adequate track model, one can define so called *residuals*[4], i.e. the difference between the measured hit and its corresponding prediction obtained from the fit. From these *residuals*, one can derive geometry corrections; a simple example is schematically depicted in Figure 5.2.

These track fits however assume a fixed set of *global parameters*[5] and therefore depend only on a small set of parameters like the hit positions, the inclination angles or the curvature of the track. As a result, the obtained *residuals* will be biased; they depend on a wrong model, assuming fixed global parameters. Despite that, they can be used to obtain an estimate for the global parameters which, in turn, will lead to a biased geometry. To minimise this effect, the described procedure is usually applied iteratively. However, it is not clear if and when this method will converge.

The idea of using track residuals for alignment purposes can be used to develop a much more involved alignment method by including all global parameters into the track fits and fitting them all at the same time as the track parameters. This way the track fits are not biased, since they do not assume fixed global parameters, but instead use them as fit parameters.

[4]Not to be confused with the residuals defined for the GBL in section 5.1.

[5]Global parameters describe the position, orientation and surface structure of individual detector parts leading to a complete geometrical description of the detector.

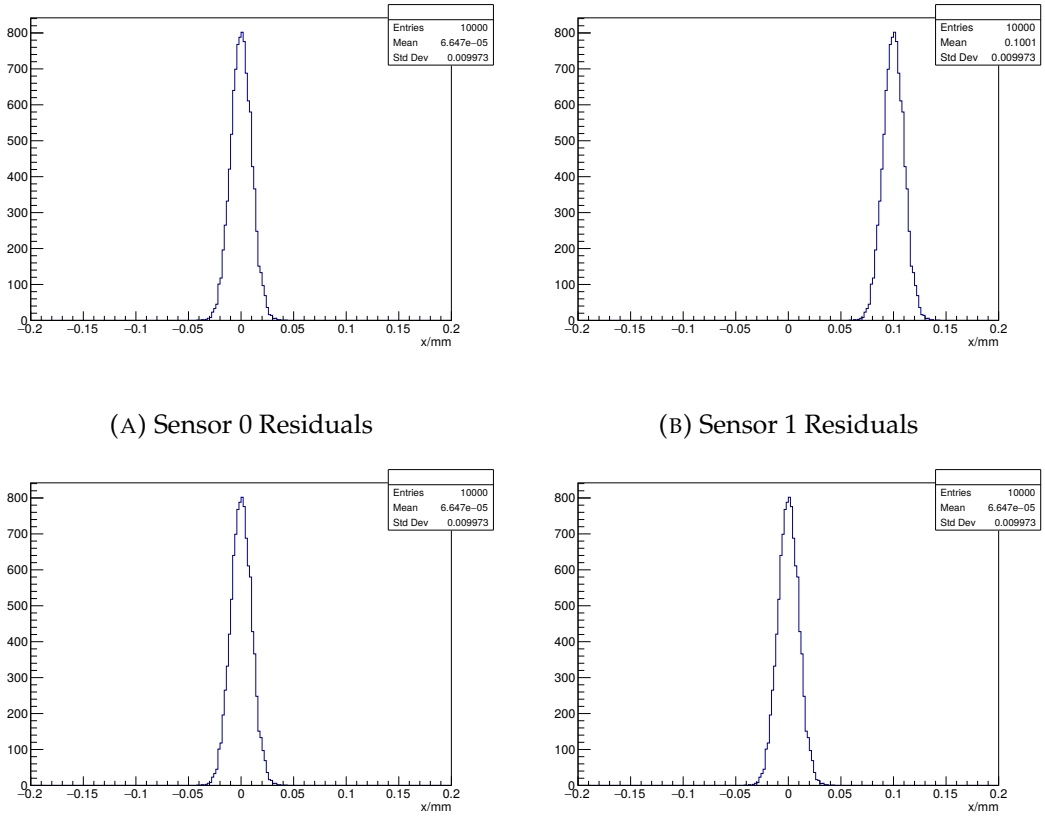

(A) Sensor 0 Residuals (B) Sensor 1 Residuals

(C) Sensor 2 Residuals (D) Sensor 3 Residuals

FIGURE 5.2: Schematic depiction of a histogram based alignment procedure. Depicted are track residuals on four sensors. Here it seems, sensor 1 has to be moved by 100 µm in x-direction to achieve a minimisation of the residuals. This is of course not the only option to achieve the goal of minimisation, but probably the most visceral one.

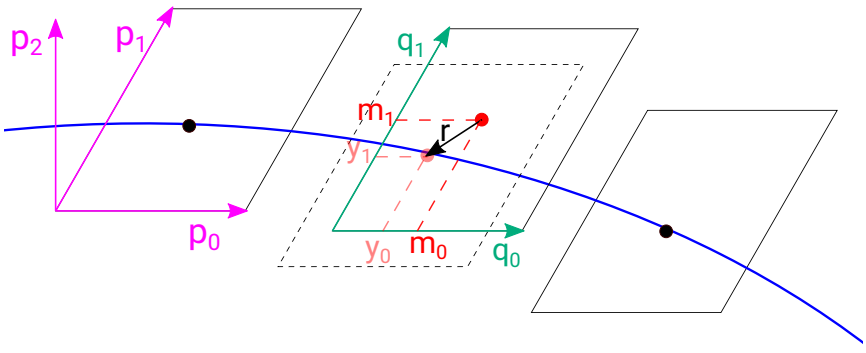

FIGURE 5.3: A schematic depiction of a particle traversing three sensor planes. On the left one, a possible local coordinate system for alignment corrections is depicted (magenta). It represents one set of global parameters. On the middle one, local track parameters (green), the measured hit position (red) and the predicted hit position (light red) are displayed. The resulting (two dimensional) residual r is marked with a black arrow.

For each reconstructed track, a residual can be defined as the difference between measured hit and a predicted hit position:

$$r_{ij} = m_{ij} - f(\boldsymbol{q}_j, \boldsymbol{p}). \tag{5.5}$$

Here, m_{ij} denotes a measurement[6] and f is the function that describes the measured data and depends on local track parameters $\boldsymbol{q}_j$ and the global parameters $\boldsymbol{p}$. See Figure 5.3 for a depiction of the relevant variables introduced here. By summing over all hits in a track and over all tracks in a dataset, the χ^2 function

$$\chi^2(\boldsymbol{q}_j, \boldsymbol{p}) = \sum_{j}^{\texttt{tracks}} \sum_{i}^{\texttt{hits}} \left(\frac{r_{ij}}{\sigma_{ij}} \right)^2 \tag{5.6}$$

can be defined, where σ_{ij} denotes the uncertainty of the measurement. Minimising this function will lead to an optimal combination of track parameters and global parameters.

The MILLEPEDE-II algorithm [45] is a global method which solves the minimisation problem in a single step and is used for the track based alignment for the *Mu3e* detector. It was originally developed in the H1 experiment [46, 47] and has since been successfully applied to a variety of tracking systems like CMS at LHC [44, 48–56] and Belle 2 at SuperKEKB [57].

5.3 The Millepede-II Programme

In section B.1 it is demonstrated that the minimisation of Equation 5.6 comes down to the matrix equation

$$\boldsymbol{C}\Delta\boldsymbol{a} = \boldsymbol{b} \tag{5.7}$$

which, in turn, can be solved via the inversion of matrix $\boldsymbol{C}$. The parameter vector $\Delta\boldsymbol{a} = (\Delta\boldsymbol{p}, \Delta\boldsymbol{q}_j)$ incorporates changes in the local and global parameters. However, working with millions of tracks and $\mathcal{O}(10^5)$ global parameters leads to a very large matrix. Assuming N local measurements, of which each depends on ν track parameters and a global parameters, the size of C becomes $(a + N \cdot \nu) \times (a + N \cdot \nu)$. For one alignment run of the *Mu3e* experiment, the following values are expected: $N \approx 2 \cdot 10^6$, $\nu \approx 25$ and $a \approx 5 \cdot 10^5$. Hence, the matrix will have a size of roughly $5 \cdot 10^7$, making a straightforward inversion of this matrix in a reasonable time impossible, since the computing time for inversion grows with $(a + N \cdot \nu)^3$. Here MILLEPEDE-II comes into play, exploiting the sparsity of $\boldsymbol{C}$ and thereby reducing computing time.

[6] Since pixel sensors measure hits in two dimensions, a measured hit would consist of two measurements.

5.3.1 The Formalism of Millepede-II

The matrix $\boldsymbol{C}$ in Equation 5.7 can be divided into submatrices with specific features: The upper left block, $\boldsymbol{C}_1$, a symmetric matrix, is calculated from the global derivatives $\partial f/\partial \boldsymbol{p}$ only and is therefore of dimension a. The other sub-matrices are either zero or single-track related. By defining the matrices $\boldsymbol{\Gamma}_j$, consisting of the j-th local measurement and the local derivatives $\partial f/\partial \boldsymbol{q}_j$, and $\boldsymbol{G}_j$, consisting of mixtures between the local and global derivatives, Equation 5.7 can now be expressed as

$$\left(\begin{array}{c|c|c|c} \boldsymbol{C}_1 & \cdots & \boldsymbol{G}_j & \cdots \\ \hline \vdots & \ddots & 0 & 0 \\ \hline \boldsymbol{G}_j^T & 0 & \boldsymbol{\Gamma}_j & 0 \\ \hline \vdots & 0 & 0 & \ddots \end{array}\right) \cdot \left(\begin{array}{c} \Delta\boldsymbol{p} \\ \hline \vdots \\ \hline \Delta\boldsymbol{q}_j \\ \hline \vdots \end{array}\right) = \left(\begin{array}{c} \boldsymbol{b}^{\texttt{global}} \\ \hline \vdots \\ \hline \boldsymbol{b}_j^{\texttt{local}} \\ \hline \vdots \end{array}\right) \tag{5.8}$$

with the (global) alignment parameter corrections[7] $\Delta\boldsymbol{p}$ and the (local) track parameter corrections $\Delta\boldsymbol{q}$. Additionally, the right-hand-side vector $\boldsymbol{b}$ has been divided into the two sub-vectors $\boldsymbol{b}^{\texttt{global}}$, consisting of products of global derivatives and the normalised residuals, and $\boldsymbol{b}^{\texttt{local}_j}$, consisting of products of local derivatives and the normalised residuals.

In Appendix C it is shown that such an equation can be solved for $\Delta\boldsymbol{p}$ by solving the equation of reduced size

$$\boldsymbol{C}'\Delta\boldsymbol{p} = \boldsymbol{b}', \tag{5.9}$$

where

$$\boldsymbol{C}' = \boldsymbol{C}_1 - \sum_j \boldsymbol{G}_j \boldsymbol{\Gamma}_j^{-1} \boldsymbol{G}_j^T \tag{5.10}$$

and

$$\boldsymbol{b}' = \boldsymbol{b}^{\texttt{global}} - \sum_j \boldsymbol{G}_j \boldsymbol{\Gamma}_j^{-1} \boldsymbol{b}_j^{\texttt{local}}. \tag{5.11}$$

The χ^2 function in Equation 5.6 can now be minimised by solving the matrix equation of size a in Equation 5.9 instead of the far larger equation of size $a + Nv$ in Equation 5.7. This represents the core idea of the Millepede algorithm.

5.3.2 Hierarchical Alignment in Millepede-II

As mentioned in chapter 2 and shown in Figure 2.10, the *Mu3e* detector will be built in a hierarchical structure. This has several advantages with regards to track based

[7] Alignment parameters describe the geometry of detector parts.

alignment with MILLEPEDE-II: The determination of alignment corrections for composite detector parts requires far less statistics to reach good results than determining corrections for the individual parts it consists of[8]. Moreover, as stated in section 4.1, the hierarchy is expected to be reflected in the detector geometry after construction and applying the same structural coherences to the alignment algorithm is standing to reason. But this procedure is not only beneficial right after construction. Changes in temperature, the magnetic field, hall access and other influences can lead to deformations and misplacements of the tracker structure. Not implementing a hierarchical alignment, but instead only aligning individual pixel sensors, would not be feasible in this context and would probably not lead to an adequate result.

In MILLEPEDE-II, hierarchical alignment is realised by introducing linear constraints of the form

$$\boldsymbol{A}\boldsymbol{p} = \boldsymbol{c} \tag{5.12}$$

to the χ^2 minimisation and performing the minimisation with the method of Lagrange multipliers. The method of Lagrange multipliers is a strategy of finding extrema of a function subject to equality constraints. It is used in MILLEPEDE-II to minimise the χ^2 function (Equation 5.6) with subject to linear constraints (Equation 5.12) by introducing an additional parameter λ_i for each single constraint. In section B.2 it is shown that this leads to a new system of equations which can be expressed as the matrix equation

$$\left(\begin{array}{c|c} \boldsymbol{C} & \boldsymbol{A}^T \\ \hline \boldsymbol{A} & 0 \end{array}\right) \cdot \begin{pmatrix} \Delta\boldsymbol{a} \\ \boldsymbol{\lambda} \end{pmatrix} = \begin{pmatrix} \boldsymbol{b}_1 \\ \hline \boldsymbol{c} - \boldsymbol{A}\boldsymbol{a}_{0j} \end{pmatrix}. \tag{5.13}$$

Since the composed matrix in Equation 5.13 is still relatively small, it can be solved efficiently with adequate[9] methods.

5.3.3 Outlier Treatment

In a χ^2 minimisation, the normalised residuals r_{ij}^2/σ_{ij} influence the overall fit, distorting the result of the least squares fit. Measured hits which are multiple standard deviations off from their predicted position will have a large impact on the result. These so called *outliers* can be rejected or reweighted by MILLEPEDE-II which consequently requires internal iterations of the least squares fit.

Track Rejection For the local fit in MILLEPEDE-II (Equation 5.9), the value of χ^2 and the number of degrees of freedom (ndf) are calculated for each track and a cut can be applied on χ^2/ndf to reject badly reconstructed tracks. For the first iteration, a fairly soft cut should be applied to not reject tracks that have a large χ^2/ndf due to poorly aligned sensors. The cut will be reduced with each refit, since improvements

[8] This is due to the fact that the precision of the alignment result scales with the number of tracks used for the detector part to be aligned. Composite detector parts can use all the tracks measured with the included individual parts and have thereby enlarged statistics.

[9] Which method to use varies with the size and the specific demands.

in the alignment will also reduce the χ^2 of each track fit. MILLEPEDE-II allows the definition of the first two cuts; subsequent cuts are calculated by dividing the previous one by $\sqrt{2}$ until the minimum cut of 1 is reached. However, there might still be outliers due to a wrong reconstruction. These will still be rejected since their χ^2 will not improve sufficiently with better alignment.

Hit Reweighting For a reweighting of outlier hits, the *method of M-estimates* is used to modify the measurement weight $1/\sigma_{ij}$ of an outlier. For that, a probability density function has to be defined to replace the standard χ^2 function.

5.4 The Alignment Work flow of the Mu3e Experiment

At the heart of the pixel tracker alignment for *Mu3e* lies MU3EPIXAL which was created in the context of this thesis. It uses the tracking library WATSON, which was created for *Mu3e* in [30] and some added extensions that were created by the author in the context of this thesis. For the alignment to work, hit information in the form of local hit coordinates and the geometries of the sensors the hits were registered with, are required. Moreover, an initial estimate for the track parameters of each track are needed. They are obtained in form of a "track seed"[10] from *Mu3e*'s track fitting algorithm (see subsection 2.4.2). Once this is read in, MU3EPIXAL refits tracks using GBL to obtain all propagation Jacobians[11]. From there, the local derivatives, i.e. derivatives of the measurements with respect to the track parameters, and global derivatives, i.e. derivatives with respect to the parameters, are calculated.

These parameters are stored in a binary file to be read by PEDE, a standalone programme that performs the least squares fit in Equation 5.9. Additionally, PEDE needs a steering file which (among other options) contains information about which parameters (see section 5.5) to align for and optionally a constraint file that contains information about e.g. the hierarchy structure, a localisation of the global detector movement or any other constraint that can be expressed like Equation 5.12. In the resulting *millepede.res* file, the corrections to the alignment parameters that were calculated by PEDE are stored. The last step is then to read the results, interpret them and use the outcome to update the geometry information.

MILLEPEDE-II offers the possibility to make use of external measurements and include them into the least squares fit. Since *Mu3e* is still under development, the options of external measurements have not yet been investigated thoroughly. It is clear however that some sort of measurement for the positions of the endrings where the

[10] Track seed in this context includes estimated values for initial track position, direction and momentum.

[11] Propagation Jacobians are derivatives of the track parameters at one sensor with respect to the ones at the previous one. Hence, they give information about how changes in track parameters at one sensor affect the parameters at the next one the track passes through.

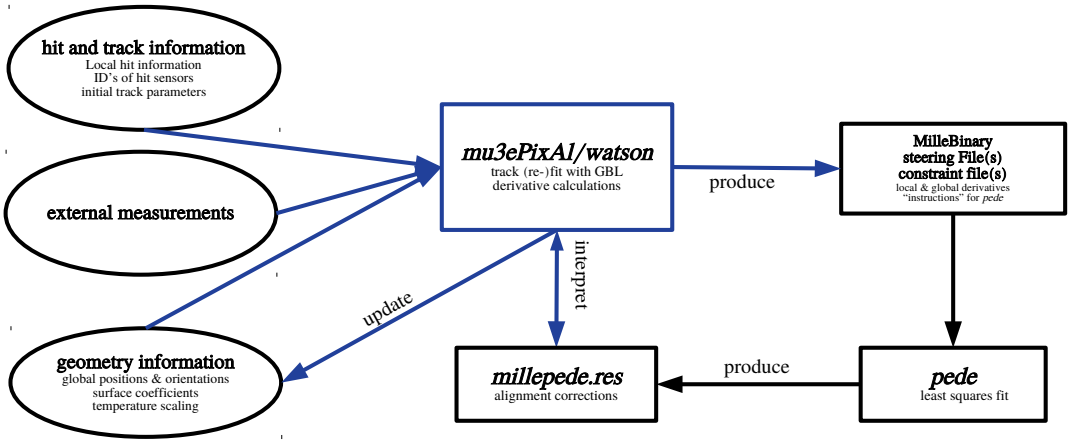

FIGURE 5.4: Alignment work flow; marked in blue are the parts that were created in the context of this thesis.

pixel ladders will be mounted on (Figure 2.14) has to be implemented. In the software framework, this has been carried out by the addition of "fake" measurements which are read into MU3EPIXAL.

The above described work flow is summarised in Figure 5.4.

5.5 Alignment Parametrisation

To describe the detector geometry, a representation of a single sensor geometry has to be defined. Assuming the sensors to be rigid bodies, this can be achieved by defining a reference point $\boldsymbol{x}_0$ and a rotation matrix $\boldsymbol{R}$. Such a rotation matrix defines coordinate transformations between the global right-handed $(\widehat{\mathbf{x}}, \widehat{\mathbf{y}}, \widehat{\mathbf{z}})$-system and a local $(\widehat{\mathbf{u}}, \widehat{\mathbf{v}}, \widehat{\mathbf{w}})$-system as depicted in Figure 5.5. Transformations from a local into the global coordinate system can therefore be defined as

$$\boldsymbol{x} = \boldsymbol{R}\,\boldsymbol{q} + \boldsymbol{x}_0. \tag{5.14}$$

Here, $\boldsymbol{q} = (u, v, w)^T$ describes a local point on a sensor with reference point $\boldsymbol{x}_0$ that is transformed into the global point $\boldsymbol{x} = (x, y, z)^T$.

For composite detector parts, the reference points are the centre of mass of the active surfaces of all included sensors. Their coordinate system is the global system, where x and y are perpendicular and z is parallel to the beam, is used.

In the following, the *alignment parameters*, i.e. parameters used to describe corrections to the detector geometry, are introduced and the according alignment Jacobians are derived.

5.5.1 Rigid Body Parameters

Assuming the detector parts to be aligned to be rigid bodies, the basic alignment parameters for these entities are offsets and rotations relative to their nominal position

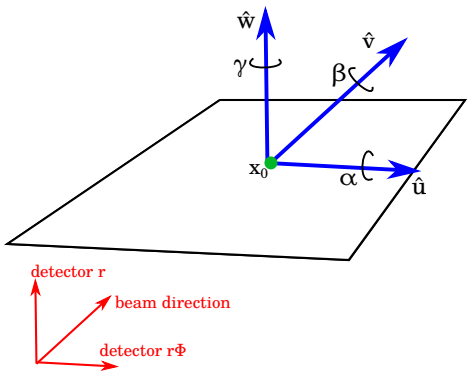

FIGURE 5.5: The unit vectors $\hat{\mathbf{u}}$, $\hat{\mathbf{v}}$, and $\hat{\mathbf{w}}$ define a right-handed local coordinate system for individual sensors. $\hat{\mathbf{u}}$ and $\hat{\mathbf{v}}$ are parallel to the sensor edges and span the nominal plane in which the sensor lies. The green dot, marked with a x_0, labels the centre and represents a reference point. The red coordinate system is a reference to the global coordinates. Hence, $\hat{\mathbf{u}}$ points in $r\Phi$-direction, $\hat{\mathbf{w}}$ points in radial-direction (away from the centre) of the barrel and $\hat{\mathbf{v}}$ in beam direction.

and orientation.

Offsets Offset corrections $\Delta\boldsymbol{q} = (\Delta u, \Delta v, \Delta w)^\top$ are given in the local coordinate system and correspond to changes in the respective axis direction with respect to the nominal position.

Rotations Corrections to the orientation are defined by the "small" angles α, β and γ and can be expressed in the form of three rotation matrices for rotations around the respective axes:

$$\Delta\boldsymbol{R}_\alpha = \begin{pmatrix} 1 & 0 & 0 \\ 0 & \cos\alpha & \sin\alpha \\ 0 & -\sin\alpha & \cos\alpha \end{pmatrix} \tag{5.15}$$

$$\Delta\boldsymbol{R}_\beta = \begin{pmatrix} \cos\beta & 0 & -\sin\beta \\ 0 & 1 & 0 \\ \sin\beta & 0 & \cos\beta \end{pmatrix} \tag{5.16}$$

$$\Delta\boldsymbol{R}_\gamma = \begin{pmatrix} \cos\gamma & \sin\gamma & 0 \\ -\sin\gamma & \cos\gamma & 0 \\ 0 & 0 & 1 \end{pmatrix} \tag{5.17}$$

By combining these matrices, one can derive the following overall rotation matrix for rotations around all three axes in a given order:

$$\begin{aligned}\Delta\boldsymbol{R} &= \Delta\boldsymbol{R}_\gamma \cdot \Delta\boldsymbol{R}_\beta \cdot \Delta\boldsymbol{R}_\alpha \\ &= \begin{pmatrix} \cos\beta\cos\gamma & \cos\alpha\sin\gamma + \sin\alpha\sin\beta\cos\gamma & \sin\alpha\sin\gamma - \cos\alpha\sin\beta\cos\gamma \\ -\cos\beta\sin\gamma & \cos\alpha\cos\gamma - \sin\alpha\sin\beta\sin\gamma & \sin\alpha\cos\gamma + \cos\alpha\sin\beta\sin\gamma \\ \sin\beta & -\sin\alpha\cos\beta & \cos\alpha\cos\beta \end{pmatrix}\end{aligned} \tag{5.18}$$

The corrected global position of a rigid body can therefore be determined as

$$\boldsymbol{x}_{\texttt{corr}} = \boldsymbol{R}\,\Delta\boldsymbol{R}\,(\boldsymbol{q} + \Delta\boldsymbol{q}) + \boldsymbol{x}_0. \tag{5.19}$$

5.5.2 Surface Parameters

Since the MuPix chip used for *Mu3e* will have a thickness of about 50 µm, rigid body alignment parameters as discussed above alone will not be sufficient to describe their geometry entirely. Additional deviations from the nominal planar surface have to be considered. A height map describing the distance along the $\widehat{\mathbf{w}}$-axis from the nominal sensor plane as a function of the two-dimensional position in the plane, is defined. The plane coordinates (u, v) are left unchanged and are taken to be identical to the corresponding local coordinates in the nominal surface. This assumption is valid if the deformations are small compared to the scale of the plane coordinates, which they are expected to be.

To be able to adjust the surfaces optimally, the height map is expanded in Legendre polynomials $P_n(x)$ up to third order[12]. The Legendre polynomial of order n of a single variable x can be expressed as

$$P_n(x) = 2^n \sum_{k=0}^{n} \binom{n}{k} \binom{\frac{n+k-1}{2}}{n} x^k. \tag{5.20}$$

Legendre polynomials are defined in the interval $x \in [-1, 1]$. Hence, the local coordinates (u, v) must be normalized to this range before calculating the polynomials. The two-dimensional height map is defined as

$$h(x, y) = \sum_{i=0}^{N} \sum_{j=0}^{i} c_{ij}\, P_{i-j}(x)\, P_j(y), \tag{5.21}$$

where x and y are the normalized input coordinates and c_{ij} is the weighting coefficient for each term. Since the polynomials are dimensionless, all coefficients must have dimension length by construction. It must be noted that the constant and linear terms of the height map are conceptually identical to offsets and rotations and can therefore be absorbed by the corresponding parameters defined in subsection 5.5.1.

[12] An expansion to higher order is prepared in software and can easily be activated, but is not expected to be necessary.

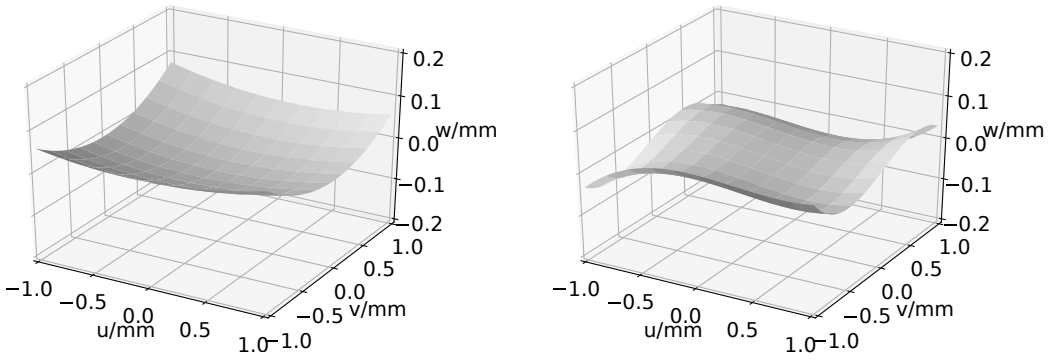

FIGURE 5.6: Example configurations of sensor surfaces parametrised by the height map in Equation 5.21. On the left, Legendre polynomials of up to second order are used, on the right, up to third order. Surface coefficients are of the size of how they are expected after detector construction.

Hence, only quadratic and higher order terms need to be considered for the height map. This means, a matrix that combines all relevant surface parameters can be defined as

$$\boldsymbol{C} = \begin{pmatrix} 0 & 0 & 0 & 0 \\ 0 & 0 & 0 & 0 \\ c_{20} & c_{21} & c_{22} & 0 \\ c_{30} & c_{31} & c_{32} & c_{33} \end{pmatrix} \tag{5.22}$$

and used for the height map in Equation 5.21.

Normalising the input coordinates means scaling them by the sensor dimensions, i.e. $x = 2u/l_u$ and $y = 2v/l_v$, where l_u and l_v are the sensor lengths in local u- and v-direction respectively. Example configurations of the sensor surfaces can be found in Figure 5.6.

By defining a three-dimensional height function as

$$\boldsymbol{h}(\boldsymbol{q}) = \begin{pmatrix} 0 \\ 0 \\ h(2u/l_u,\, 2v/l_v) \end{pmatrix}, \tag{5.23}$$

the addition of surface deformations, parametrised as above, to local coordinates causes the following transformation:

$$\boldsymbol{q} \to \boldsymbol{q} + \boldsymbol{h}(\boldsymbol{q}). \tag{5.24}$$

5.5.3 Temperature Effects

Temperature changes affect the size of the detector. On the sensor level, this means that the sensor dimensions will change, introducing one scaling factor d_i for each dimension. This means that the scaling parameters defined previously for the surface

deformations must be adapted to

$$l_i \to d_i \, l_i, \quad i = u, v. \tag{5.25}$$

To simplify these transformations, the vector function

$$\boldsymbol{d}(\boldsymbol{q}) = (d_u u, \, d_v v, \, w)^T = \boldsymbol{q'} \tag{5.26}$$

can be defined.

5.5.4 Combined Parametrisation

For a consistent description, the different alignment effects need to be considered at once. Hence, with the addition of surface deformation (Equation 5.24) and temperature scaling effects (Equation 5.26), Equation 5.19 has to be adjusted. The final transformation that considers all previously described effects then reads

$$\boldsymbol{x}_{\texttt{corr}} = \boldsymbol{R} \, \Delta\boldsymbol{R} \left(\boldsymbol{q'} + \boldsymbol{h}(\boldsymbol{q'}) + \Delta\boldsymbol{q} \right) + \boldsymbol{x}_0. \tag{5.27}$$

5.6 Alignment Jacobians

Alignment Jacobians are matrices that include derivatives of the measurements $\boldsymbol{m} = (u, \, v)$ with respect to the alignment parameters

$$\boldsymbol{\Delta p} = (\Delta u, \, \Delta v, \, \Delta w, \, \alpha, \, \beta, \, \gamma, \, \boldsymbol{c})^T. \tag{5.28}$$

For reasons of simplicity, the surface parameters in Equation 5.22 are here expressed as the vector

$$\boldsymbol{c} = (c_{20}, \, c_{21}, \, c_{22}, \, c_{30}, \, c_{31}, \, c_{32}, \, c_{33}). \tag{5.29}$$

Since the temperature scaling is not yet fully implemented in MU3EPIXAL, the related parameters d_u and d_v are excluded here.

5.6.1 Rigid Body Jacobian

For rigid bodies, the alignment parameters are

$$\boldsymbol{\Delta p}_{\texttt{rigid}} = (\Delta u, \, \Delta v, \, \Delta w, \, \alpha, \, \beta, \, \gamma)^T \tag{5.30}$$

and the corresponding Jacobian can be expressed as

$$\frac{\partial \boldsymbol{m}}{\partial \boldsymbol{\Delta p}_{\texttt{rigid}}} = \begin{pmatrix} -1 & 0 & u' & u'v & -u'u & v \\ 0 & -1 & v' & v'v & -v'u & -u \end{pmatrix} \tag{5.31}$$

with the local slopes

$$u' = t_u/t_w \qquad v' = t_v/t_w \tag{5.32}$$

and the local tangent of the incoming track $\boldsymbol{t} = (t_u,\ t_v,\ t_w)^T$. The derivation of Equation 5.31 can be found in section D.1.

For reasons of numerical stability, it is advantageous to have matrix elements of similar sizes and same units. Therefore, the rotations around the α- and β-axes have been replaced by tilts around the respective axes and the rotation around the γ-axis was scaled by the scaling factor

$$c_l = \frac{l_u + l_v}{2}. \tag{5.33}$$

With the normalised local coordinates $x = 2u/l_u$ and $y = 2v/l_v$, Equation 5.31 translates to

$$\frac{\partial \boldsymbol{m}}{\partial \boldsymbol{\Delta p}_{\mathtt{rigid}}} = \begin{pmatrix} -1 & 0 & u' & u'x & u'y & v/c_l \\ 0 & -1 & v' & v'x & v'y & -u/c_{l.} \end{pmatrix}. \tag{5.34}$$

Note that in this convention, rotations around α correspond to tilts in v-direction and rotations around β to tilts in u-direction. The signs of the rotation- and tilt-derivatives (last three columns in Equation 5.34) merely represent the chosen convention of rotation- and tilt-direction and are to some degree arbitrary. However, they have to be consistent throughout the whole alignment implementation.

5.6.2 Surface Jacobian

The alignment parameters describing surface deformations are

$$\boldsymbol{\Delta p}_{\mathtt{surface}} = (\boldsymbol{c})^T \tag{5.35}$$

and according to section D.2, the corresponding Jacobian can be expressed as

$$\frac{\partial \boldsymbol{m}}{\partial \boldsymbol{\Delta p}_{\mathtt{surface}}} = \begin{pmatrix} u'P_2(x)P_0(y) & v'P_2(x)P_0(y) \\ u'P_1(x)P_1(y) & v'P_1(x)P_1(y) \\ u'P_0(x)P_2(y) & v'P_0(x)P_2(y) \\ u'P_3(x)P_0(y) & v'P_3(x)P_0(y) \\ u'P_2(x)P_1(y) & v'P_2(x)P_1(y) \\ u'P_1(x)P_2(y) & v'P_1(x)P_2(y) \\ u'P_0(x)P_3(y) & v'P_0(x)P_3(y) \end{pmatrix}^T, \tag{5.36}$$

with the Legendre polynomials P_n, u' and v' defined as in subsection 5.6.1 and x and y as the normalised local parameters $x = 2u/l_u$ and $y = 2v/l_v$.

5.6.3 Overall Alignment Jacobian

Combining Equations 5.34 and 5.36 yields the overall alignment Jacobian which includes derivatives of measurements with respect to all 13 single sensor alignment parameters currently used by MU3EPIXAL:

$$\boldsymbol{J} = \left(\frac{\partial \boldsymbol{m}}{\partial \boldsymbol{\Delta p}_{\mathtt{rigid}}} \qquad \frac{\partial \boldsymbol{m}}{\partial \boldsymbol{\Delta p}_{\mathtt{surface}}}\right) = \begin{pmatrix} -1 & 0 \\ 0 & -1 \\ u' & v' \\ u'x & v'x \\ u'y & v'y \\ v/c_l & -u/c_l \\ u'P_2(x)P_0(y) & v'P_2(x)P_0(y) \\ u'P_1(x)P_1(y) & v'P_1(x)P_1(y) \\ u'P_0(x)P_2(y) & v'P_0(x)P_2(y) \\ u'P_3(x)P_0(y) & v'P_3(x)P_0(y) \\ u'P_2(x)P_1(y) & v'P_2(x)P_1(y) \\ u'P_1(x)P_2(y) & v'P_1(x)P_2(y) \\ u'P_0(x)P_3(y) & v'P_0(x)P_3(y) \end{pmatrix}^T \tag{5.37}$$

5.7 Hierarchy Structure

In Figure 2.10, the hierachical structure of the *Mu3e* detector is depicted. According to this, there are several composite parts consisting of smaller subcomponents. These subcomponents go all the way down to individual sensors. In chapter 4 it was discussed how larger entities can be misplaced as a whole - this should be reflected in the alignment as well.

Since measurements are only possible as local ones on individual pixel sensors, a transformation has to be found to transform the alignment results from the subcomponent "sensor" to the composite parts that are ladders, modules and layers. Such a transformation can be expressed as

$$\Delta \boldsymbol{p}_{\mathtt{s}} = \boldsymbol{C}\, \Delta \boldsymbol{p}_{\mathtt{c}}. \tag{5.38}$$

Since for now, only rigid body parameters are considered for composite parts[13], the symmetric transformation matrix $\boldsymbol{C}$ transforms composite rigid body alignment parameters[14] $\Delta \boldsymbol{p}_{\mathtt{c}}$ into subcomponent parameters $\Delta \boldsymbol{p}_{\mathtt{s}}$[15]. The calculation of $\boldsymbol{C}$ can be found in Appendix E.

[13] This should and will change in future implementations of MU3EPIXAL.

[14] Rigid body parameters consist of the positional and rotational alignment parameters: $\Delta \boldsymbol{p} = (\Delta u, \Delta v, \Delta w,\ \alpha, \beta, \gamma)$

[15] $\boldsymbol{C}^{-1}$ accordingly transforms subcomponent parameters to composite parameters.

The desired derivatives of a measurement $\boldsymbol{m}$ with respect to the composite alignment parameters can be calculated via the chain rule:

$$\frac{\partial \boldsymbol{m}}{\partial \boldsymbol{p}_c} = \frac{\partial \boldsymbol{r}}{\partial \boldsymbol{p}_s}\frac{\partial \boldsymbol{p}_s}{\partial \boldsymbol{p}_c} \tag{5.39}$$

$$= \frac{\partial \boldsymbol{r}}{\partial \boldsymbol{p}_s}\boldsymbol{C}. \tag{5.40}$$

5.8 Weak Modes

Weak modes in track based alignment are tracker deformation modes that don't influence the χ^2 in Equation 5.6. An obvious weak mode is the overall movement of the complete detector in space. The principle of a weak mode is depicted in Figure 5.7 for the example of an elliptical deformation of the tracker barrel. If the barrel is deformed elliptically, the true track will have a worse χ^2 than without the deformation. However - and that is what makes up a weak mode - another track can be reconstructed with the same χ^2 as the original one.

In Figure 5.8, an overview of various other misalignment modes that are expected to represent alignment weak modes for the *Mu3e* detector, are presented. This is neither a complete list nor is it guaranteed that all of them will appear in the *Mu3e* detector, it is rather a first estimate of what is expected and what has already been observed in simulation.

Weak modes for the *Mu3e* detector can be suppressed by utilising tracks from cosmic muons, since they have a very different topology than the expected tracks coming from muon decays in the target (see Figure 5.9). Because of their strong forward momentum, it is also planned to add reconstructed tracks from Mott scattering to the overall pool of data used for alignment. They have the advantage of connecting detector parts with trajectories that are not connected by only utilising low momentum particles coming from the muon decay at rest. However, this is not

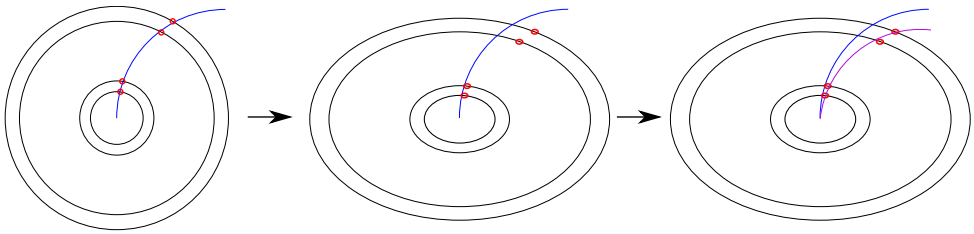

FIGURE 5.7: Schematic depiction of an elliptical deformation of the tracker barrel. Elliptical deformations do not affect the χ^2-function of the track fit. In blue, the true track is depicted. The red circles are measured hits. If the barrel is deformed elliptically, the blue track will have a worse χ^2 than without the deformation. However - and that is what makes up a weak mode - another track (purple) can be reconstructed with the same χ^2 as the original blue one.

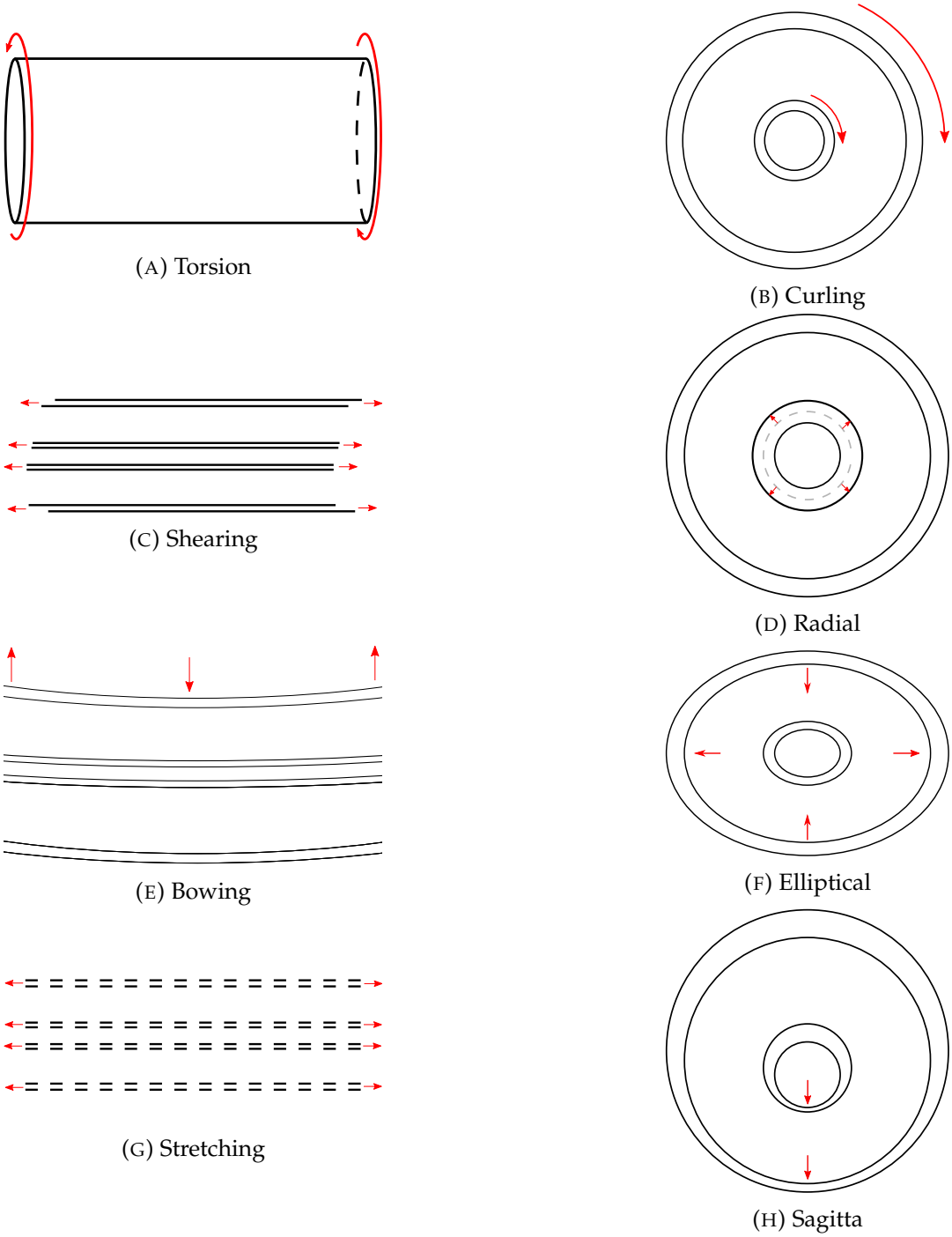

(A) Torsion

(B) Curling

(C) Shearing

(D) Radial

(E) Bowing

(F) Elliptical

(G) Stretching

(H) Sagitta

FIGURE 5.8: Schematic depiction of expected possible weak modes for the *Mu3e* detector. Left side figures are in rz-view and right side figures in xy-view of the detector.

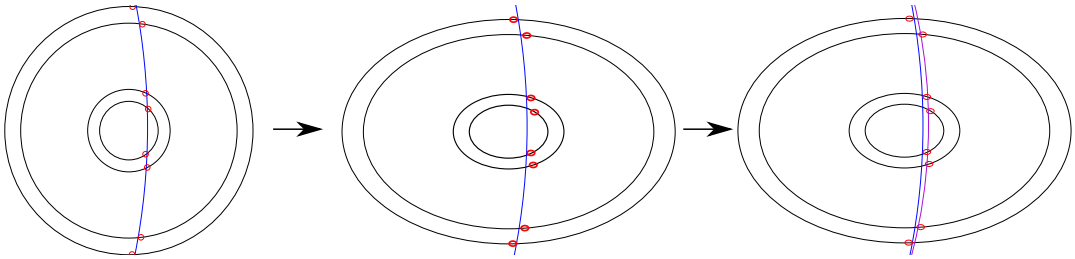

FIGURE 5.9: Cosmic muon passing the tracker barrel. Elliptical deformations do affect the χ^2-function of the track fit.

fully implemented into the software framework and is therefore not part of the results presented in section 6.2. In general, having as many "different kinds" of tracks as possible will suppress weak modes, since the alignment will thereby not be prone to one specific track topology and the misalignment modes its χ^2-function is invariant onto.

Furthermore, survey measurements are planned to get independent position measurements of e.g. the barrel layer endrings. These measurements can be added easily to MU3EPIXAL and included into the χ^2 function in MILLEPEDE-II.

Chapter 6

Results

In this chapter, results for various applications of the alignment software package MU3EPIXAL will be presented. Starting off with a *proof of principle* for the programme to work with real data: the application onto beam telescopes. Afterwards, the application of the alignment on the simulated *Mu3e* detector and a strategy to handle a possible real life misalignment scenario in the future, is introduced. Eventually, results for the track based alignment of the *Mu3e* pixel detector will be presented and discussed.

6.1 Results for Beam Telescopes

The MUPIX prototypes have been tested with regards to performance and characteristics extensively both in the lab and in test beam campaigns. For the latest prototype, the MUPIX8, measurements are ongoing since 2017. A customary way to study sensor properties is to utilise a so called "beam telescope", i.e. an arrangement of several sensors in a row, such that a passing particle will be detected by all of them. Figure 6.1 shows examples of beam telescopes used by the *Mu3e* collaboration. The "device-under-test" (DUT), i.e. the sensor to be investigated, will be sandwiched in between the telescope layers. All sensor layers but the DUT are used to fit a particle trajectory and extrapolate the track position onto the DUT, allowing for various studies to take place. In addition to the MUPIX telescope, consisting solely of MUPIX sensors, EUDET [58] type beam telescopes, stationed at "Deutsches Elektronen-Synchrotron" (DESY) in Hamburg, were utilised.

This provides a great opportunity to test the *Mu3e* alignment tools (see section 5.4) in real life to provide a "proof of principle". Hence, the alignment for the telescopes used by the *Mu3e* collaboration for characterising MUPIX prototypes, is performed with exactly these tools. Since the *Mu3e* testbeam campaign did not contain measurements from a beam telescope inside a magnetic field, different demands are put on the tracking and alignment algorithms than for the *Mu3e* detector. However, this has the advantage of being able to test if said algorithms also work for a turned off magnet and for cosmic rays, which are - because of their high momentum - not expected to be largely affected by the field.

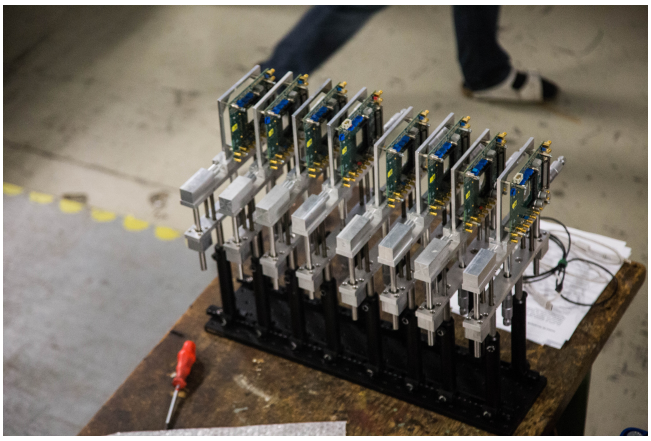

(A) MUPIX8 telescope

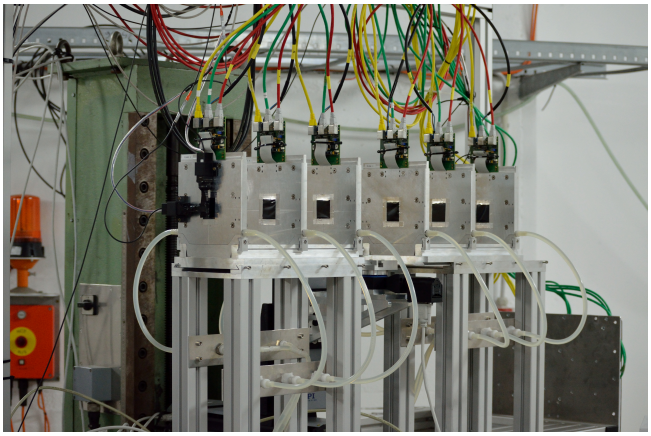

(B) EUDET-type telescope DURANTA

(C) MUPIX8 prototype as DUT in DURANTA telescope

FIGURE 6.1: Photographs (courtesy of Niklaus Berger) of different testbeam setups for the MUPIX prototype characterisation.

But this is not the only reason to implement the MU3EPIXAL framework for a telescope as well. For each sensor plane that is added to a telescope, the problem of alignment becomes more challenging. Especially, if the "usual" methods of histogram based alignment (see Figure 5.2) are applied. Considering *Mu3e* is using an eight-plane telescope since 2016 for test beams, it has been decided to carry out the alignment tasks for the test beam campaigns solely with the *Mu3e* alignment tools. By now, the tools were used to align telescopes that (among others) vary in chip size, total number of sensors used in the telescope, pixel size and detection efficiency.

In this section, alignment results for a MUPIX8 telescope and a EUDET telescope will be presented. The results are based on the calculation of residuals, i.e. the difference between fitted track position and measured hit on the sensor. A GBL track fit (see section 5.1) is used to gain fitted track positions and calculate the residuals. As input for the GBL, a straight line fit has been performed to obtain initial track parameters.

The data used for this section were provided through the courtesy of Lennart Huth [17].

6.1.1 Results for the MUPIX8 Telescope

The MUPIX8 sensors have 128 columns and 200 rows of $81 \times 80\,\mu m^2$ pixels (see section 3.3) and for the presented alignment results, eight of them were combined to a telescope.

The data used for the alignment results presented in the following was collected at DESY. About 1 million tracks from electrons with energies of $\mathcal{O}(1\,\text{GeV})$ were used to perform the track based alignment. The active alignment parameters, i.e. the parameters, MILLEPEDE-II was set up to align for, are shifts in the two-dimensional sensor planes and rotations around the axes perpendicular to the planes. Other parameters were not used, since they are only weakly constrained for a telescope set up like this. The presented results were obtained by iterating four times to minimise inaccuracies due to the linearisation performed in the alignment algorithm, where each iteration took about three minutes to process on a single CPU core. Figure 6.2 shows biased track residuals[1] of the MUPIX telescope before (red) and after (blue) the track based alignment software was used. Although the alignment has already been fairly good before, it was possible to improve it even further. The means of the residual distribution - as illustrated by the means of the Gaussian fits in Figure 6.2 - before the alignment are in the order of 10 µm. Afterwards they are smaller than 3 µm for all sensor planes[2] and even smaller than 2 µm for most of them which is a great result considering the pixel size.

The figure of merit of a telescope is its track resolution $\sigma_{t,i}$, i.e. the precision with which the intersection of a particle with a DUT can be determined. It depends on

[1] Biased residuals means, that the sensor for which the residual is calculated was also used in the track fit.

[2] Residuals for the remaining sensors can be found in section F.1.

the intrinsic resolution of the sensors $\sigma_{int,i}$; in the case of pixel sensors that relates to the pixel size. But it is also a function of the number of measurements, their position and the material in the path of the tracked particle. It worsens with a larger lever arm, since the deflection angle is boosted with larger distance to the previous measurement. In the limit of very large deflection angles, it converges towards the intrinsic resolution. The biased residual width (i.e. the standard deviation of the residual distribution) at a given sensor plane i can be calculated by

$$\sigma_r = \sqrt{\sigma_{int,i}^2 - \sigma_{t,i}^2}. \tag{6.1}$$

Figure 6.2 shows a larger residual width for the inner sensors plane than for the outer planes. This is expected, since the track resolutions at the outer planes are worse, making the difference between σ_{int} and σ_t smaller.

6.1.2 Results for an EUDET Type Telescope

The DURANTA telescope at DESY is composed of six MIMOSA26 sensors [58]. The MIMOSA26 is a monolithic active pixel sensor consisting of 576 by 1152 pixels with a pitch of 18.5 µm each. Hence, the DURANTA provides a very good intrinsic and thereby also track resolution, allowing for sub-pixel studies for the MUPIX chip. To do so, the DURANTA sensors have to be very well aligned.

About 130 000 tracks from electrons with energies of $\mathcal{O}(1\,\mathrm{GeV})$ were used to perform the track based alignment. The active alignment parameters are the same as the ones stated above for the MUPIX telescope, i.e. shifts in the two-dimensional sensor planes and rotations around the axes perpendicular to the planes. The presented results were obtained by iterating about ten times.

In Figure 6.3, the biased track residuals for three of the six aligned DURANTA planes are depicted. The whole set of residuals can be found in section F.1. The results are even better than for the MUPIX telescope which has to do with the smaller pixel size. The alignment software is able to align the DURANTA telescope to a degree that the residual means are of by a maximum of 1 µm on all planes and both local coordinates. The widths are smaller than 3 µm, where the widths of the inner planes are expectedly larger than the ones for the outer planes.

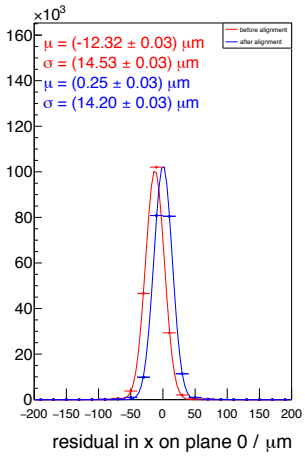

(A) Residual on first plane in local x-direction.

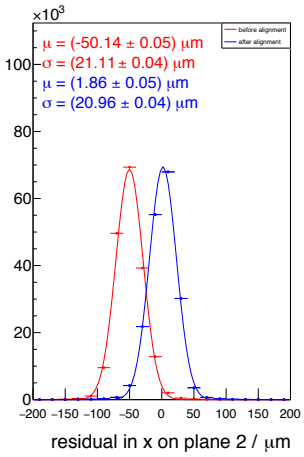

(B) Residual on third plane in local x-direction.

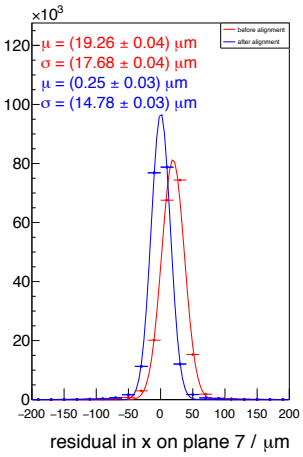

(C) Residual on last plane in local x-direction.

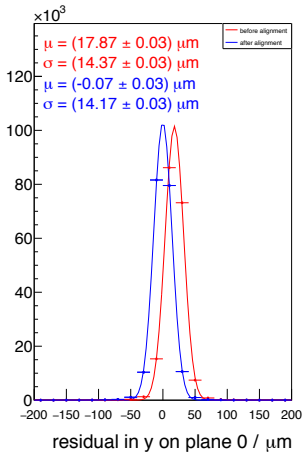

(D) Residual on first plane in local y-direction.

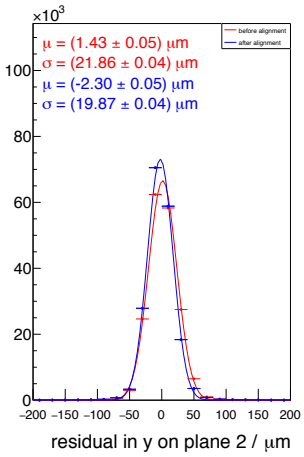

(E) Residual on third plane in local y-direction.

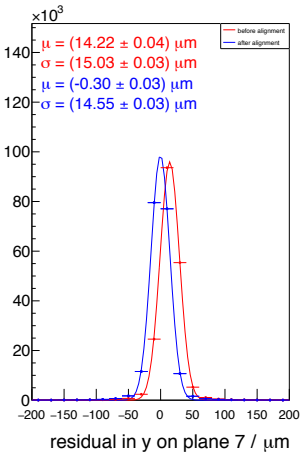

(F) Residual on last plane in local y-direction.

FIGURE 6.2: Track residuals on the first, last and (an arbitrary) inner sensor plane of an eight-plane MUPIX8 telescope. Depicted are the track residuals of a GBL track fitter. Residuals for the remaining sensors can be found in section F.1. The stated μ and σ are the mean and standard deviation of applied Gaussian fits.

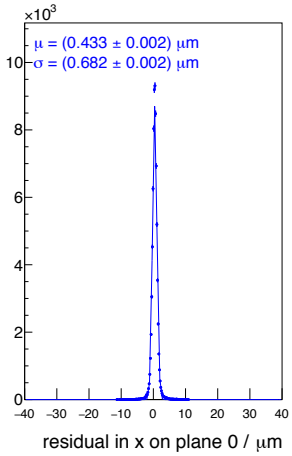

(A) Residual on first plane in local x-direction.

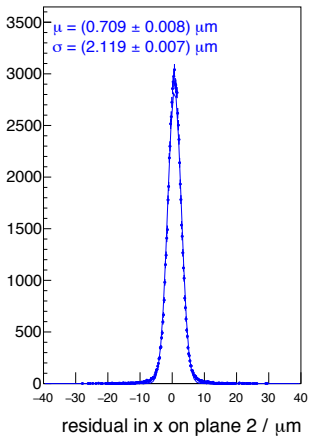

(B) Residual on third plane in local x-direction.

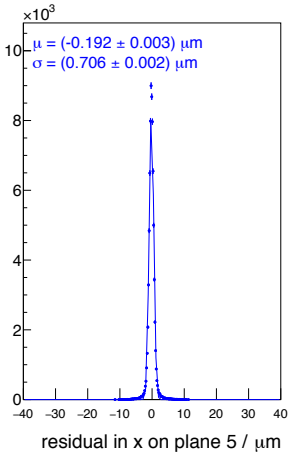

(C) Residual on last plane in local x-direction.

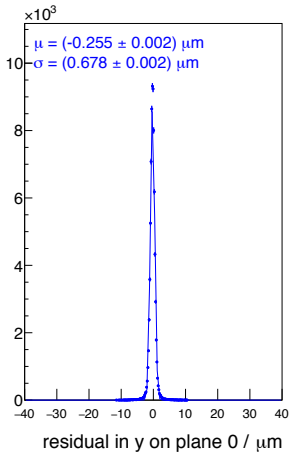

(D) Residual on first plane in local y-direction.

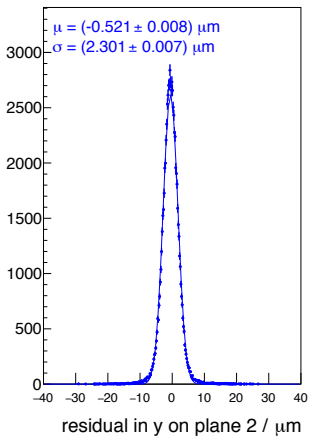

(E) Residual on third plane in local y-direction.

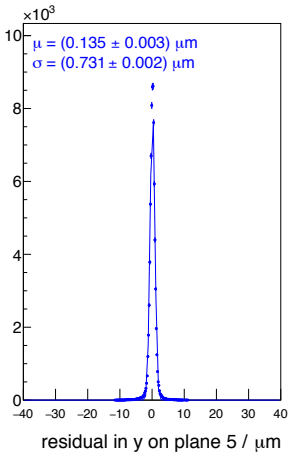

(F) Residual on last plane in local y-direction.

FIGURE 6.3: Track residuals on the first, last and an arbitrary inner sensor plane of an aligned DURANTA telescope. Residuals for the remaining sensors can be found in section F.1. The stated μ and σ are the mean and standard deviation of the Gaussian fit depicted in blue.

6.2 Results for the Mu3e Pixel Detector

The *Mu3e* tracking detector is a complex structure composed of almost 3000 pixel sensors assembled in a hierarchical configuration. This makes the alignment - especially right after detector construction - an extremely demanding task. In the following, the general ability of MU3EPIXAL to perform track based alignment for the *Mu3e* pixel detector is demonstrated for special case scenarios. Afterwards the development of an alignment strategy will be presented, followed by results[3] for a detector alignment based on the misalignment scenario right after detector assembly as introduced in section 4.1.

6.2.1 Special Case Alignment Scenarios

In section 6.1, the capability of MU3EPIXAL to align a very exceptional case of a detector - one without a magnetic field with all pixel sensors planes being roughly parallel to each other and perpendicular to the particle beam - was demonstrated. Subsequently, various studies to investigate the scalability of MU3EPIXAL to the complete *Mu3e* tracking detector (including sensor deformations) have been performed, of which some will be introduced here.

The following parameters have been chosen as indicators of the goodness of the alignment results in this context:

- absolute offset of individual sensors Δd
- $\Delta(r\phi)$.

The absolute offset is derived by calculating the absolute offsets of the four corners and centre for all sensors with respect to their true position. The offset in the product of radius r and azimuth angle ϕ of sensors is denoted as $\Delta(r\phi)$. To give an indicator of the precision of the result, a distribution width corresponding to the RMS will be given for both parameters.

Alignment at the Sensor Level

Standing to reason is that the alignment of individual sensors as rigid bodies and their surface deformations is a basic requirement of the alignment programme. To save computing time and data storage, the alignment scenarios presented in this context are reduced to only sensors that are part of the central detector station[4]; the results presented also relate solely to the sensors in the central station. A data sample of about 10 million track candidates, each from positive and negative muon decay and from cosmics was used for this study.

[3] For the results obtained in the context of this thesis, the assumption of a constant magnetic field was made. This is however not a perfectly valid assumption and tracking and alignment for the areas with a inhomogeneous magnetic field has to be tested and implemented.

[4] Since the alignment is implemented in the same way for each station, it is a valid assumption that the functionality of MU3EPIXAL translates through all stations.

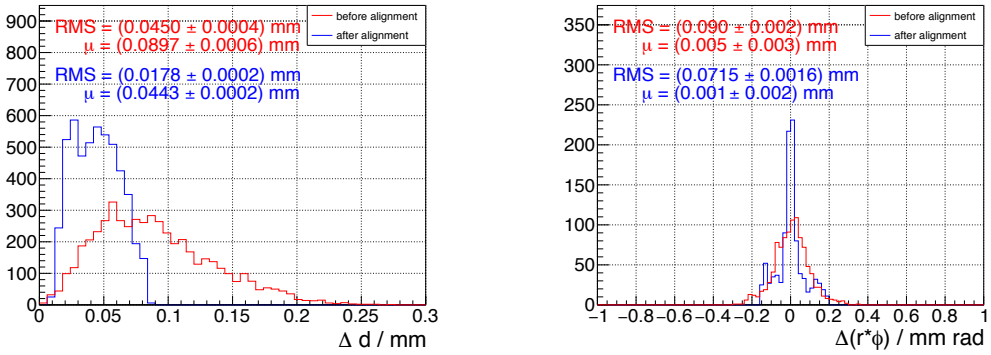

(A) Absolute offsets from the true sensor position.

(B) Deviation in $r\phi$ from the true sensor position.

FIGURE 6.4: Offsets before and after alignment of sensor positions and rotations in the central detector station.

For the alignment at sensor level, the misplacement chosen as initial input for the misalignment reflect the ones presented in Table 4.1. For the rigid body alignment, the sensors were therefore misaligned with offsets of up to 100 µm and rotations of up to 10 mrad. The applied surface deformations result in deviations from a flat surface of roughly half a pixel pitch in average.

Figure 6.4 shows the result for the mis- and re-alignment of rigid body parameters at sensor level for the central detector station. Five iterations[5] were performed, taking about three hours each to complete. It shows that the absolute offsets can be reduced by MU3EPIXAL to about half the pixel size, whereas $\Delta(r\phi)$ doesn't receive a large improvement, is however trending in the right direction. The leftover misalignment is connected to the weak mode of bowing of sensor layers which is displayed in Figure 6.5. This seems like a minor issue; however, it is something that needs to be studied in detail to suppress it in the future. Although the outcome could be improved, these results are already quite good and do certainly serve as a proof of principle.

To compare sensor deformations, the deviation from a flat surface Δh at the four sensor corners and the centre of a sensor are considered. This should give a feeling for the amount of deformation. In Figure 6.6, these deviations are displayed before and after two alignment iterations which took roughly three hours each to finish. It was possible to reduce the deviations by about a factor of five. Since the corrections obtained from PEDE in the second iteration are already at the level their corresponding errors, more iterations won't improve the results any further - but more data might do so.

[5]One iteration in this context corresponds to a reconstruction of all available tracks, the run of MU3EPIXAL and the correction of the tracker geometry according to the results obtained from MU3EPIXAL. The next iteration then uses the updated geometry to reconstruct tracks from the same data set again. See Figure 5.4.

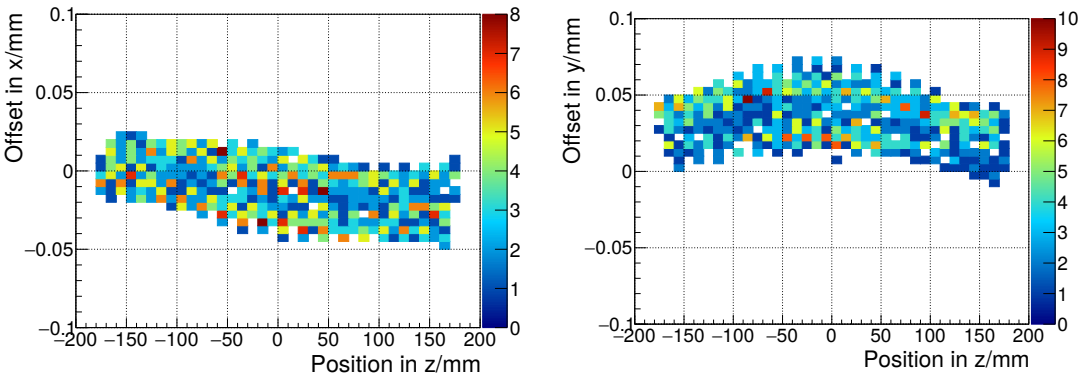

FIGURE 6.5: Sensor offsets in global x- and y-direction as a function of sensor position in global z after alignment of positions and rotations of sensors in the central station. There is a visible correlation between sensor position and offset, resulting in a bowing of the complete central detector station.

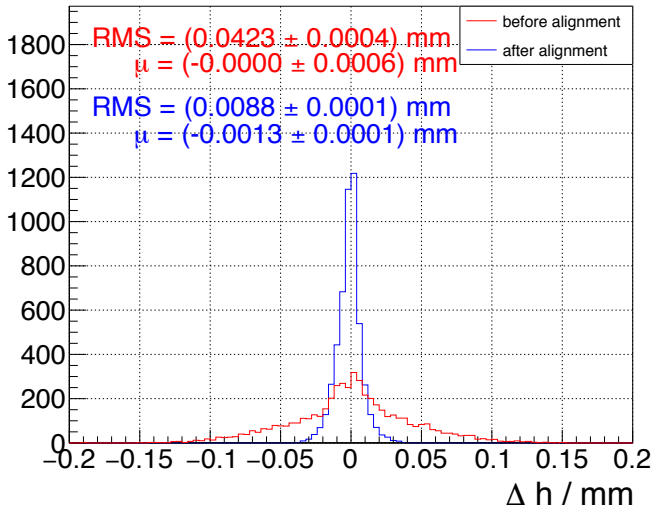

FIGURE 6.6: Deviations from a flat surface before and after two alignment iterations of the central detector station.

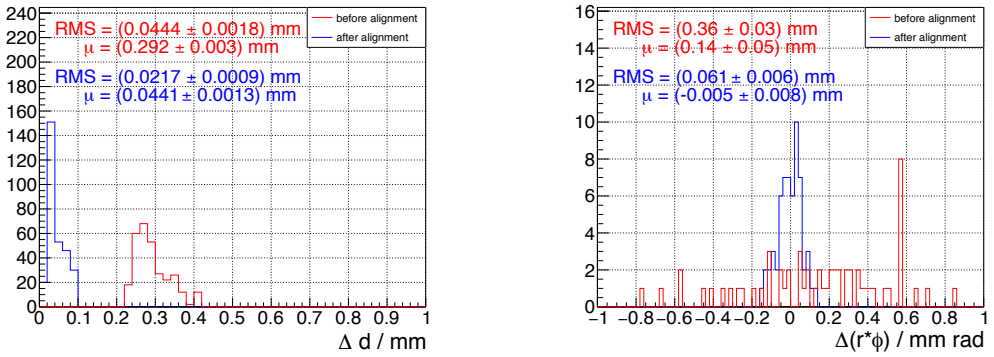

(A) Absolute offsets from the true sensor position.

(B) Deviation in $r\phi$ from the true sensor position.

FIGURE 6.7: Offsets before and after two alignment iterations of one pixel layer utilising the hierarchy alignment.

Hierarchy Alignment

For this case, one pixel layer was misaligned by arbitrary angles in the order of 1 mrad and shifts in the order of 100 µm. As shown in Figure 6.7, after one alignment iteration of only said layer (i.e. six alignment parameters) with 100 000 track candidates each from cosmics and positive muon decay in the target, the leftover absolute offset is down to about half a pixel pitch, whereas the resolution in $r\phi$ was improved by a factor of six and its bias shrank from 140 µm to -5 µm.

The study of these special scenarios shows the general capability of MU3EPIXAL to perform a track based alignment for the relevant parameters. The following section is devoted to the alignment of the estimated misalignment scenario after detector assembly and combines therefore all of the above modes and extends them to the whole detector.

6.2.2 Deriving a Strategy for the Full Tracker Alignment

The largest expected misplacements of a sensor stem from misalignments at hierarchy levels higher than the sensor itself, i.e. ladder, module and layer misalignments. It is therefore crucial to find a strategy that provides good results for these composite detector parts. In the following, various hierarchy alignment strategies for the *Mu3e* tracker will be presented and the most promising one will be used further and ultimately discussed and analysed in more detail in subsection 6.2.3. Beware, the in this section presented results don't include the alignment at sensor level; there is no reason to believe that a valid strategy for hierarchy alignment can not provide a good basis for the alignment at sensor level.

Standard Settings

If not otherwise stated, the following studies will use the settings below.

Internal Iterations For the rejection of outliers, MILLEPEDE-II provides the option to perform multiple iterations of the local (track) fit with updated global (alignment) parameters. In each step, a cut on χ^2/ndf is applied to reject badly reconstructed tracks (see subsection 5.3.3 for more information). Five internal iterations are performed and cuts of 30, 6, 2.45, 1.56 and 1 are applied successively.

Prior Knowledge MILLEPEDE-II allows the inclusion of a-priori-knowledge about the misalignment in form of so called "pre-sigmas". They limit the step width per internal iteration to possibly suppress weak modes. The input misalignments (cf. Table 4.1) are used here. For all lower level parts, the assigned pre-sigmas correspond to a tenth of the input values, forcing MILLEPEDE-II to prefer the movement of layers over lower level corrections.

Solving Method MILLEPEDE-II provides the user with the choice from a variety of methods to solve the overall matrix equation. Here, solving via inversion is chosen, since it offers errors on the parameter corrections.

Outlier Downweighting Outlier hits can be weighted down in different ways (see subsection 5.3.3). The settings chosen here are such that in the first internal iteration no downweighting is applied, the second and third iteration are down weighted with the help of Huber functions and the fourth with a Cauchy function (see [41] for more information).

Constraints Linear constraints are applied such that the movements of all sensors in a ladder sum up to zero; the same principle was applied for ladders per module and modules per layer. Layer movements were constrained by external measurements.

Failsafe Alignment parameters for which less than 1000 measurements were available, were deactivated for the alignment process. This has the advantage that weakly constrained parameters cannot distort the overall alignment because of constraints. The downside is that sensors without high statistics cannot be aligned[6].

Track Data Selection

In this section, the effects assorted track data selections have on the alignment result will be presented. The *Mu3e* software suite allows the use of positive muon

[6]This however is not an issue, since their effect on track reconstruction is therefore negligibly small.

Case	μ^+	μ^-	**cosmics**
μ^+	300k	0	0
μ^++	150k	0	150k
$\mu^+\mu^-$	150k	150k	0
all	100k	100k	100k
cosmics	0	0	300K
cosmics+	50k	50k	200k

TABLE 6.1: Alignment case study for different track samples. Given are the included number of track candidates.
Since there is no significant difference expected between using only μ^+ data or only μ^- data, the "only μ^-" case was omitted.

Indicator		μ^+	μ^+**+**	$\mu^+\mu^-$	***all***	***cosmics***	***cosmics+***
Δd [mm]	mean	1.075	0.293	1.229	0.306	0.419	0.403
	width	0.182	0.134	0.281	0.139	0.190	0.198
$\Delta(r\phi)$ [mm]	mean	-0.240	-0.042	-0.667	-0.043	0.021	-0.036
	width	0.895	0.422	0.873	0.459	0.670	0.675

TABLE 6.2: Alignment case studies for various track data selections.

decays, negative muon decays and cosmics. In the future, Mott scattering will be fully implemented[7] to make use of another breed of trajectories.

For the purpose of these studies, the estimated realistic scenario from Table 4.1 was used and six alignment iterations have been performed, aligning only for composite parts of the detector, i.e. ladders, modules and layers (cf. Figure 2.10). Table 6.1 shows an overview over the studied datasets and the results are summarised in Table 6.2. It shows that - with absolute offsets of more than 1 mm - the alignment without cosmics leads by far to the worst results. The other studied cases lead to similar results, with the "μ^++" case resulting in the best outcome. Further studies will nevertheless be using the "all" case, since it provides more data and more variety in track types[8]. Hence, for further studies, equal amounts of track candidates from positive and negative muons and from cosmics are used. However, the results also show that it is possible to obtain reasonable alignment results even when using only cosmic data. This is a big advantage, since it means track based alignment can be performed even before beam data is available.

Figure 6.8 shows the offsets of all sensors in global y-direction (perpendicular to the beam axis) as a function of their respective position in z (parallel to the beam axis). It can be seen that although the recurl stations as well as the central station

[7] In general, the use is already possible; it needs however thorough studies before it can be reliably used for the track based alignment.

[8] Since the results are very similar, it might not be necessary to use negative muons for the real detector alignment which has the advantage that instead of having to perform additional alignment runs with negative muons, the regular *Mu3e* beam with positive muons suffices.

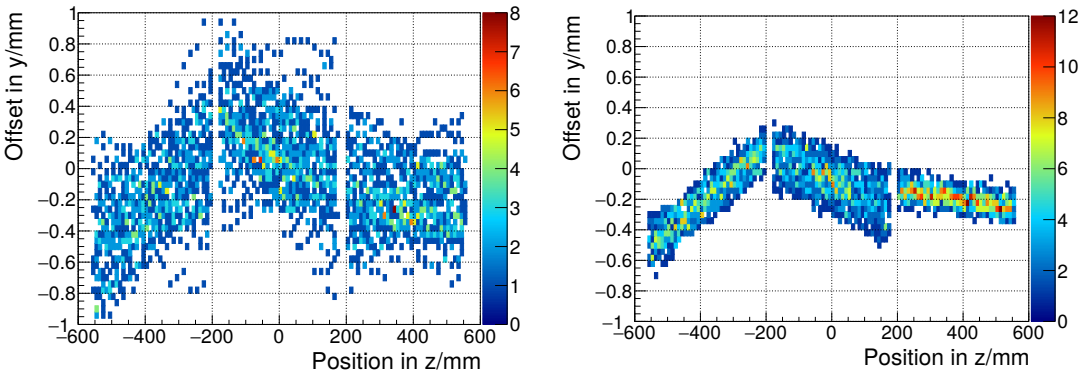

(A) Before alignment.

(B) After alignment.

FIGURE 6.8: Sensor offsets in global y-direction as a function of sensor position in global z before and after alignment.

seem to be aligned fairly well internally, their positions and orientations with respect to each other are biased, leading to offsets in the order of hundreds of micro metres. This is a weak mode particular to the *Mu3e* detector and the used data. The positions and orientations of the three stations are not well constrained with respect to each other, since trajectories of particles that connect different stations do so only after travelling relatively great distances outside the active detector volume. This means that effects of e.g. multiple scattering are more dominant than the misalignment. Since this weak mode could not be overcome with the currently available track data, additional information is required to suppress it. This is introduced in the form of external measurements.

External Measurements

As the need for external measurements was expected already, plans towards it are ongoing. A current idea is the use of a system of cameras - as presented in [15] - to determine the position of measurement markers put onto the layer endrings (cf. Figure 2.11) to evaluate the positions and orientations of the tracker layers independently from track data. The usage of external measurements was implemented into the software framework to be able to constrain the weak mode introduced above. A small tool was developed that calculates measurements for positional and rotational offset of layers by comparing the misplaced layers to the nominal ones. These measurements are written to a text file to be read in by PEDE; they are thereby included in the overall χ^2-minimisation for the alignment. This can later be easily replaced by actual measurements from an external source.

Since the alignment will make use of millions of tracks, the external measurements might need to be weighted stronger[9] to overcome the power of track data for the correct alignment of the tracking layers. A small study has been performed to find a sweet spot for the extra weight put on the external measurements and the

[9]This can be done by simply adding the measurements multiple times to MILLEPEDE-II.

Indicator		$w = 0$	$w = 1$	$w = 10^2$	$w = 10^4$	$w = 10^6$
Δd [mm]	mean	0.306	0.195	0.180	0.172	0.173
	width	0.139	0.078	0.074	0.071	0.072
$\Delta(r\phi)$ [mm]	mean	-0.043	-0.006	0.086	0.043	0.039
	width	0.459	0.209	0.157	0.165	0.171

TABLE 6.3: Results of the case studies for various measurement weights w.

results are displayed in Table 6.3. They show the critical need of external measurements for the suppression of the mentioned weak mode. The effect of putting a stronger weight onto the measurements is visible especially in the absolute sensor offsets and the width of the $\Delta(r\phi)$-distribution. But it can be seen even by eye in Figure 6.9. Since a clear advantage of using a weight of $> 10^4$ can not be deduced from here and a total number of tracks of $3 \cdot 10^5$ was used for the presented alignment results, a weight of $\frac{1}{30}N$ - where N is the number of track candidates used for said alignment run - will be used as the standard setting from now on. Although, using a greater weight would not worsen the alignment result (maybe even improve it slightly), it extends the computing time for each alignment iteration.

Conclusion and Chosen Alignment Strategy

Although there are numerous other combinations of settings to form a different alignment strategy with, the ones chosen based on the studies above result in a good enough alignment of the *Mu3e* tracking detector to state a proof of principle for reaching a suitable result after starting from an estimated scenario after detector assembly.

If not otherwise stated, the results presented in the following are based on applying the standard settings defined in section 6.2.2 while using data from μ^+- and μ^--decays and cosmics in the ratio $1 : 1 : 1$ with n track candidates from each source and external measurements for tracker layers weighted by the factor $0.1n$. The number of tracks n will be stated at the appropriate situation since the required amount of tracks depends on the number of active alignment parameters[10].

6.2.3 Results for a Full Pixel Detector Alignment

The results presented in the following are based on eleven alignment iterations, the first six of which were performed aligning only for offsets and rotations of composite detector parts, using $n = 10^5$ track candidates from each discussed source. Afterwards, five more iterations - this time with $n = 10^6$ - where only the positions, orientations and surface deformations of pixel sensors were active alignment

[10] Aligning only composite parts needs far less statistics than the alignment of individual sensors (cf. subsection 5.3.2).

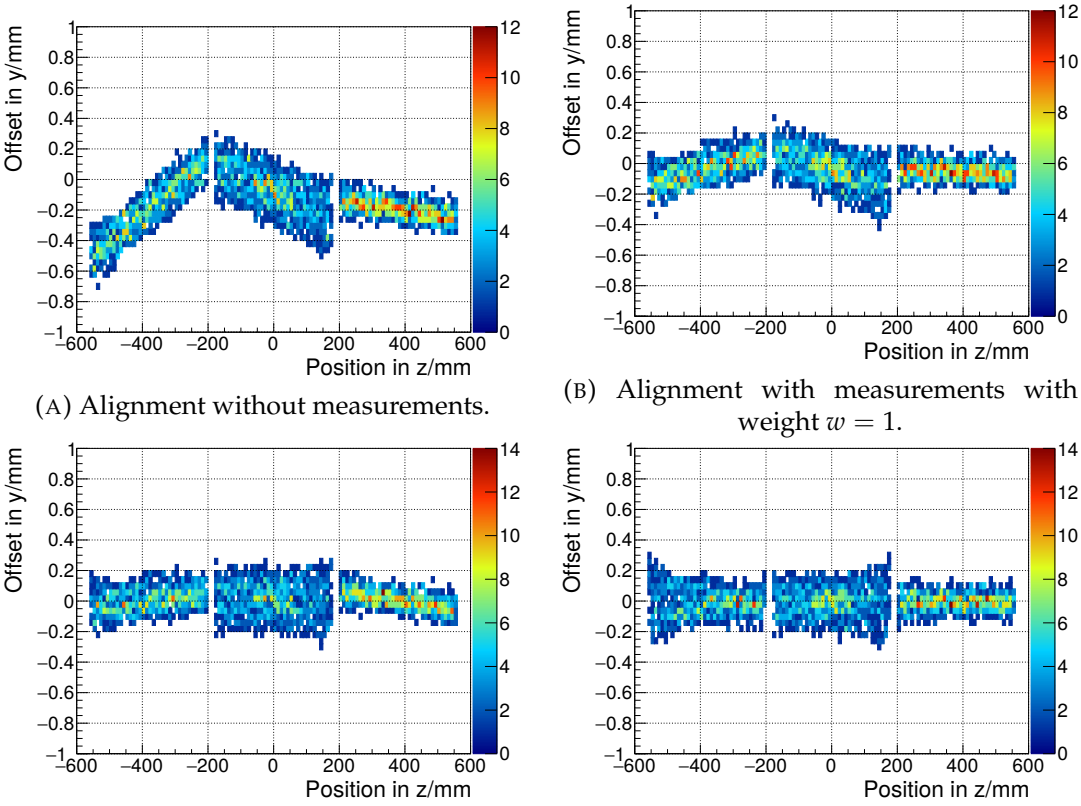

(A) Alignment without measurements.

(B) Alignment with measurements with weight $w = 1$.

(C) Alignment with measurements with weight $w = 100$.

(D) Alignment with measurements with weight $w = 10^4$.

FIGURE 6.9: Sensor offsets in global y-direction as a function of sensor position in global z for differently weighted external measurements.

parameters, were executed. In the latter case, the overall movement of all sensors was set to sum up to zero, therefore fixing the centre of mass of the whole detector[11]. The included processes were set up to make use of multiple CPU threads in parallel. By using an average of about 28 threads, the first six steps took about 30 min each. Aligning for all sensors however takes far longer, since the number of alignment parameters is significantly higher[12]. The track reconstruction and MU3EPIXAL took about 40 min and the χ^2 minimisation performed by PEDE took about 4.75 h for each of these alignment steps to complete. This makes up a total runtime of about 35 h for the alignment software to produce the presented results. However, this can be significantly reduced simply by iterating fewer times, since - as will be shown - this should suffice to reach equivalent results. Further reduction is also possible by optimising the number of used track candidates and reconstructed data.

Comparison to the True Geometry

For a comparison between aligned and true geometry, the previously discussed parameters Δd and $\Delta(r\phi)$ are again the figures of merit. The alignment algorithm is able to improve both by about a factor of four with respect to their initial misalignment. Figure 6.10 shows that the width as well as the mean values for both the absolute offset and the offset in $r\phi$ are improved significantly. However, the goal for the absolute offset set in chapter 4 - i.e. smaller than 50 µm - can currently not be reached starting from the estimated "after-assembly scenario". Furthermore, a bias in $r\phi$ of about half a pixel size remains. Based on the result after the eleven alignment iteration, several attempts on "finetuning" the result have been conducted. Neither the usage of a factor of ten more data, nor the selective use of tracks (only short tracks or only long tracks) or alignment parameters (only central station, only rigid body alignment parameters) proved to be promising. Independent of the number of iterations performed, the obtained results were never significantly better than the ones displayed in Figure 6.10.

There are some sensors with extraordinarily large offsets left after the alignment. In Figure 6.11, the absolute offset as a function of measurements used for the alignment of the corresponding sensor is displayed. Clearly, the statistics affect the outcome for the alignment. The sensors with the largest misplacements are the ones that are not aligned at all; they were excluded because of the low number of available tracks passing the sensors. Figure 6.12 displays where in the detector the sensors with the leftover misplacements are situated. In Figure 6.12a, it can bee seen that the alignment precision is worse for the outer detector layers than the inner layers This is mostly due to the weakly constrained alignment of the z-position for the recurl stations (cf. Figure 6.12b). Figure 6.12c slightly shows the - now for alignment at the sensor level - again emerging weak mode of the rotation of stations with respect

[11] This was different for the alignment of composite parts as introduced in section 6.2.2

[12] A hierarchy alignment for the *Mu3e* tracking detector includes 1350 parameters, whereas the pixel sensor alignment includes 36972 parameters.

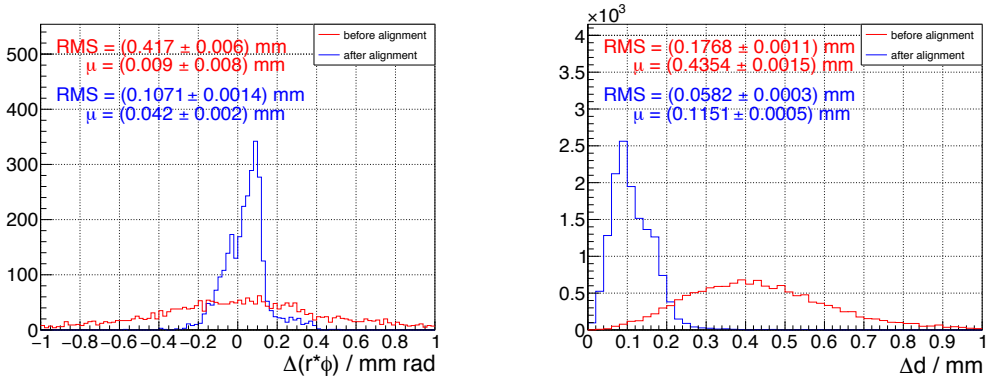

(A) $\Delta(r\phi)$ before and after the alignment.

(B) Absolute offset; measured at the corners and the centres of all sensors.

FIGURE 6.10: Geometry comparison between misaligned and aligned detector.

to each other (the recurl station in positive z-range is rotated) and in Figure 6.12d and Figure 6.12b, a worsening of the alignment precision for sensors at the end of all stations can be seen. This is due to the lower statistics available for the outer sensors which was mentioned before.

However, since the difference to the nominal geometry will neither be known nor can it be a relevant indicator of the real detector, it makes sense to look at how much the alignment can improve the performance of the tracking detector with respect to the misaligned scenario.

Effects on the Tracking Performance

The most important task of MU3EPIXAL is the improvement of the results of *Mu3e* by eliminating the negative effects misplaced sensors have on the performance of the pixel detector. In the following, indicators of said improvement and a study of the best currently possible alignment results with regards to these indicators, will be presented.

Indicators for the Alignment Quality To quantify the goodness of the alignment result without knowing the true geometry, the following parameters were used as indicators:

- track reconstruction efficiency
- momentum resolution
- distribution of the measured momenta of positrons originating from a Michel decay (also known as the "Michel spectrum"); especially the "Michel edge"
- signal reconstruction efficiency
- resolution and position of the reconstructed signal vertex.

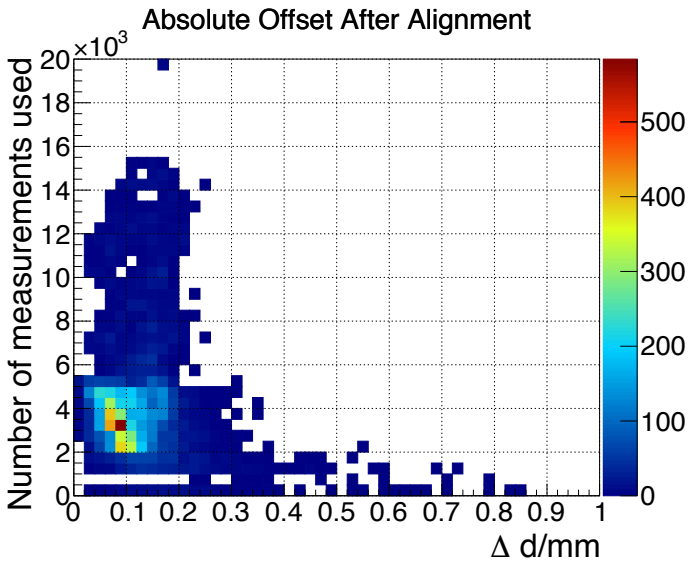

FIGURE 6.11: Remaining deviation from nominal position after the alignment as a function of the number of measurements used for rigid body alignment.

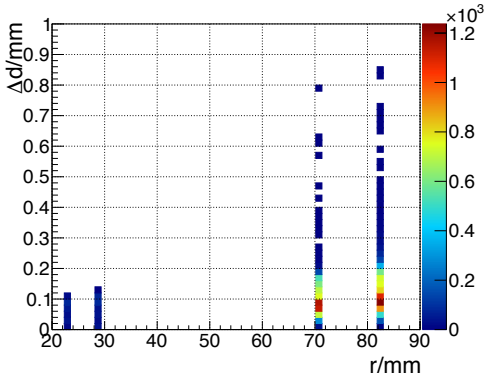

(A) Absolute offset as a function of radius.

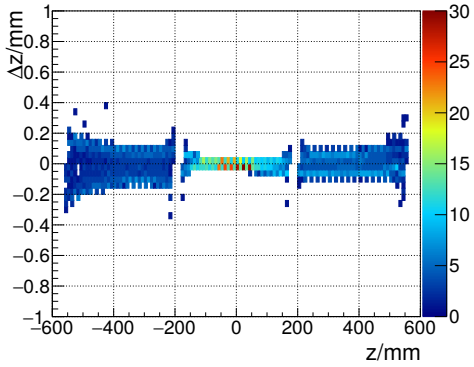

(B) Offset in x as a function of position in z.

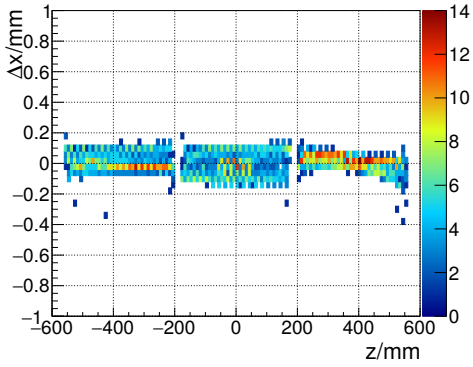

(C) Offset in x as a function of position in z.

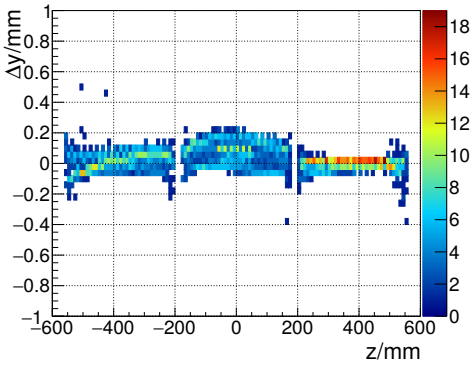

(D) Offset in y as a function of position in z.

FIGURE 6.12: Leftover sensor misplacements after alignment of the complete pixel detector.

Parameter	*nominal*	*misaligned*	*aligned*
efficiency [%]			
short tracks	97.333 ± 0.026	57.510 ± 0.080	97.348 ± 0.026
long tracks	73.118 ± 0.072	34.159 ± 0.077	73.152 ± 0.072
momentum resolution [MeV c^{-1}]			
short tracks	2.628 ± 0.003	4.271 ± 0.006	2.635 ± 0.003
long tracks	1.341 ± 0.002	1.645 ± 0.003	1.337 ± 0.002

TABLE 6.4: Tracking performances for the nominal, a misaligned and the re-aligned pixel detector. Resolutions correspond to the RMS of the difference between reconstructed and true momentum. It has been renounced to state the upper and lower errors for the given efficiencies (efficiency errors are in general asymmetrical), since they are identical to at least a level of 10^{-3}%.

There are numerous more parameters one could investigate; since this would be beyond the scope of this work, the quantities above, found to be the most crucial ones, were selected. For the analysis of the general reconstruction performance, a data sample of roughly 1.3 million tracks from muon decay products (mostly Michel positrons) were utilised. For the signal analysis, 1 million signal decays were simulated and studied.

Table 6.4 shows the improvement on the tracking efficiency and momentum resolution for short tracks and for long tracks, MU3EPIXAL provides. The efficiencies of the nominal detector and the re-aligned detector agree with each other at the per mille level. The same is true for the momentum resolution of short tracks. For long tracks, a very small improvement with respect to the momentum resolution of the nominal detector was measured which can occur due to selection effects; only the tracks which can be reconstructed very well get reconstructed at all.

Another important quality factor for tracking is the momentum resolution as a function of true momentum. In case of a loss in efficiency, it is essential to know if it is predominantly in a specific range of momenta or equally spread. Figure 6.13 shows that the momentum resolution of the misaligned detector rises with the momentum. The alignment software however can negate the effect completely with the result that for all momentum ranges, the resolution is essentially identical to the nominal one.

The shape of the Michel spectrum and the position of its edge are well defined and can therefore be a useful tool for detector calibration. Since the momentum of a positron that originated from a muon decay can not exceed half of the muon mass, a hard cut at about 52.9 MeV in the measured momenta coming from said particles is expected[13]. Because of the detector acceptance, not the whole spectrum can be measured by *Mu3e*; that's the reason why the Michel spectra displayed in the following deviate from the typical shape, even for the nominal detector alignment.

[13]Because of the finite momentum resolution, the measured edge will however be smeared out.

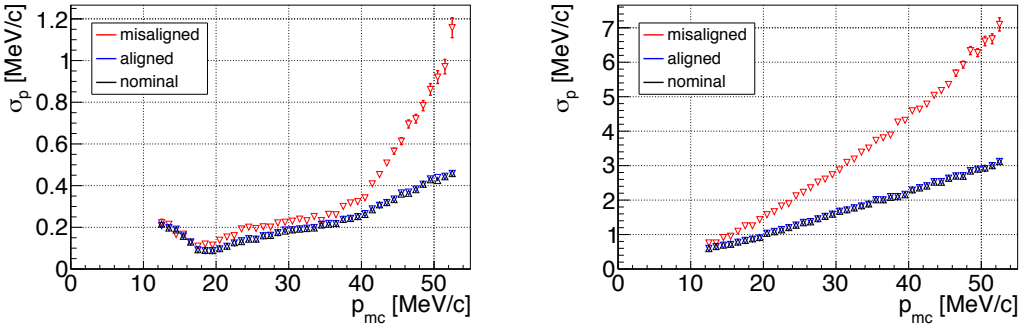

(A) For only long Tracks.

(B) For only short Tracks.

FIGURE 6.13: Momentum resolution as a function of true momentum. The σ corresponds to the width of a Gaussian fit to the difference between true and measured momentum.

Parameter	*nominal*	*misaligned*	*aligned*
efficiency (all) [%]	37.32	2.45	37.32
efficiency (long) [%]	20.60	0.61	20.60

TABLE 6.5: Total efficiency for reconstructing phase-space signal events for requiring no recurlers (all) and three recurlers (long). This includes the geometrical detector acceptance, track and vertex reconstruction and selection inefficiencies.

Particles with too low momenta ($\lessapprox 10\,\text{MeV}$) don't reach the outer tracker layers and are therefore not reconstructed. On the other hand, if their momenta are too high, they might not recurl before passing the recurl stations and will therefore also not be reconstructed. Figures 6.14 and 6.15 show comparisons of the Michel spectra of the misaligned and the aligned to the nominal detector respectively. The spectrum is clearly heavily affected by misplaced sensors. After alignment, the spectrum matches the one for the nominal geometry in great detail.

For every reconstruction step there is the possibility of losing signal data; most of which due to the geometrical acceptance of the detector but also due to applied cuts. Misalignment can negatively affect the signal efficiency and the reconstruction of the vertex position which would be a huge drawback for the success of *Mu3e*. Table 6.5 lists the total efficiency for reconstructing signal events. In Table 6.6, the reconstructed vertex positions of signal decays with their resolutions are denoted[14]. The efficiencies and the vertex resolution of the aligned almost perfectly resemble the values for the nominal detector, whereas the reconstructed vertex position reveals a small bias in x and y.

According to the studies performed in the context of this thesis - which are not limited to the ones presented here -, the alignment programme delivers results good

[14]The here cited numbers were obtained from the fits presented in Figure F.5

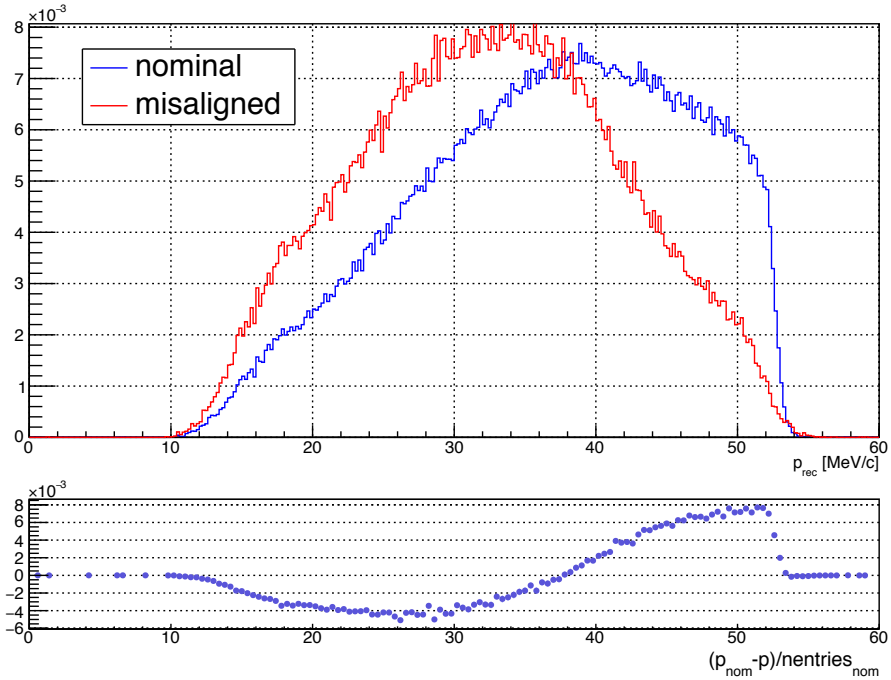

FIGURE 6.14: Reconstructed momentum of Michel positrons for the nominal detector versus the (estimated) detector after assembly. The lower graph shows the relative difference between the two.

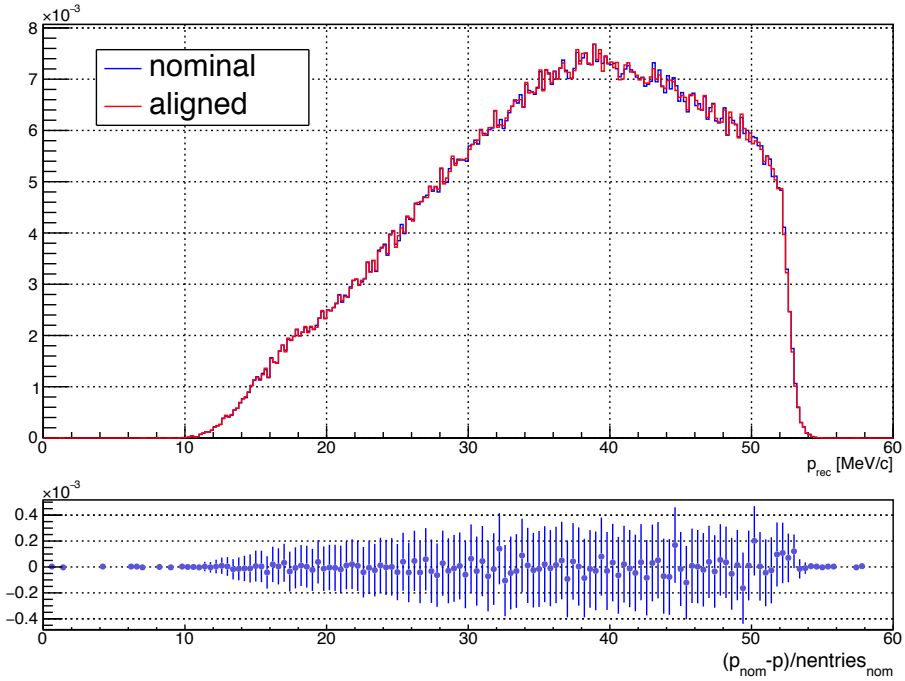

FIGURE 6.15: Reconstructed momentum of Michel positrons for the nominal detector versus the detector after sensor alignment. The lower graph shows the relative difference between the two.

Parameter		*nominal*	*misaligned*	*aligned*
$x_{rec} - x_{true}$ [mm]	mean	0.001 ± 0.001	0.300 ± 0.012	-0.018 ± 0.001
	width	0.289 ± 0.002	0.672 ± 0.009	0.289 ± 0.002
$y_{rec} - y_{true}$ [mm]	mean	-0.001 ± 0.001	-0.262 ± 0.008	0.058 ± 0.001
	width	0.286 ± 0.002	0.580 ± 0.040	0.287 ± 0.002
$z_{rec} - z_{true}$ [mm]	mean	0.000 ± 0.001	0.001 ± 0.013	-0.006 ± 0.001
	width	0.194 ± 0.001	0.760 ± 0.019	0.194 ± 0.001

TABLE 6.6: Results of the vertex reconstruction of signal events with three recurlers required; for a nominal, a misaligned and an aligned detector. The mean stems from a fit of the sum of two Gaussians and the quoted width is the area-weighted mean.

enough to reproduce detector performances that almost exactly match the ones for the nominal detector. The results are better than expected considering the geometrical deviations, meaning the tracking does not seem to be sensitive to the kind of misplacements that are left after alignment.

Possible Optimisations

Although the results of MU3EPIXAL considering tracking performance are already satisfying, improvements can and should still be accomplished in the future. One of them is the time taken to reach a result. Figure 6.16 displays the absolute offset and the offset in $r\phi$ of all sensors as a function of alignment iterations. It becomes clear that the number of iterations can be cut at least in half,conserving the computing time necessary to reach a comparable result[15]. Another prominent feature of Figure 6.16 is the fact that the hierarchy alignment achieves results that are already quite good, allowing the user to obtain usable geometry description in less than three hours, where only a few 100 000 tracks are necessary.

That the alignment at sensor level can not simply be neglected is shown for example in Figure 6.17. Without it, the Michel edge is not correctly reproduced.

Weak Modes

None of the weak modes presented in section 5.8 could be observed after alignment (this can be seen in Figures F.7 and F.8). However, exploiting every currently possible setting, various different alignment runs have been performed without successfully obtaining better corrections than the ones presented in the previous sections. The reason for this is the weak mode of rotated stations visible in Figure 6.8 which is possibly closely connected to the one visible in Figure 6.5. Those two combined currently prevent the alignment software from further improvements. In the following,

[15] It makes sense however to perform more iterations during the development phase, since one wants to see the algorithm converge.

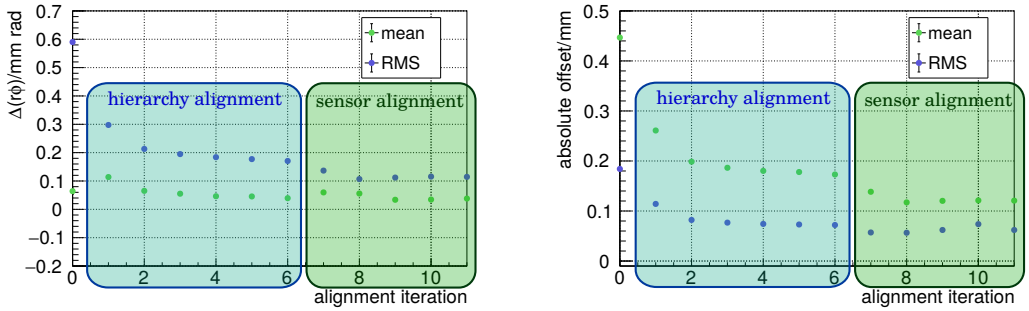

(A) $\Delta(r\phi)$ as a function of alignment iteration.

(B) Absolute average offset at a sensor corner as a function of alignment iterations.

FIGURE 6.16: Step 0 corresponds to the initially misaligned one, every other step corresponds to the results after the n ($n > 0$) steps.

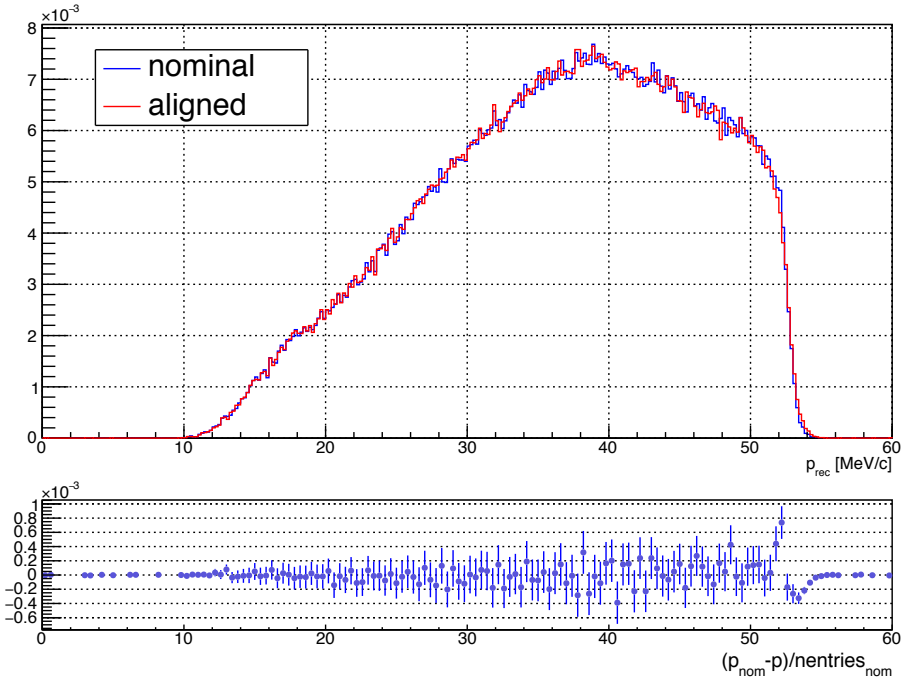

FIGURE 6.17: Reconstructed momentum of Michel positrons for the nominal detector versus the detector after the alignment of only composite parts. The lower graph shows the relative difference between the two.

ideas to overcome this issue, the pursue of which would exceed the scope of this work, are briefly presented.

Improvement in local track fit The local track fit included in MU3EPIXAL provides a basis for the χ^2 minimisation performed by MILLEPEDE-II. An incorrect implementation (e.g. by a wrong error estimate of the trajectories and therefore a wrong χ^2 of the local track fit) can lead to distortions of the χ^2 function in MILLEPEDE-II, ultimately provoking biased results.

Fake Tracks MU3EPIXAL currently uses all data provided by *Mu3e*'s track reconstruction programme. Systematically wrongly reconstructed tracks which could impact the alignment might occur and should be rejected for alignment purposes.

Different Track Types The advantage from utilising different track types is already apparent when looking at Table 6.2. A larger variety from Mott scattering for example can further enhance the results. However, all the currently usable track data types have already been exploited.

Running without magnetic field Playing into the previous point, this will also provide a different breed of track. The use of straight tracks however is not yet fully implemented in MU3EPIXAL.

Improve Reconstruction of Cosmics Cosmics, as how they are currently implemented, are very susceptible to misalignment. Hence, misplacements in the pixel detector strongly affect the χ^2 of the local track fit for cosmics much more than they affect other data types. The cut on χ^2 performed in the internal MILLEPEDE-II iterations then leads to a bias in the usage of data types.

Using the Michel edge The measured Michel edge position should be independent of the azimuth angle ϕ. However, if such a correlation can be seen, this should indicate a deformation of the pixel detector. This can assist in detecting possible weak modes without knowing the true geometry.

Bowing of composite parts The weak mode of bowing of the layers discussed in section 6.2.1 could be suppressed by adding parameters for the bowing of composite detector parts. This needs to be implemented in any case, since gravitational force will evoke a sagging of longer ladders. This might even assist in resolving the weak mode of the mutual alignment of stations.

Chapter 7

Conclusion and Outlook

7.1 Conclusion

The *Mu3e* experiment is a precision experiment searching for the lepton flavour violating decay $\mu^+ \to e^+e^-e^+$, which is theoretically possible, but heavily suppressed in the Standard Model of particle physics. Any observation of this process would be a clear indicator of new physics. To achieve the sensitivity goal of one in 10^{16} decays, a large number of muon decays must be observed and background processes must be efficiently suppressed. This can only be accomplished with excellent resolutions with respect to momentum, vertex position and timing. A novel detector technology - high voltage monolithic active pixel sensors (HV-MAPS) - allow high rates while still holding the material budget to a minimum. Almost 3000 of those sensors are arranged as concentric barrel-shaped layers in three stations; one central station consisting of four layers and two recurl stations consisting of two layers each. Together with the applied magnetic field of 1 T this allows for a precise reconstruction of particle trajectories. However, misplacements of the pixel sensors, as they will occur in the detector, lead to impairments or even a prevention of the reconstruction. An alignment programme that can reliably account for the misplacements is therefore an essential ingredient for the success of *Mu3e*.

In the context of this thesis, MU3EPIXAL, the software to perform track based alignment for the *Mu3e* pixel detector utilising the General Broken Lines fit and MILLEPEDE-II was created. Additionally, a tool to modify the geometry for a simulated detector - MU3EMISAL- was developed, allowing the investigation of effects, various expected misalignment scenarios have on the detector performance.

To examine, how intensively misplacements in the pixel detector affect its tracking performance, various scenarios were analysed, including an estimate of the misalignment right after detector assembly. The main goal of this work was to deliver a solution for obtaining a usable geometry when starting with said estimated scenario after construction. To start off, the alignment software was tested on real data obtained with telescopes developed for prototyping the MUPIX chip, the HV-MAPS used in *Mu3e*. For this special case, where all sensors are aligned approximately parallel to each other along the particle beam without magnetic field, precisions of less than 2 µm were regularly achieved. Scaling this up to the *Mu3e* detector, where

the chips are positioned in concentric barrel-shaped layers around the particle beam inside a magnetic field, is not a trivial task. Additionally, for this geometry, deformations of the sensor surfaces, which are expected because of their thickness of only 50 µm, play a role. MU3EPIXAL is able to reduce the initial average absolute offset of about 440 µm in the "after-assembly-scenario" to roughly 110 µm in less than two days while using a reasonable amount of data. The cause of the remaining misalignment was found to be a weak mode particular for the *Mu3e* pixel detector and the available beam data. Although it was shown that the sensors inside the central and the recurl stations can in general be aligned to higher precision, the rotations of the three stations with respect to each other as well as bows of the detector layers can not be sufficiently well aligned with the available data. The possibility for including external measurements was therefore implemented in MU3EPIXAL to suppress these weak modes. Although the results were thereby improved, they are currently not satisfying concerning the overall leftover misalignment. Attempts to improve the alignment further were presented, did however not lead to a better result, since it is currently not possible to fully overcome the presented weak mode. Suggestions for approaches to recuperate the results that go beyond the scope of this work were made; further investigations are needed.

However, the study of the effects, the leftover misalignment has on track reconstruction, showed an almost perfect agreement with the results from a detector using the true geometry. Solely the reconstructed vertex resolution for signal decay exhibits deviations in the order of tens of µm. For the overall reconstruction efficiency, the momentum resolution, as well as the signal efficiency and the Michel spectrum did not demonstrate a significant deviation from the nominal results.

7.2 Outlook

Having completed the development of an alignment programme for *Mu3e*, next steps to fine tune the results can be made. This needs a deeper investigation of the discussed weak modes of station rotations and layer bows. Deformations of composite detector parts, like layers, need to be implemented into the alignment software as well as into the misalignment producing tool MU3EMISAL. This constitutes a chance to conquer the weak modes, allowing for a higher alignment precision. Although it was shown that it is already possible to obtain a usable geometry proceeding from a misaligned detector in a matter of an hour, optimisations regarding speed are possible and should be tackled in the future. Furthermore, the implementation of a realistic magnetic field - i.e. including possibly inhomogeneous areas - needs to be taken into account for alignment purposes.

The track based alignment for the *Mu3e* pixel detector is set on a great path to deliver excellent and reliable results which can be achieved after some fine tuning and an efficient suppression of the occurring weak modes.

Appendix A

Results of Misalignment Studies

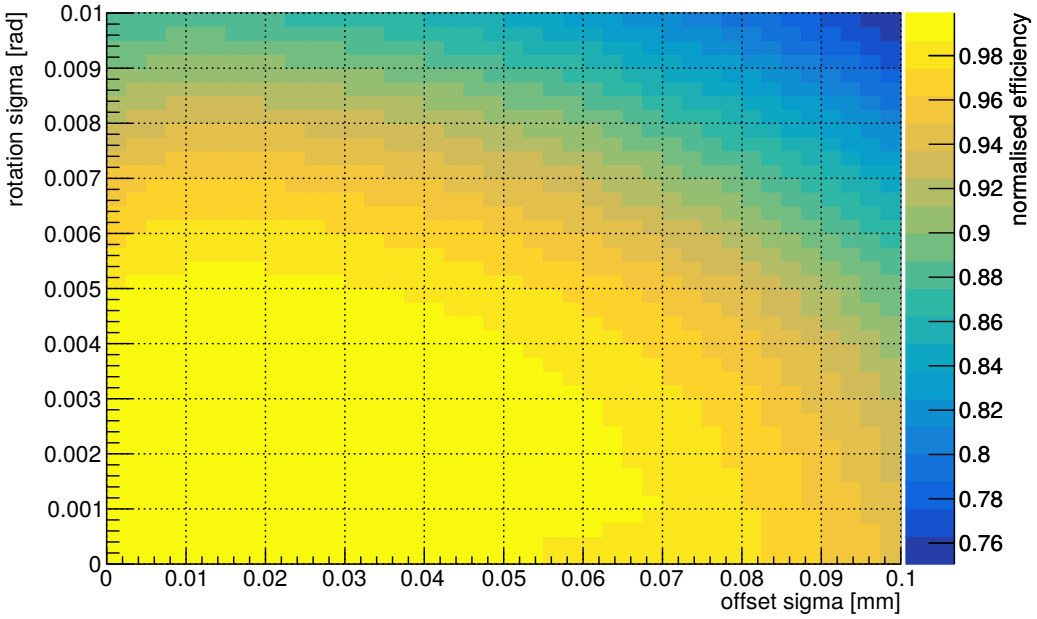

(A) Track reconstruction efficiency (normalised to a perfectly aligned detector).

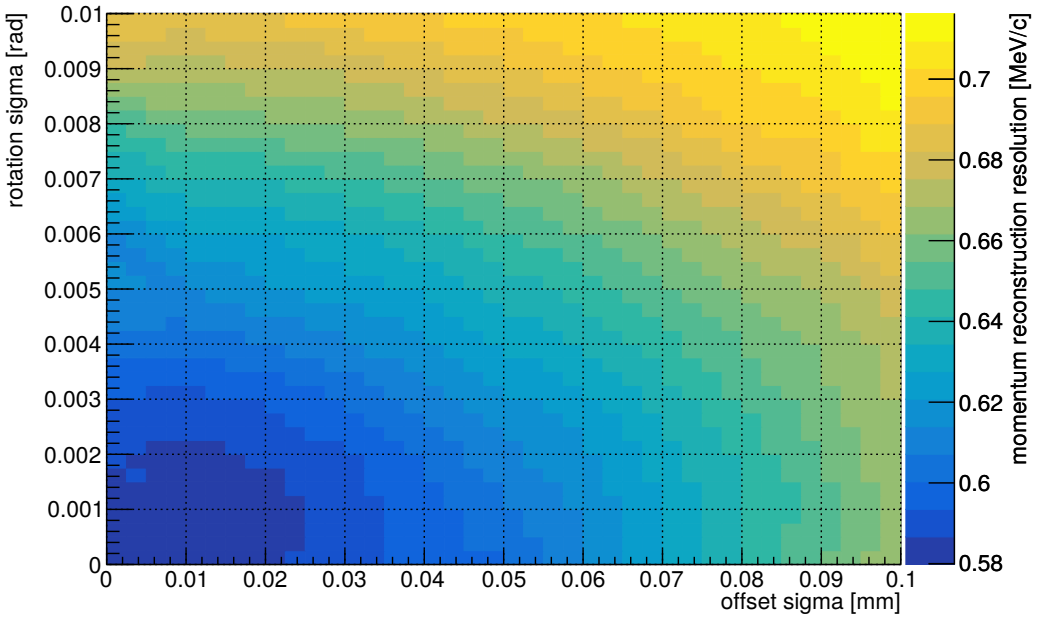

(B) Momentum resolution for long tracks corresponding to the RMS of the difference between true momentum and reconstructed momentum.

FIGURE A.1: **Individual sensor misplacements:** Effects of position and orientation misalignment of individual sensors on track reconstruction efficiency and on momentum resolution. The standard deviations of the random shifts and rotations are depicted on the x- and y-axis respectively.

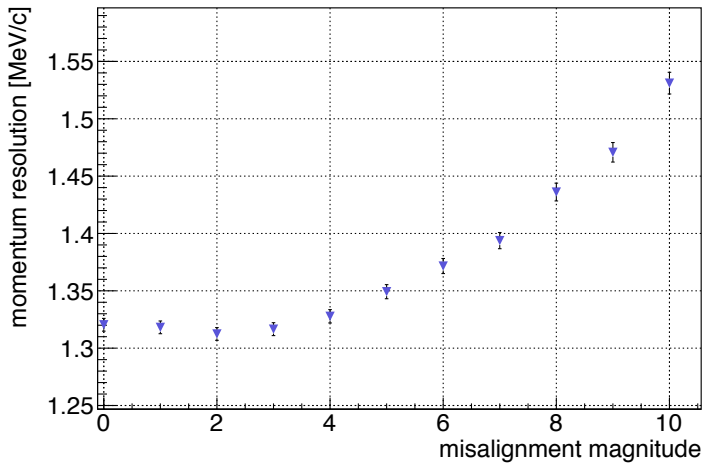

(A) Momentum resolution from RMS of the difference between reconstructed and true momentum.

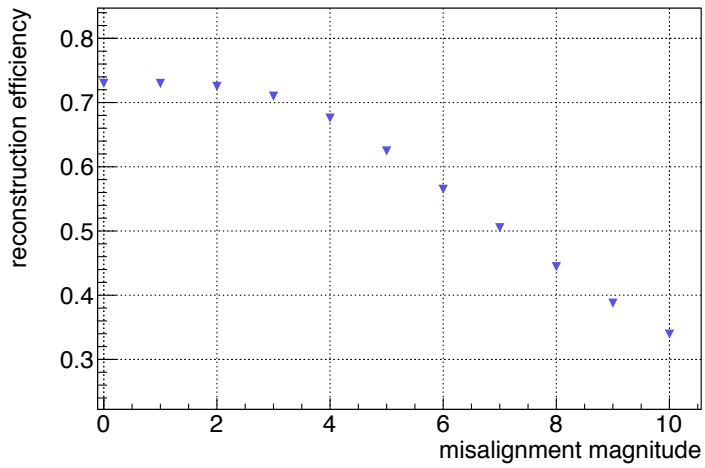

(B) Momentum reconstruction efficiency.

FIGURE A.2: **Misalignment effects on reconstruction performance:** Momentum resolution and reconstruction efficiency for long tracks (consisting of 6 or 8 hits) as a function of various misalignment magnitudes. A magnitude of 0 corresponds to the nominal detector geometry and all misplacements are being increased in consistent steps to reach the full realistic estimates from Table 4.1 at magnitude 10.

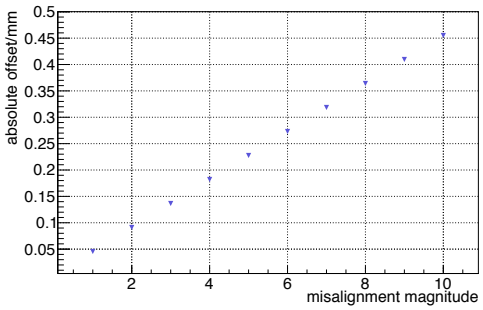

(A) Sensor corner 0

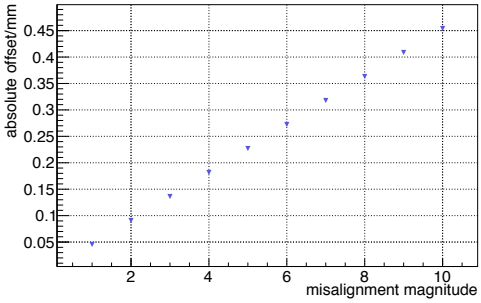

(B) Sensor corner 1

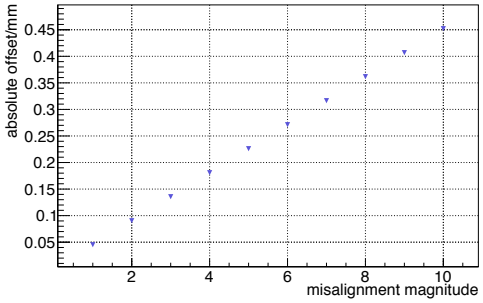

(C) Sensor corner 2

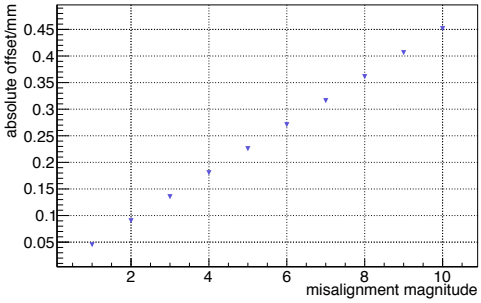

(D) Sensor corner 3

FIGURE A.3: **Average offset vs. misalignment magnitude:** Average absolute offset at the sensor corners for each misalignment magnitude. The values were obtained by calculating the absolute three-dimensional deviation at the four corners of a sensor from their nominal positions.

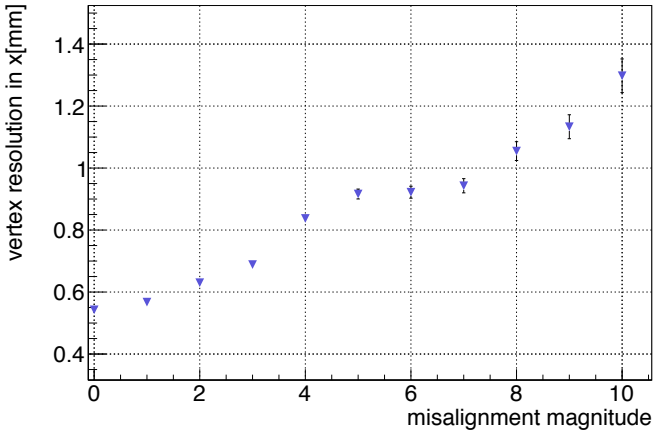

(A) Vertex reconstruction resolution in x.

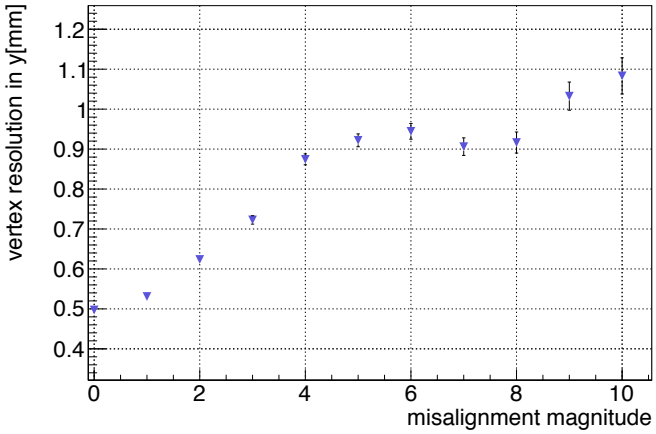

(B) Vertex reconstruction resolution in y.

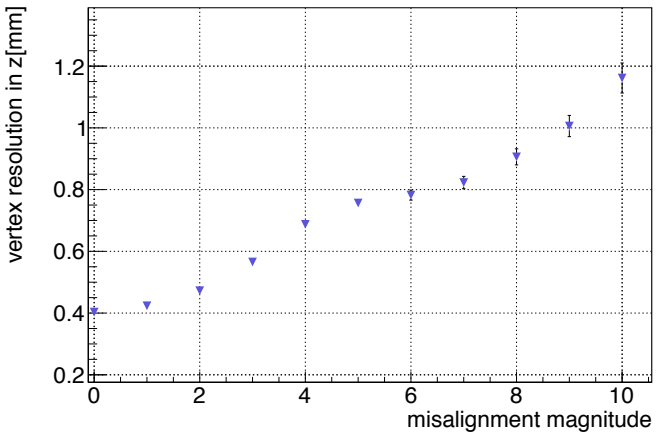

(C) Vertex reconstruction resolution in z.

FIGURE A.4: Misalignment effects on the vertex resolution. The declines starting from misalignment magnitude 6 is due to selection effects caused by the very low efficiency (Figure 4.3b).

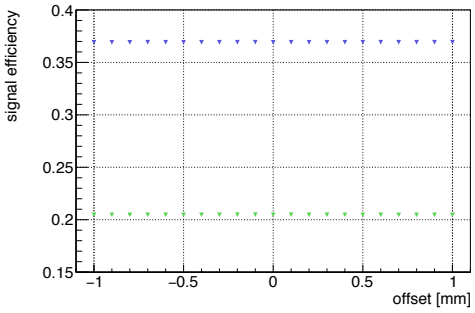

(A) Signal reconstruction efficiency.

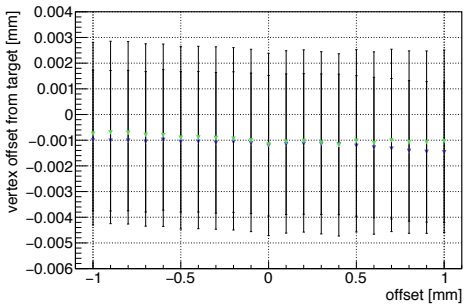

(B) Absolute offset from reconstructed vertex to target surface.

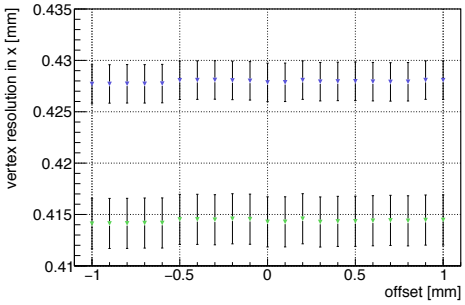

(C) Vertex resolution in x.

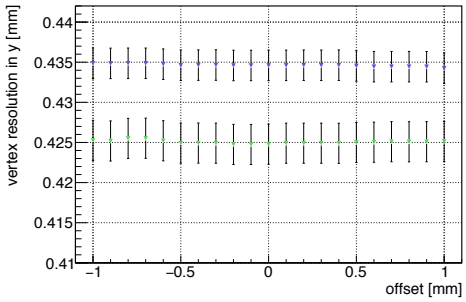

(D) Vertex resolution in y.

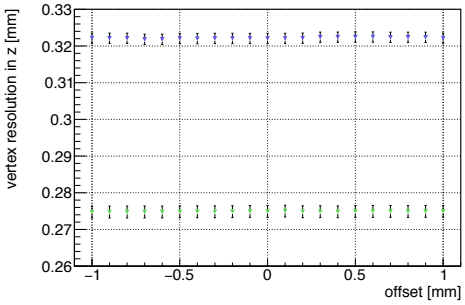

(E) Vertex resolution in z.

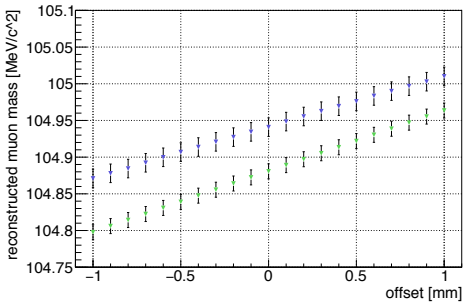

(F) Reconstructed mass of the decayed muon.

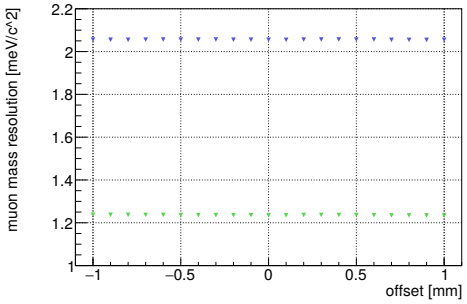

(G) Mass resolution for the decayed muon.

FIGURE A.5: **Recurl stations parallel to beam direction**: Effects on the reconstruction performance for signal decays. Each figure hosts results for utilising only long tracks (green) and for all possible tracks (blue) for reconstruction. The stated offsets correspond to the systematic misplacement of both recurl stations simultaneously towards each other (along beam direction). Hence, a negative offset corresponds to a "stretching" of the detector and a positive offset to a "squeezing".

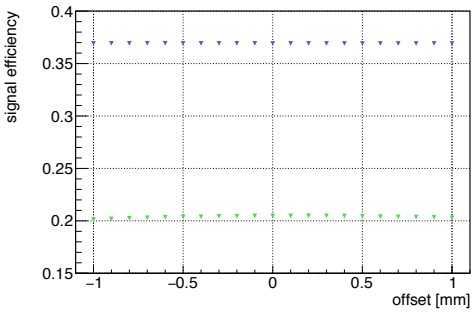

(A) Signal reconstruction efficiency.

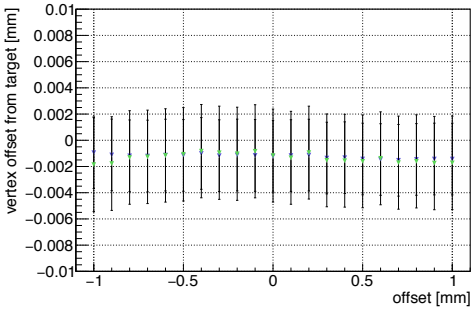

(B) Absolute offset from reconstructed vertex to target surface.

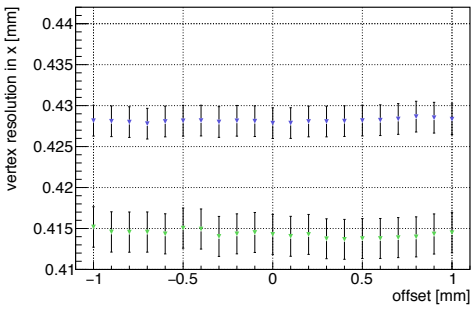

(C) Vertex resolution in x.

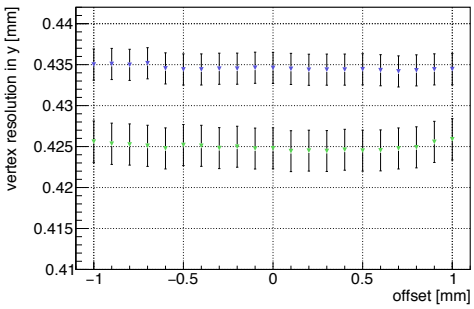

(D) Vertex resolution in y.

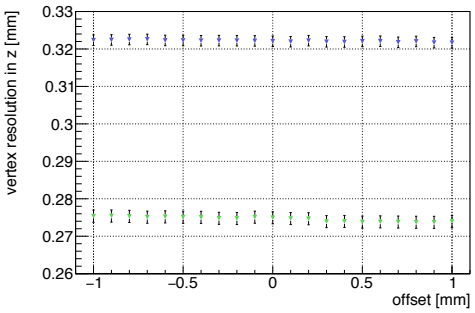

(E) Vertex resolution in z.

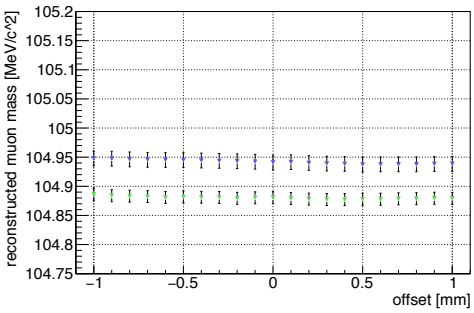

(F) Reconstructed mass of the decayed muon.

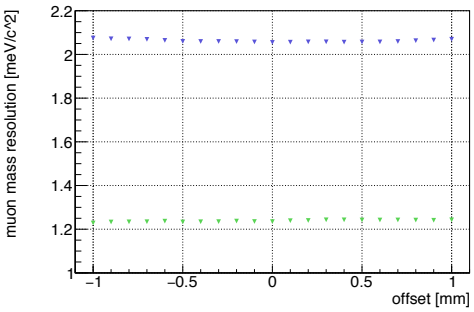

(G) Mass resolution for the decayed muon.

FIGURE A.6: **Recurl stations perpendicular to beam direction**: Effects on the reconstruction performance for signal decays. Each plot hosts results for utilising only long tracks (green) and for all possible tracks (blue) for reconstruction. The stated offsets correspond to the systematic misplacement of both recurl stations simultaneously perpendicular to the beam direction.

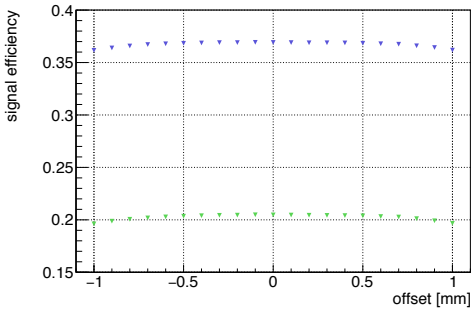

(A) Signal reconstruction efficiency.

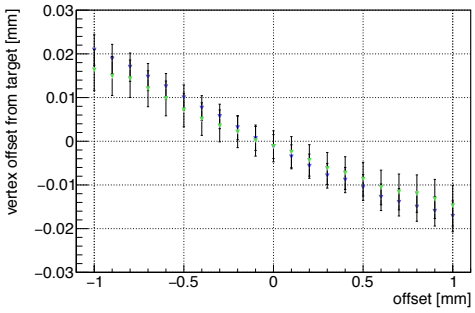

(B) Absolute offset from reconstructed vertex to target surface.

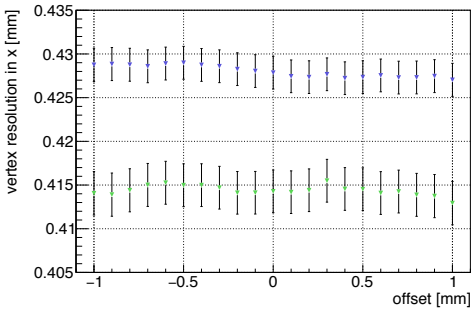

(C) Vertex resolution in x.

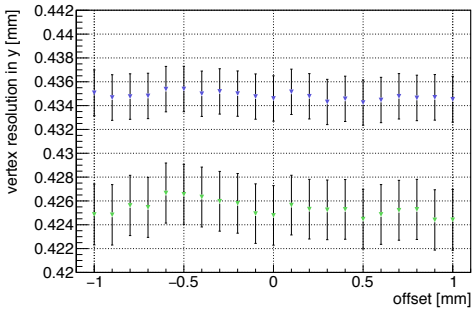

(D) Vertex resolution in y.

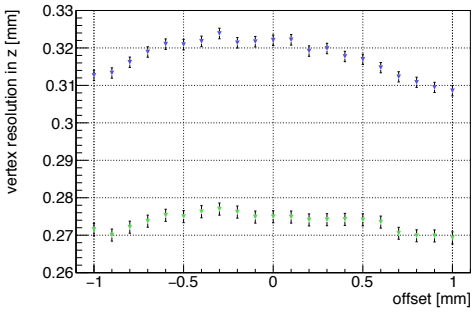

(E) Vertex resolution in z.

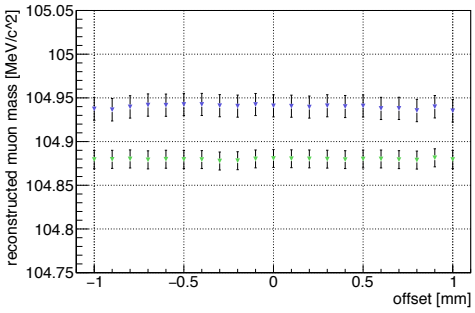

(F) Reconstructed mass of the decayed muon.

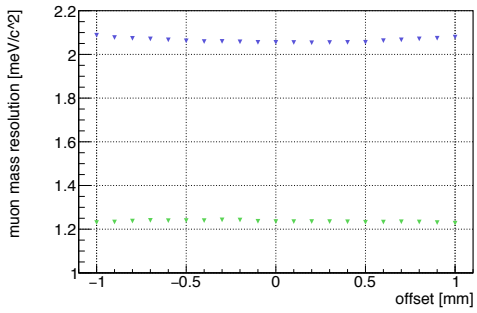

(G) Mass resolution for the decayed muon.

FIGURE A.7: **Vertex layers parallel to beam direction**: Effects on the reconstruction performance for signal decays. Each plot hosts results for utilising only long tracks (green) and for all possible tracks (blue) for reconstruction. The stated offsets correspond to the systematic misplacement of the vertex layers parallel to the beam direction, where negative offsets corresponds to upstream and positive offsets to downstream misplacements. The calculation of the vertex resolution in z is compromised due to the large offset of the reconstructed vertex from its nominal position.

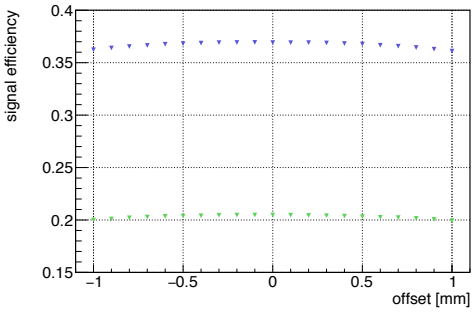

(A) Signal reconstruction efficiency.

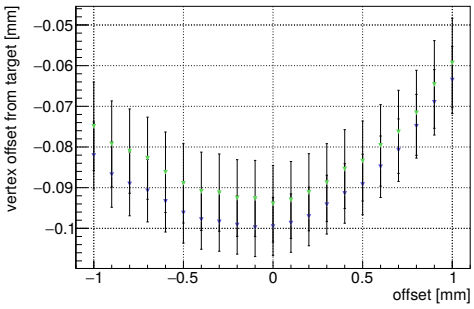

(B) Absolute offset from reconstructed vertex to target surface.

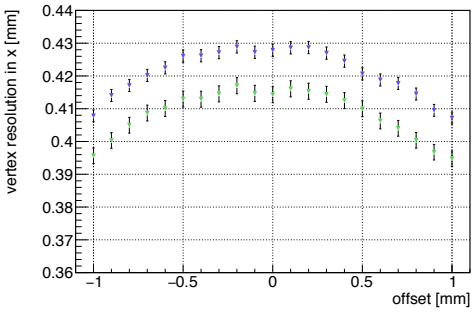

(C) Vertex resolution in x.

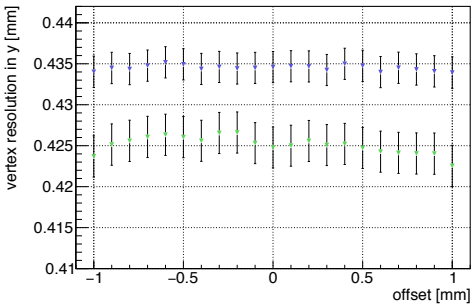

(D) Vertex resolution in y.

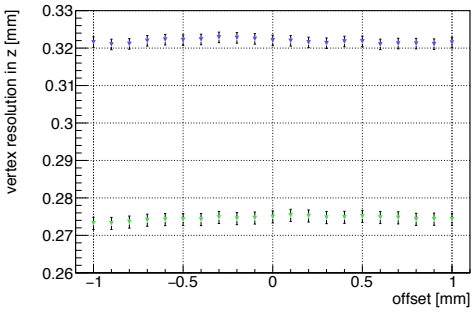

(E) Vertex resolution in z.

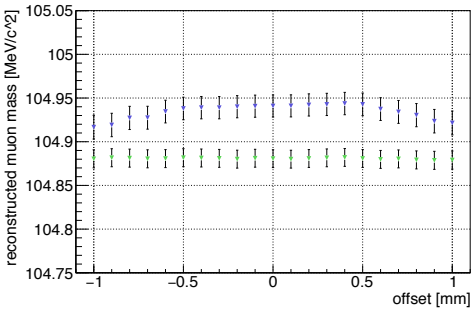

(F) Reconstructed mass of the decayed muon.

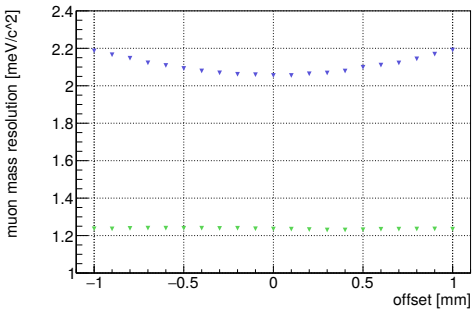

(G) Mass resolution for the decayed muon.

FIGURE A.8: **Vertex layers perpendicular to beam direction**: Effects on the reconstruction performance for signal decays. Each plot hosts results for for utilising only long tracks (green) and for all possible tracks (blue) for reconstruction. The stated offsets correspond to the systematic misplacement of the vertex layers (inner two layers) perpendicular to the beam direction. The calculation of the vertex resolution in x is compromised due to the large offset of the reconstructed vertex from its nominal position.

Appendix B

Minimisation of a χ^2 Function by Solving a Matrix Equation

B.1 Minimisation Without Linear Constraints

Starting from a residual

$$r_{ij} = m_{ij} - f_{ij}(\boldsymbol{a}_j) \tag{B.1}$$

one can define a χ^2 function as

$$\chi^2(\boldsymbol{a}) = \frac{1}{2}\sum_j \sum_i \frac{r_{ij}^2}{\sigma_{ij}^2}. \tag{B.2}$$

Here, m_{ij} is a measurement and $f_{ij}(\boldsymbol{a}_j)$ and σ_{ij} are the corresponding measurement prediction and measurement error respectively. In a track based alignment of a pixel tracker, a measurement would correspond to one dimension of a local two dimensional hit measurement and $f_{ij}(\boldsymbol{a}_j)$ to the prediction of said measurement stemming from the track fit in track j. The parameter vector $\boldsymbol{a}_j$ includes all local track parameters for track j and in addition all global parameters describing the detector geometry.

If the function $f(\boldsymbol{a}_j)$ depends non-linearly on its parameters $\boldsymbol{a}_j$ (which is in general the case for alignment purposes), an iterative procedure has to be used, where the function has to be linearised by e.g.[1]

$$f(\boldsymbol{a}_j) \approx f(\boldsymbol{a}_{0j}) + (\nabla f_{ij})^T \Delta \boldsymbol{a}_j, \tag{B.3}$$

where $\boldsymbol{a}_{0j}$ is the linearisation point and $\Delta \boldsymbol{a}_j = \boldsymbol{a}_j - \boldsymbol{a}_{0j}$.

The new χ^2 function is therefore approximated by

$$\chi^2(\boldsymbol{a}_j) \approx \frac{1}{2}\sum_j \sum_i \frac{1}{\sigma_{ij}^2}\left(m_{ij} - f(\boldsymbol{a}_{0j}) - (\nabla f_{ij})^T \Delta \boldsymbol{a}_j\right)^2 \tag{B.4}$$

[1] $(\nabla f_{ij})^T$ is the transposed gradient of f_{ij} and is defined by $(\nabla f_{ij})^T = (\frac{\partial f_{ij}(a_{j0})}{\partial a_{j0}}, \frac{\partial f_{ij}(a_{j1})}{\partial a_{j1}}, ...)$

and finding a minimum of it, by requiring its derivative to be equal to zero, results in

$$0 = \sum_j \sum_i \frac{1}{\sigma_{ij}^2} \nabla f_{ij} \left(m_{ij} - f_{ij}(\boldsymbol{a}_{0j}) - (\nabla f_{ij})^T \Delta \boldsymbol{a}_j \right). \tag{B.5}$$

With the definitions

$$\boldsymbol{b} = \sum_j \sum_i \frac{1}{\sigma_{ij}^2} \nabla f_{ij} \left(m_{ij} - f_{ij}(\boldsymbol{a}_0) \right), \tag{B.6}$$

$$\boldsymbol{C} = \sum_j \sum_i \frac{1}{\sigma_{ij}^2} \nabla f_{ij} (\nabla f_{ij})^T \tag{B.7}$$

and

$$\Delta \boldsymbol{a} = \sum_j \Delta \boldsymbol{a}_j, \tag{B.8}$$

Equation B.5 becomes equivalent to the matrix equation

$$\boldsymbol{C} \Delta \boldsymbol{a} = \boldsymbol{b} \tag{B.9}$$

which has to be solved by e.g. inverting $\boldsymbol{C}$.

B.2 Minimisation With Linear Constraints

If the minimisation is subject to linear constraints of the form

$$\boldsymbol{A} \boldsymbol{a} = \boldsymbol{c} \tag{B.10}$$

the Lagrange multiplier method can be utilised. This means, replacing the χ^2 function by the Lagrangian

$$\mathcal{L}(\boldsymbol{a}, \boldsymbol{\lambda}) = \chi^2(\boldsymbol{a}) + \boldsymbol{\lambda} (\boldsymbol{A} \boldsymbol{a} - \boldsymbol{c}) \tag{B.11}$$

and minimising it. Here, λ denotes the so called "Lagrange multiplier".

This can be done analogously to section B.1 by fulfilling

$$\nabla \mathcal{L}(\boldsymbol{a}, \boldsymbol{\lambda}) = 0 \tag{B.12}$$

which is equivalent to solving the following system of equations that can be derived from Equation B.12 and Equation B.9:

$$\boldsymbol{C} \Delta \boldsymbol{a} + \boldsymbol{A}^T \boldsymbol{\lambda} = 0 \tag{B.13}$$

$$\boldsymbol{A} \Delta \boldsymbol{a} = \boldsymbol{c} - \boldsymbol{A} \boldsymbol{a}_{0j} \tag{B.14}$$

Appendix C

Matrix Reduction

For a matrix equation $\boldsymbol{C}\boldsymbol{a} = \boldsymbol{b}$ with a symmetric matrix $\boldsymbol{C}$, the process of finding its solution can be simplified with respect to naively inverting $\boldsymbol{C}$. Especially in the context of MILLEPEDE-II, where $\boldsymbol{C}$ is huge, this makes a lot of sense. At first, the equation has to be written in block form, by dividing $\boldsymbol{C}$ into four sub-matrices with the symmetric matrices $\boldsymbol{C}_{11}$ and $\boldsymbol{C}_{22}$:

$$\left(\begin{array}{c|c} \boldsymbol{C}_{11} & \boldsymbol{C}_{12} \\ \hline \boldsymbol{C}_{21} & \boldsymbol{C}_{22} \end{array}\right) \cdot \begin{pmatrix} \boldsymbol{a}_1 \\ \boldsymbol{a}_2 \end{pmatrix} = \begin{pmatrix} \boldsymbol{b}_1 \\ \boldsymbol{b}_2 \end{pmatrix} \tag{C.1}$$

According to the Helmert-Wolf blocking method, the inverse of $\boldsymbol{C}$ can be calculated as

$$\left(\begin{array}{c|c} \boldsymbol{C}_{11} & \boldsymbol{C}_{12} \\ \hline \boldsymbol{C}_{21} & \boldsymbol{C}_{22} \end{array}\right)^{-1} = \left(\begin{array}{c|c} \boldsymbol{S}^{-1} & -\boldsymbol{S}^{-1}\boldsymbol{C}_{12}\boldsymbol{C}_{22}^{-1} \\ \hline -\boldsymbol{C}_{22}^{-1}\boldsymbol{C}_{21}\boldsymbol{S}^{-1} & \boldsymbol{C}_{22}^{-1} + \boldsymbol{C}_{22}^{-1}\boldsymbol{C}_{21}\boldsymbol{S}^{-1}\boldsymbol{C}_{12}\boldsymbol{C}_{22}^{-1}\boldsymbol{C}_{12}\boldsymbol{C}_{22}^{-1} \end{array}\right), \tag{C.2}$$

where the matrix $\boldsymbol{S}$ is the so called "Schur complement" and is defined as

$$\boldsymbol{S} = \boldsymbol{C}_{11} - \boldsymbol{C}_{12}\boldsymbol{C}_{22}^{-1}\boldsymbol{C}_{21}. \tag{C.3}$$

Equation C.1 can now be solved by

$$\begin{pmatrix} \boldsymbol{a}_1 \\ \boldsymbol{a}_2 \end{pmatrix} = \left(\begin{array}{c|c} \boldsymbol{S}^{-1} & -\boldsymbol{S}^{-1}\boldsymbol{C}_{12}\boldsymbol{C}_{22}^{-1} \\ \hline -\boldsymbol{C}_{22}^{-1}\boldsymbol{C}_{21}\boldsymbol{S}^{-1} & \boldsymbol{C}_{22}^{-1} + \boldsymbol{C}_{22}^{-1}\boldsymbol{C}_{21}\boldsymbol{S}^{-1}\boldsymbol{C}_{12}\boldsymbol{C}_{22}^{-1}\boldsymbol{C}_{12}\boldsymbol{C}_{22}^{-1} \end{array}\right) \cdot \begin{pmatrix} \boldsymbol{b}_1 \\ \boldsymbol{b}_2 \end{pmatrix}. \tag{C.4}$$

If the sub-vector $\boldsymbol{a}_1$ in Equation C.1 would be 0[1], a so called "local solution" for $\boldsymbol{a}_2$ can be found as

$$\boldsymbol{a}_2^* = -\boldsymbol{C}_{22}^{-1}\boldsymbol{b}_2. \tag{C.5}$$

From Equation C.4, the solution for sub-vector $\boldsymbol{a}_1$ can now be calculated as

$$\boldsymbol{S}\boldsymbol{a}_1 = \boldsymbol{b}_1 - \boldsymbol{C}_{12}\boldsymbol{a}_2^*, \tag{C.6}$$

[1] In the context of a track based alignment, this would correspond to the corrections to the geometry being 0.

where the right-hand-side is already known from calculating the local solution beforehand.

Appendix D

Alignment Jacobians

D.1 Rigid Body Alignment Jacobians

For the calculation of the alignment Jacobians for rigid bodies, the derivatives of the residual defined as $\boldsymbol{r} = \boldsymbol{q} - \boldsymbol{q}_{\mathtt{corr}}$, where

$$\boldsymbol{q}_{\mathtt{corr}} = \Delta\boldsymbol{q} + \Delta\boldsymbol{R}\boldsymbol{q} \tag{D.1}$$

is the corrected local position and $\boldsymbol{q} = (u, v, w)$ the best prior estimate for the hit position, with respect to a set of alignment parameters $\boldsymbol{a} = (\Delta u,\ \Delta v,\ \Delta w,\ \alpha,\ \beta,\ \gamma)$ have to be calculated[1].

The rigid body alignment Jacobian

$$\frac{\partial \boldsymbol{r}}{\partial \boldsymbol{a}} = \frac{\partial \boldsymbol{q}}{\partial \boldsymbol{a}} - \frac{\partial \boldsymbol{q}_{\mathtt{corr}}}{\partial \boldsymbol{a}} \tag{D.2}$$

can therefore be split into two parts and calculated separately.

The positional derivatives of the corrected position are trivial and lead to a 3×3 unit matrix.

However, the calculation of rotational derivatives is more involved. Starting with the rotation correction matrix in Equation 5.18, the derivatives with respect to the angles α, β and γ have to be calculated at vanishing initial alignment parameters (i.e. at $\alpha = \beta = \gamma = 0$). This yields[2]

$$\left.\frac{\partial \Delta R}{\partial \alpha}\right|_{\alpha=\beta=\gamma=0} = \begin{pmatrix} 0 & 0 & 0 \\ 0 & 0 & -1 \\ 0 & 1 & 0 \end{pmatrix} \tag{D.3}$$

$$\left.\frac{\partial \Delta R}{\partial \beta}\right|_{\alpha=\beta=\gamma=0} = \begin{pmatrix} 0 & 0 & 1 \\ 0 & 0 & 0 \\ -1 & 0 & 0 \end{pmatrix} \tag{D.4}$$

$$\left.\frac{\partial \Delta R}{\partial \gamma}\right|_{\alpha=\beta=\gamma=0} = \begin{pmatrix} 0 & -1 & 0 \\ 1 & 0 & 0 \\ 0 & 0 & 0 \end{pmatrix} \tag{D.5}$$

[1] Other parameters defined as in subsection 5.5.1.

[2] These are independent of the order of multiplication chosen in Equation 5.18

Derivatives of measured hits with respect to the rigid body alignment parameters therefore are

$$\frac{\partial \boldsymbol{q}_{\mathtt{cor}}}{\partial \boldsymbol{a}} = \left(\mathbb{1}_{3\times 3} \quad \frac{\partial \Delta R}{\partial \alpha}\boldsymbol{q} \quad \frac{\partial \Delta R}{\partial \beta}\boldsymbol{q} \quad \frac{\partial \Delta R}{\partial \gamma}\boldsymbol{q}\right) \tag{D.6}$$

$$= \begin{pmatrix} 1 & 0 & 0 & 0 & w & -v \\ 0 & 1 & 0 & -w & 0 & u \\ 0 & 0 & 1 & v & -u & 0 \end{pmatrix}. \tag{D.7}$$

The derivatives of the estimated hit position with respect to the alignment parameters can be calculated via[3]

$$\frac{\partial \boldsymbol{q}}{\partial \boldsymbol{q}_{\mathtt{cor}}}\frac{\partial \boldsymbol{q}_{\mathtt{cor}}}{\partial \boldsymbol{a}} = \begin{pmatrix} 0 & 0 & u' \\ 0 & 0 & v' \\ 0 & 0 & 1 \end{pmatrix} \begin{pmatrix} 1 & 0 & 0 & 0 & w & -v \\ 0 & 1 & 0 & -w & 0 & u \\ 0 & 0 & 1 & v & -u & 0 \end{pmatrix} \tag{D.8}$$

$$= \begin{pmatrix} 0 & 0 & u' & u'v & -u'u & 0 \\ 0 & 0 & v' & v'v & -v'u & 0 \\ 0 & 0 & 1 & v & -u & 0 \end{pmatrix} \tag{D.9}$$

with local slopes $u' = t_u/t_w$ and $v' = t_v/t_w$, while $\boldsymbol{t} = (t_u,\ t_v,\ t_w)^T$ being the local tangent of the incoming track.

The final Jacobian that consists of the derivatives of the residuals with respect to the alignment parameters can now be written as

$$\frac{\partial \boldsymbol{r}}{\partial \boldsymbol{a}} = \frac{\partial \boldsymbol{q}}{\partial \boldsymbol{a}} - \frac{\partial \boldsymbol{q}_{\mathtt{cor}}}{\partial \boldsymbol{a}} = \begin{pmatrix} -1 & 0 & u' & u'v & -u'u & v \\ 0 & -1 & v' & v'v & -v'u & -u \\ 0 & 0 & 0 & 0 & 0 & 0 \end{pmatrix}. \tag{D.10}$$

D.2 Alignment Jacobian for Surface Deformations

Since surface deformations are parameterised only to affect to w-coordinate, it is not possible to directly measure them. However, they can be expressed as a function of the inclination angle and can be measured as projections of the deformations onto the nominal sensor plane parametrised by the local coordinates (u, v):

$$\Delta \boldsymbol{q}_m = h(x, y)\ \boldsymbol{q}', \tag{D.11}$$

with the height function $h(x, y)$[4] as defined in Equation 5.21 and the vector $\boldsymbol{q}' = (u', v')$ consisting of the local track slopes (see Equation 5.32).

[3] Here, the fact that $w = 0$ always holds, since only the u- and v-coordinate are measured, is used.

[4] x and y again are the normalised local coordinates.

Now, the derivatives have to be calculated with respect to $\boldsymbol{c}$ defined as in Equation 5.29 which results in

$$\frac{\partial \boldsymbol{m}}{\partial \boldsymbol{\Delta p}_{\texttt{surface}}} = \begin{pmatrix} u'P_2(x)P_0(y) & v'P_2(x)P_0(y) \\ u'P_1(x)P_1(y) & v'P_1(x)P_1(y) \\ u'P_0(x)P_2(y) & v'P_0(x)P_2(y) \\ u'P_3(x)P_0(y) & v'P_3(x)P_0(y) \\ u'P_2(x)P_1(y) & v'P_2(x)P_1(y) \\ u'P_1(x)P_2(y) & v'P_1(x)P_2(y) \\ u'P_0(x)P_3(y) & v'P_0(x)P_3(y) \end{pmatrix}^T . \tag{D.12}$$

Appendix E

Hierarchy Jacobians

Here, the matrix that transforms rigid body alignment parameters of a composite detector entity to the parameters of its subcomponents, i.e.

$$\Delta \boldsymbol{p}_{\mathrm{s}} = \boldsymbol{C}\, \Delta \boldsymbol{p}_{\mathrm{c}}, \tag{E.1}$$

is derived.

The transformation matrix can be expressed as the block matrix

$$\boldsymbol{C} = \begin{pmatrix} \boldsymbol{C}_{11} & \boldsymbol{C}_{12} \\ \boldsymbol{C}_{21} & \boldsymbol{C}_{22} \end{pmatrix}, \tag{E.2}$$

where each block corresponds to a specific transformation.

$\boldsymbol{C}_{11}$ is the transformation of translations of the composite part to the subcomponent parts. It depends on the rotation matrices, i.e. rotations from local to global coordinate systems, of the subcomponent, $\boldsymbol{R}_{\mathrm{s}}$, and the one of the composite structure, $\boldsymbol{R}_{\mathrm{c}}$.

$$\boldsymbol{C}_{11} = \boldsymbol{R}_{\mathrm{s}}^{-1} \boldsymbol{R}_{\mathrm{c}} \tag{E.3}$$

$\boldsymbol{C}_{12}$ corresponds to the transformation from composite rotations to subcomponent translations and can be partitioned in three columns, i.e.

$$\boldsymbol{C}_{12} = \left(\boldsymbol{C}_{12}^{\alpha}\, \boldsymbol{C}_{12}^{\beta}\, \boldsymbol{C}_{12}^{\gamma} \right), \tag{E.4}$$

with the columns defined as

$$\boldsymbol{C}_{12}^{i} = \boldsymbol{R}_{\mathrm{s}}^{-1} \left(\boldsymbol{R}_{\mathrm{c}}\, \frac{\partial \boldsymbol{\Delta R}}{\partial i}\, \boldsymbol{R}_{\mathrm{c}}^{-1} \Delta \boldsymbol{x}_0 \right), \tag{E.5}$$

with $i = \alpha, \beta, \gamma$.

$\boldsymbol{C}_{22}$ can again be divided into three columns:

$$\boldsymbol{C}_{22} = \left(\boldsymbol{C}_{22}^{\alpha}\, \boldsymbol{C}_{22}^{\beta}\, \boldsymbol{C}_{22}^{\gamma} \right). \tag{E.6}$$

Here, the column vectors can be calculated as a linear approximation of the Euler angles corresponding to the rotation matrices

$$\boldsymbol{R}_{22}^{i} = \boldsymbol{R}_{\mathtt{s}}^{-1} \left(\boldsymbol{R}_{\mathtt{c}} \, \frac{\partial \boldsymbol{\Delta R}}{\partial i} \, \boldsymbol{R}_{\mathtt{c}}^{-1} \right) \boldsymbol{R}_{\mathtt{s}}, \tag{E.7}$$

with $i = \alpha, \beta, \gamma$.

$\boldsymbol{C}_{21}$ corresponds to the transformation of translations of the composite part to rotations of the subcomponent parts - which is zero:

$$\boldsymbol{C}_{21} = 0. \tag{E.8}$$

These calculations are based on [56].

Appendix F

Additional Alignment Results

F.1 Additional Results of the Telescope Alignments

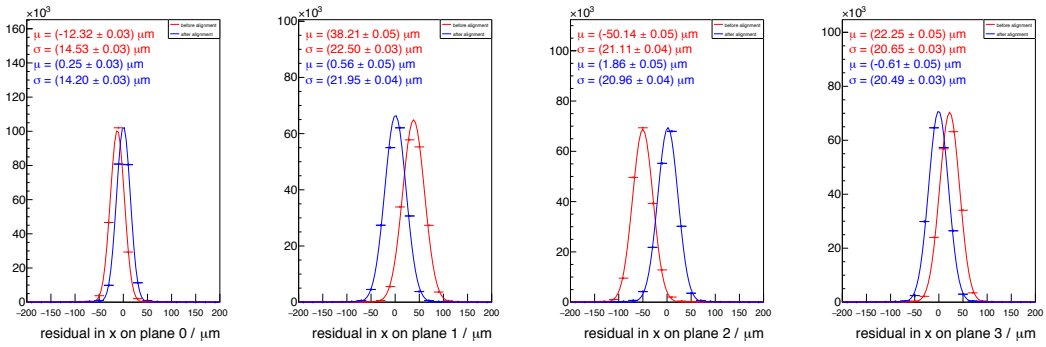

(A) First plane (B) Second plane (C) Third plane (D) Fourth plane

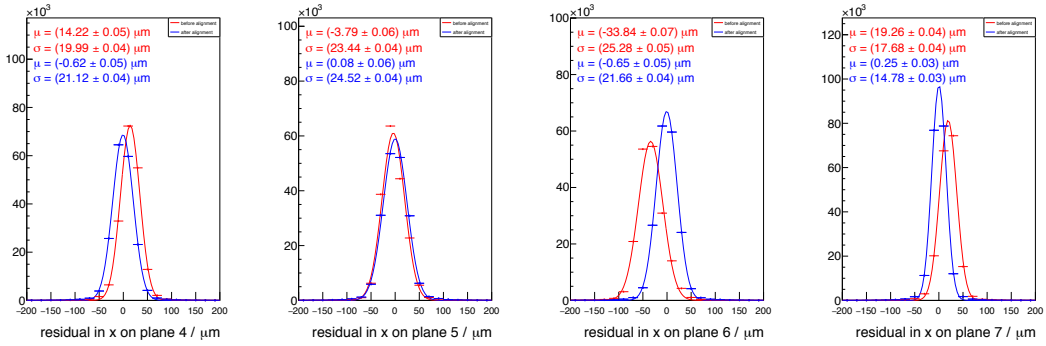

(E) Fifth plane (F) Sixth plane (G) Seventh plane (H) Last plane

FIGURE F.1: Eight-plane MUPIX telescope x: Track residuals for the un-aligned (red) and aligned (blue) telescope in local x-direction of an eight-plane MUPIX8 telescope. The stated μ and σ are the means and standard deviations of the depicted Gaussian fits.

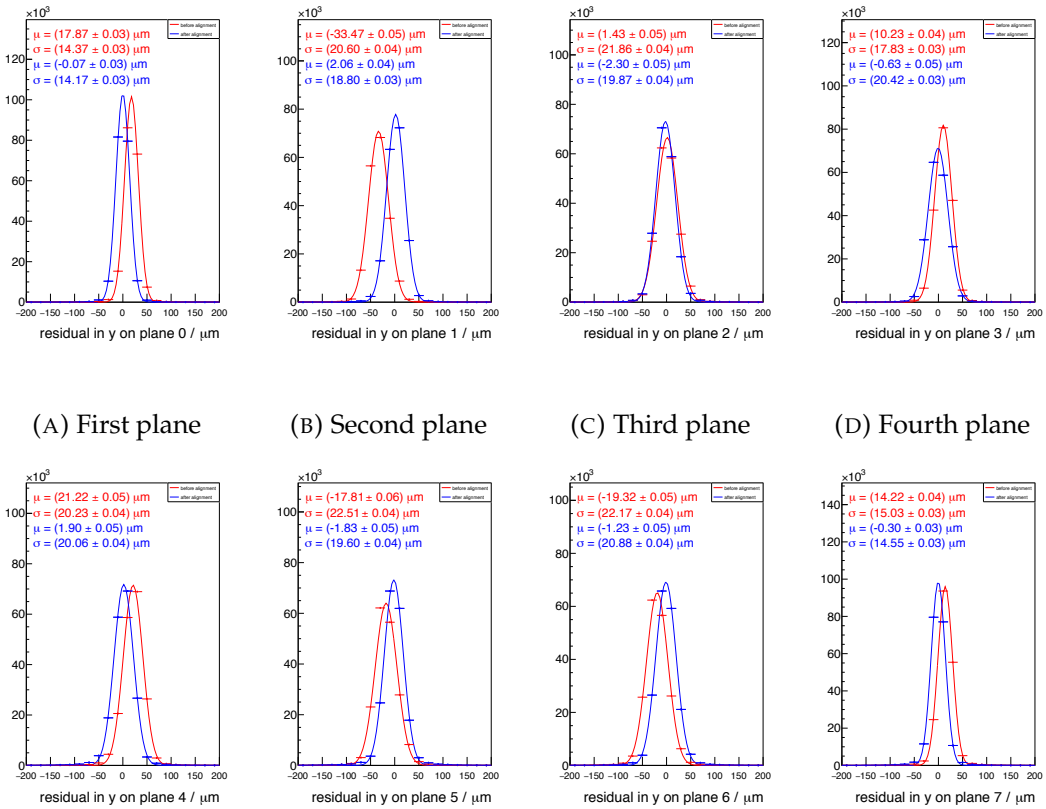

(A) First plane (B) Second plane (C) Third plane (D) Fourth plane

(E) Fifth plane (F) Sixth plane (G) Seventh plane (H) Last plane

FIGURE F.2: Eight-plane MUPIX telescope y: Track residuals for the un-aligned (red) and aligned (blue) telescope in local y-direction of an eight-plane MUPIX8 telescope. The stated μ and σ are the means and standard deviations of the depicted Gaussian fits.

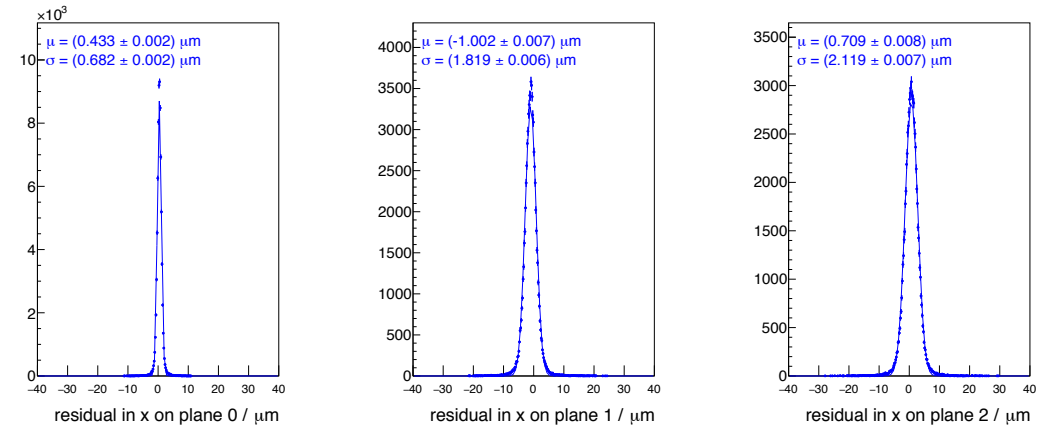

(A) First plane (B) Second plane (C) Third plane

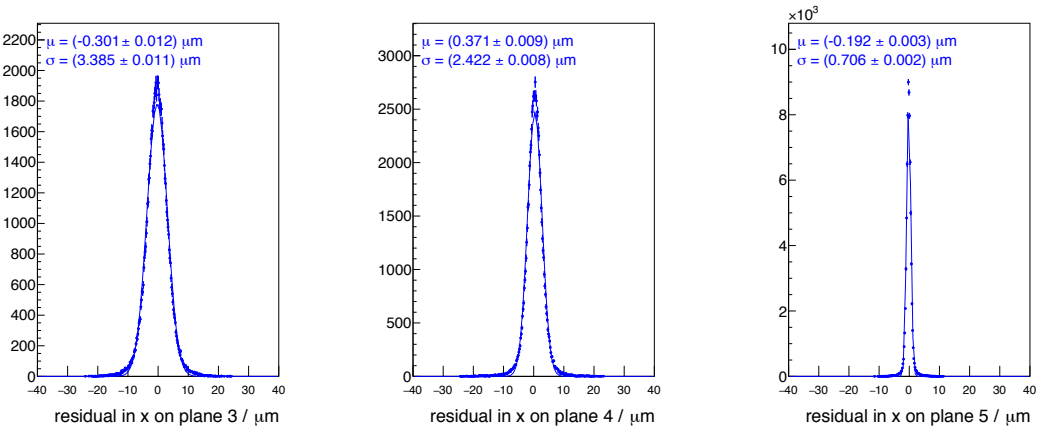

(D) Fourth plane (E) Fifth plane (F) Sixth plane

FIGURE F.3: Six-plane EUDET type telescope: Track residuals for an aligned EUDET type telescope in local x-direction. The stated μ and σ are the means and standard deviations of the depicted Gaussian fits.

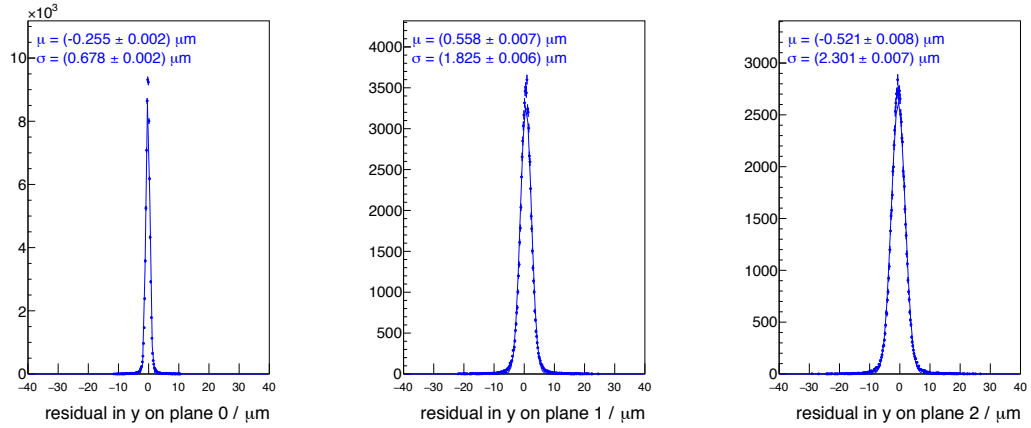

(A) First plane (B) Second plane (C) Third plane

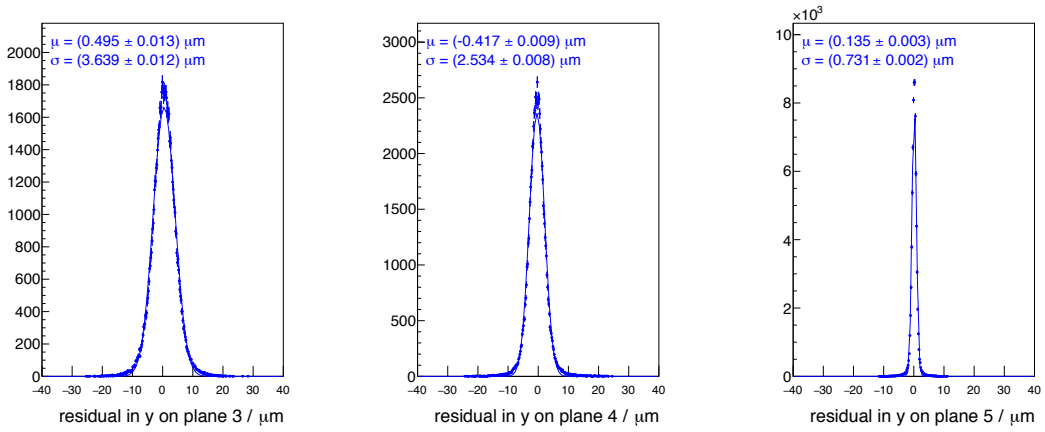

(D) Fourth plane (E) Fifth plane (F) Sixth plane

FIGURE F.4: Six-plane EUDET type telescope: Track residuals for an aligned EUDET type telescope in local y-direction. The stated μ and σ are the means and standard deviations of the depicted Gaussian fits.

F.2 Additional Results of the Tracker Alignment

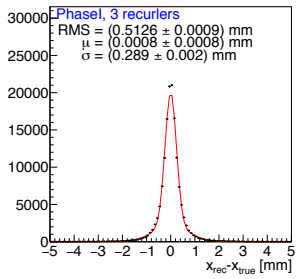

(A) Nominal in x.

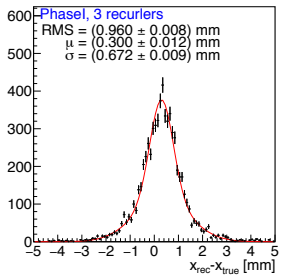

(B) Misaligned in x.

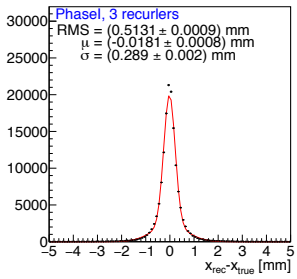

(C) Aligned in x.

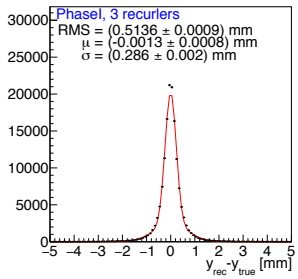

(D) Nominal in y.

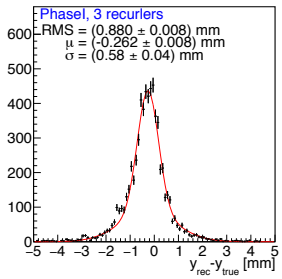

(E) Misaligned in y.

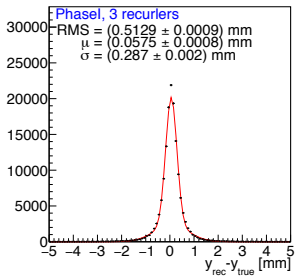

(F) Aligned in y.

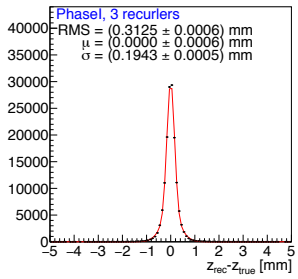

(G) Nominal in z.

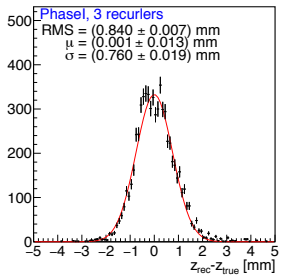

(H) Misaligned in z.

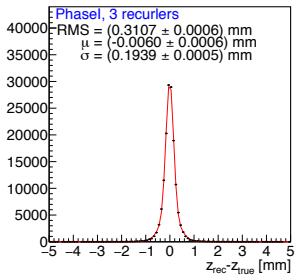

(I) Aligned in z.

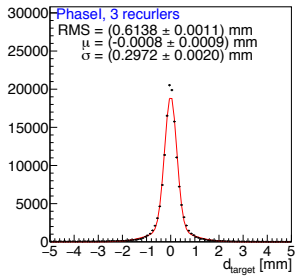

(J) Distance to target surface, nominal.

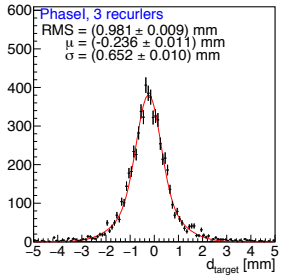

(K) Distance to target surface, misaligned.

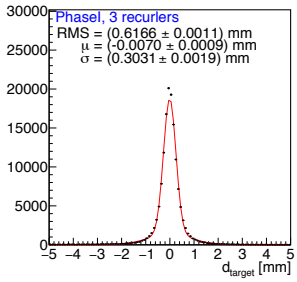

(L) Distance to target surface, aligned.

FIGURE F.5: Reconstructed vertex position for the true, the misaligned and the aligned detector geometry. Negative distances denote a vertex position inside the target volume. The fits are the sum of two Gaussians and the quoted σ corresponds to the area-weighted mean.

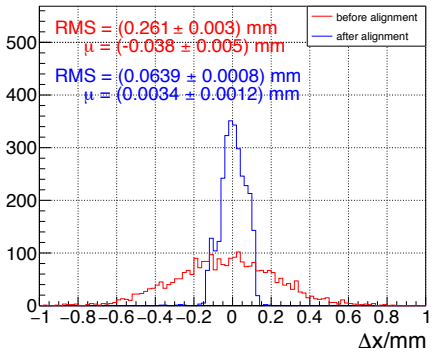

(A) Offset in x.

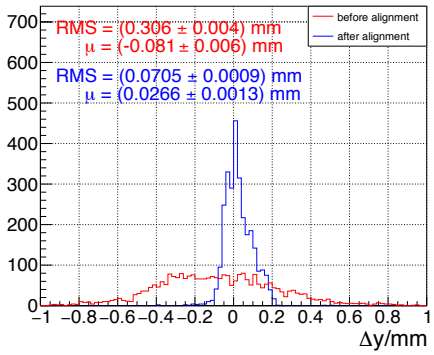

(B) Offset in y.

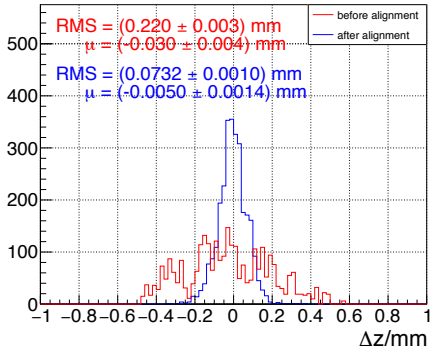

(C) Offset in z.

FIGURE F.6: Offsets from the true position left over after the performance of a full detector alignment.

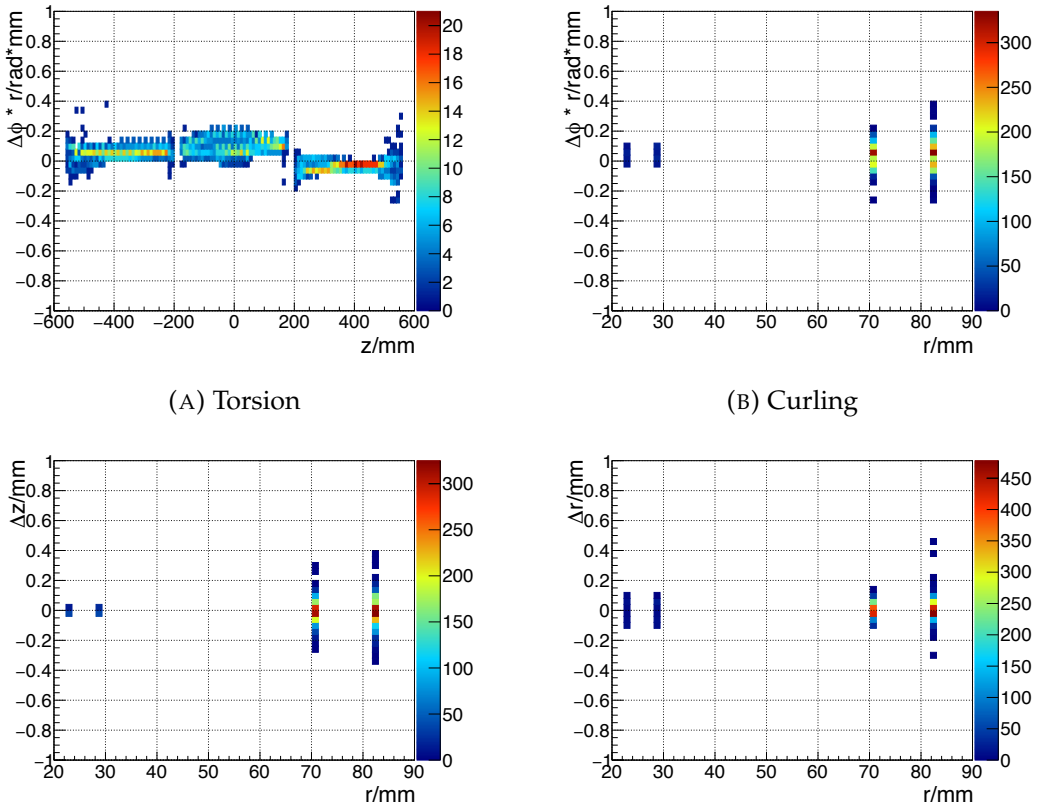

(A) Torsion

(B) Curling

(C) Shearing

(D) Radial

FIGURE F.7: No visible correlations means none of the weak modes presented in section 5.8 could be observed after alignment.

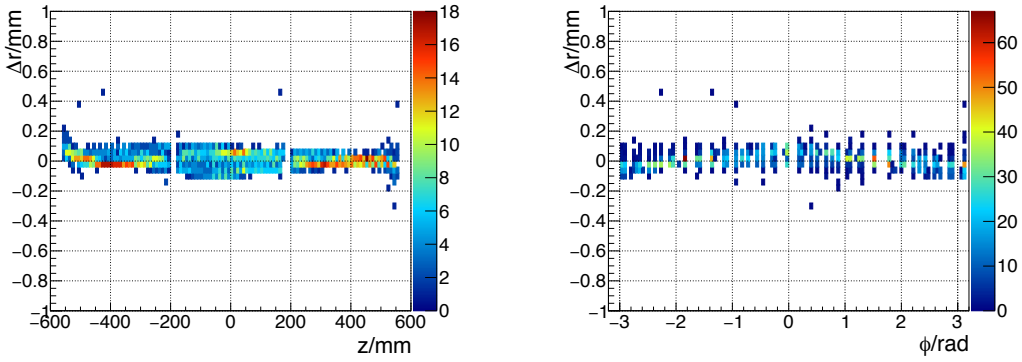

(A) Bowing

(B) Elliptical

(C) Stretching

(D) Sagitta

FIGURE F.8: No visible correlations means none of the weak modes presented in section 5.8 could be observed after alignment.

Bibliography

[1] A. Einstein. *Statement to William Miller*. LIFE magazine, May 1955.

[2] G. Aad et al. "Observation of a new particle in the search for the Standard Model Higgs boson with the ATLAS detector at the LHC". In: (2012). arXiv: 1207.7214 [hep-ex].

[3] C. Burgard and D. Galbraith. *Standard Model of Physics*. 2012.

[4] M. Thomson. *Modern particle physics*. New York: Cambridge University Press, 2013. ISBN: 9781107034266.

[5] C. Patrignani et al. "Review of Particle Physics". In: *Chin. Phys.* C40.10 (2016), p. 100001.

[6] Y. Fukuda et al. "Evidence for oscillation of atmospheric neutrinos". In: *Phys. Rev. Lett.* 81 (1998), pp. 1562–1567. eprint: hep-ex/9807003.

[7] Q. R. Ahmad et al. "Measurement of the charged current interactions produced by B-8 solar neutrinos at the Sudbury Neutrino Observatory". In: *Phys. Rev. Lett.* 87 (2001), p. 071301. eprint: nucl-ex/0106015.

[8] K. Eguchi et al. "First results from KamLAND: Evidence for reactor anti- neutrino disappearance". In: *Phys. Rev. Lett.* 90 (2003), p. 021802. eprint: hep-ex/0212021.

[9] G. Hernández-Tomé, G. López Castro, and P. Roig. "Flavor violating leptonic decays of τ and μ leptons in the Standard Model with massive neutrinos". In: *ArXiv e-prints* (July 2018). arXiv: 1807.06050 [hep-ph].

[10] M. Kakizaki, Y Ogura, and F. Shima. "Lepton flavor violation in the triplet Higgs model". In: *Physics Letters B* 566.3 (2003), pp. 210–216. ISSN: 0370-2693.

[11] J. Bernabéu, E. Nardi, and D. Tommasini. "μ-e conversion in nuclei and Z' physics". In: *Nuclear Physics B* 409 (Nov. 1993), pp. 69–86. eprint: hep-ph/9306251.

[12] W. J. Marciano, T. Mori, and J. M. Roney. "Charged Lepton Flavor Violation Experiments". In: *Ann.Rev.Nucl.Part.Sci.* 58 (2008), pp. 315–341.

[13] U. Bellgardt et al. "Search for the Decay $\mu^+ \to e^+e^+e^-$". In: *Nucl.Phys.* B299 (1988), p. 1.

[14] W. Bertl et al. "Search for the decay $\mu^+ \to e^+e^+e^-$". In: *Nucl. Phys.* B 260.1 (1985), pp. 1–31. ISSN: 0550-3213.

[15] A. Blondel et al. “The Phase I Mu3e Experiment”. To be published, technical design report for the Mu3e experiment.

[16] V. L. Highland. “Some Practical Remarks on Multiple Scattering”. In: Nucl.Instrum.Meth. 129 (1975), p. 497.

[17] L. Huth. “A High Rate Testbeam Data Acquisition System and Characterization of High Voltage Monolithic Active Pixel Sensors”. PhD thesis. Universität Heidelberg, 2018.

[18] I. Perić. “A novel monolithic pixelated particle detector implemented in high-voltage CMOS technology”. In: Nucl.Instrum.Meth. A582 (2007), p. 876.

[19] Y. Munwes. “Tile Detector - Preliminary Testbeam Results”. Talk given at an internal Mu3e meeting. Apr. 2018.

[20] S. Corrodi. “A Timing Detector based on Scintillating Fibres for the Mu3e Experiment”. PhD thesis. ETH Zürich, 2018.

[21] D. vom Bruch. “Pixel Sensor Evaluation and Online Event Selection for the Mu3e Experiment”. PhD thesis. Universität Heidelberg, Oct. 2017.

[22] F. Meier and Mu3e collaboration. Mu3e Inner Detector Design and Pixel. Tech. rep. Talk given at a PSI BVR. Internal Note, 2018.

[23] M. Seidel et al. “Production of a 1.3MW proton beam at PSI”. In: IPAC’10. Kyoto, Japan, 2010.

[24] A. Knecht. “The High Intensity Muon Beam Line (HiMB) project at PSI”. In: The 19th International Workshop on Neutrinos from Accelerators (NUFACT2017). Uppsala, 2017.

[25] GEANT – Detector Description and Simulation Tool. CERN Program Library Long Writeup W5013. 1993.

[26] S. Agostinelli et al. “Geant4–a simulation toolkit”. In: Nucl. Instr. Meth. A 506.3 (2003), pp. 250–303. ISSN: 0168-9002.

[27] P. Biallass and T. Hebbeker. “Parametrization of the Cosmic Muon Flux for the Generator CMSCGEN”. In: (2009). arXiv: 0907.5514 [astro-ph.IM].

[28] N. Berger et al. “A New Three-Dimensional Track Fit with Multiple Scattering”. In: Nucl. Instr. Meth A. 844 C (2017), pp. 135–140. arXiv: 1606.04990 [physics.ins-det].

[29] S. Schenk. “A fast vertex f t for the Mu3e experiment”. Bachelor Thesis. Heidelberg University, 2013.

[30] M. Kiehn. “Pixel Sensor Evaluation and Track Fitting for the Mu3e Experiment”. PhD thesis. Universität Heidelberg, Feb. 2016.

[31] D. Becker et al. “The P2 Experiment - A future high-precision measurement of the electroweak mixing angle at low momentum transfer”. In: ArXiv e-prints (Feb. 2018). arXiv: 1802.04759 [nucl-ex].

[32] H. Spieler. Semiconductor Detector Systems. Oxford Scholarship, Sept. 2007.

[33] Wikipedia. p-n junction. Oct. 2018. URL: https://en.wikipedia.org/wiki/P%E2%80%93n_junction.

[34] I. Perić et al. "High-voltage pixel detectors in commercial CMOS technologies for ATLAS, CLIC and Mu3e experiments". In: Nucl.Instrum.Meth. A731 (2013), pp. 131–136.

[35] T. Weber. "HV-MAPS for the Panda Luminosity Detector". In: International Conference on Science and Techonology for FAIR (Oct. 2014).

[36] Ken Boyette. OpenCores 8bit/10bit encoder and decoder. URL: http://opencores.org/project,8b10b%5C_encdec.

[37] J. Kroeger. "Readout Hardware for the MuPix8 Pixel Sensor Prototype and a Firmware-based MuPix8 Emulator". Masters thesis. Universität Heidelberg, 2017.

[38] R. Brun et al. ROOT Users Guide 3.1c. Geneva, Sept. 2001.

[39] I. Paraskevas. "PhD Thesis in preparation". PhD thesis. University College London.

[40] C. Kleinwort. "General Broken Lines as advanced track f tting method". In: Nucl.Instrum.Meth. A673 (2012), pp. 107–110. arXiv: 1201.4320.

[41] C. Kleinwort. General Broken Lines as advanced track f tting method. 2013.

[42] A. Strandlie and W. Wittek. "Derivation of Jacobians for the propagation of covariance matrices of track parameters in homogeneous magnetic f elds". In: Nuclear Instruments and Methods in Physics Research A 566 (Oct. 2006), pp. 687–698.

[43] V. Blobel and E. Lohrmann. Statistische Methoden und numerische Methoden der Datenanalyse. 2012.

[44] J. Draeger. "Track based alignment of the CMS silicon tracker and its implication on physics performance". PhD thesis. Hamburg U., 2011.

[45] V. Blobel. Millepede-II Linear Least Squares Fits with a Large Number of Parameters. 2007. URL: http://www.desy.de/~blobel/Mptwo.pdf.

[46] C. Kleinwort. "H1 alignment experience". In: Proceedings, f rst LHC Detector Alignment Workshop, CERN, Geneva, Switzerland, 4-6 September 2006. 2006, pp. 41–50.

[47] V. Blobel. "Software alignment for tracking detectors". In: Nucl. Instrum. Meth. A566 (2006), pp. 5–13.

[48] C. Kleinwort and F. Meier. "Alignment of the CMS silicon tracker - and how to improve detectors in the future". In: Nuclear Instruments and Methods in Physics Research A 650 (Sept. 2011), pp. 240–244. arXiv: 1010.2039 [physics.ins-det].

[49] V. Blobel, C. Kleinwort, and F. Meier. "Fast alignment of a complex tracking detector using advanced track models". In: *Comput.Phys.Commun.* 182 (2011), pp. 1760–1763. arXiv: 1103.3909 [physics.ins-det].

[50] T. Lampén. "Alignment of the CMS silicon tracker". In: *J. Phys. Conf. Ser.* 523 (2014), p. 012024.

[51] S. Chatrchyan et al. "Alignment of the CMS tracker with LHC and cosmic ray data". In: *JINST* 9 (2014), P06009. arXiv: 1403.2286 [physics.ins-det].

[52] N. Bartosik. "Simultaneous alignment and Lorentz angle calibration in the CMS silicon tracker using Millepede II". In: *PoS* EPS-HEP2013 (2013), p. 074.

[53] G. Flucke. "Alignment of the CMS silicon tracker". In: *J. Phys. Conf. Ser.* 368 (2012), p. 012036.

[54] J. Behr. "Alignment procedures for the CMS silicon tracker". In: *J. Phys. Conf. Ser.* 396 (2012), p. 022005.

[55] M. Weber. "Calibration, alignment and tracking performance of the CMS silicon strip tracker". In: *Nucl. Instrum. Meth.* A628 (2011), pp. 59–63.

[56] M. Stoye. "Calibration and Alignment of the CMS Silicon Tracking Detector". PhD thesis. Universität Hamburg, 2007.

[57] T. Bilka and J. Kandra. "Millepede alignment of the Belle 2 sub-detectors after first collisions". In: *arXiv e-prints*, arXiv:1812.05340 (Dec. 2018), arXiv:1812.05340. arXiv: 1812.05340 [physics.ins-det].

[58] H. Jansen et al. "Performance of the EUDET-type beam telescopes". In: *EPJ Techn Instrum* 3.1 (2016), p. 7.